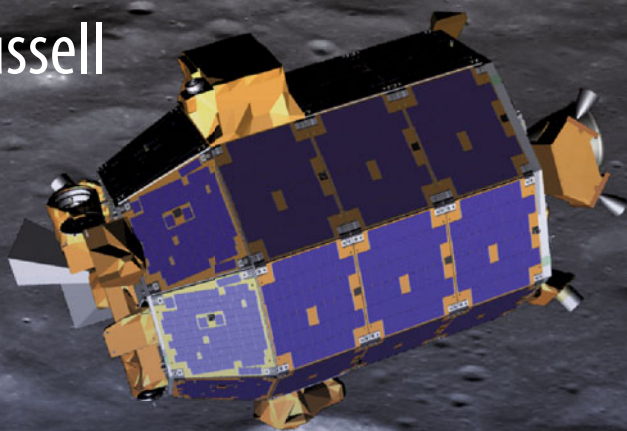Richard C. Elphic
Christopher T. Russell

Editors

The Lunar Atmosphere and Dust Environment Explorer Mission (LADEE)

Springer

The Lunar Atmosphere and Dust Environment
Explorer Mission (LADEE)

Richard C. Elphic · Christopher T. Russell
Editors

The Lunar Atmosphere and Dust Environment Explorer Mission (LADEE)

Springer

Editors
Richard C. Elphic
NASA Ames Research Center
Moffett Field, California, USA

Christopher T. Russell
Department of Earth and Space Sciences
University of California Los Angeles
Los Angeles, California, USA

Cover Image: The Lunar Atmosphere and Dust Environment Explorer (LADEE) spacecraft is pictured orbiting the Moon in its operational configuration. The large, bright crater in the background is Sundman V, where LADEE impacted at the end of its mission. The LADEE rendering was provided by LADEE mechanical engineer Owen Nishioka of NASA Ames Research Center. The lunar surface was rendered using the digital elevation model and photomosaic derived from Lunar Reconnaissance Orbiter/Lunar Reconnaissance Orbiter Camera (LROC) wide-angle camera data, publicly available at http://wms.lroc.asu.edu/lroc/view_rdr/WAC_GLD100, courtesy of Arizona State University and the LRO Project at NASA Goddard Space Flight Center.

Contents

Foreword

The Lunar Atmosphere and Dust Environment Explorer Mission

C.T. Russell · R.C. Elphic

The Moon is our most familiar solar system object after our terrestrial home. We see it almost every night, and if we are observant, almost every day. But half of the Moon is unfamiliar; it is on the side away from the Earth and invisible except from vantage points in space. And do we really know the front side of the Moon? We see it all the time but do we know it as well as we should and do we really understand it? There is much that is important that we do not know. Are there hidden things such as the recently discovered water in the shadowed polar regions that we have not studied? Are there secrets hiding in plain sight? Surprisingly, previous missions, while discovering much about the Moon's surface and interior had left the lunar atmosphere virtually untouched. The Earth has an exosphere at very high altitudes where the atoms and molecules travel in parabolic arcs without colliding until they return to lower altitudes. The Moon too has an exosphere but here the entire atmosphere is exosphere. The arcs along which the particles travel extend from the surface to space and back to the surface. How can we study this exosphere? How can we afford to study it?

Lunar exploration need not be expensive. The Moon can be reached by the smaller rockets in our fleet and need not be manned by astronauts but by astrobots. Our robotic spacecraft are up to the task. The engineers and scientists at the NASA Ames Research Center in Mountain View California stepped up to the challenge. Ames had led the highly productive low cost Pioneer Venus mission of the late 1970's and 80's, and had embarked on the development of low-cost robotic spacecraft for the Constellation program. It could repeat the challenge for the Moon and hence the Lunar Atmosphere and Dust Environment Explorer Mission or LADEE was born.

This volume contains five articles describing the mission and its instruments. The first paper, by the project scientist Richard C. Elphic and his colleagues describes the mission,

C.T. Russell (✉)
University of California, Los Angeles, CA 90095, USA
e-mail: ctrussel@igpp.ucla.edu

R.C. Elphic
NASA Ames Research Center, Moffett Field, CA, USA

objectives, the launch vehicle, spacecraft and the mission itself. This is followed by a description of LADEE's Neutral Mass Spectrometer by Paul Mahaffy and company. This paper describes the investigation that directly targets the lunar exosphere. The exosphere can also be explored optically in the ultraviolet. In the following article Anthony Colaprete describes LADEE's Ultraviolet and Visible Spectrometer that operated from 230 mm to 810 mm scanning the atmosphere just above the surface. Not only is there atmosphere but there is also dust that putatively can be levitated above the surface, possibly by electric fields on the Moon's surface. Mihaly Horanyi leads this investigation called the Lunar Dust Experiment aimed at understanding the purported observations of levitated dust. This experiment was also very successful but in this case their discovery was not the electrostatic levitation of dust but that the dust was raised by meteoroid impacts. This is not what had been expected but clearly is the explanation that best fits the data.

The LADEE mission also carried a technology demonstration, the Lunar Laser Communication Demonstration. Don Boroson describes NASA's first step toward very high data rate communication in deep space, in the last of the five articles.

The success of this volume is due to many people; but first of all, the editor wishes to thank the authors who had the difficult job of distilling and compiling the facts such missions produce, into highly readable articles. The editor also benefited from an excellent group of referees who acted as a test readership, refining the manuscripts provided by the authors. These referees included S. Bougher, R. Elphic, R. Gladstone, G. Gronoff, J. Halekas, P. Kellogg, H. Svedham, X. Sun, R. Vondrak, and J.H. Waite.

Equally important has been the strong support this project has received at Springer and the extra effort expended by Nirmala Kumar, Esther Rentmeester and Jennifer Satten. At UCLA we were skillfully assisted by Marjorie Sowmendran who acted as the interface between the authors, the referees and the publishers.

The Lunar Atmosphere and Dust Environment Explorer Mission

**R.C. Elphic · G.T. Delory · Butler P. Hine ·
P.R. Mahaffy · M. Horanyi · A. Colaprete · M. Benna ·
S.K. Noble · The LADEE Science Team**

Abstract The Lunar Atmosphere and Dust Environment Explorer (LADEE) mission was designed to address long-standing scientific questions about the Moon's environment, including the assessment of the composition of the lunar atmosphere, and characterization of the lunar dust environment at low orbital altitudes. LADEE was derived from the Modular Common Spacecraft Bus design that was developed at NASA Ames Research Center; it used modularized subassemblies and existing commercial spaceflight hardware to reduce cost. LADEE was launched on the very first Minotaur V, and was also the first deep space mission launched from Wallops Flight Facility in Virginia. LADEE was equipped with two in situ instruments and a remote sensing instrument to address the atmosphere and dust measurement requirements. LADEE also carried the first deep-space optical communications demonstration, the Lunar Laser Communications Demonstration. LADEE was launched in early September, 2013, took science data for over 140 days in low lunar orbit, and impacted the surface on April 18, 2014.

1 Introduction

It is sometimes incorrectly stated that the Moon has no atmosphere. As Stern ([1999](#)) points out, the Moon does possess a rarified and exotic atmosphere, a fact not realized until the

R.C. Elphic (✉) · G.T. Delory · B.P. Hine · A. Colaprete
NASA Ames Research Center, Moffett Field, CA 94035, USA
e-mail: richard.c.elphic@nasa.gov

P.R. Mahaffy · M. Benna
NASA Goddard Space Flight Center, Greenbelt, MD 20771, USA

M. Horanyi
Laboratory for Atmospheric and Space Physics, University of Colorado, Boulder, CO 80303, USA

S.K. Noble
NASA Headquarters, Washington, DC 20546, USA

Apollo program in the 1960s and 1970s. Today we understand that the Moon is one nearby member of a class of tenuous planetary atmospheres called "surface boundary exospheres", in which atoms and molecules only collide with the surface and not with each other (Killen and Ip 1999; Stern 1999). However, apart from a handful of species that have been identified, we know little about this nearby exosphere, its composition, sources and sinks, and dynamics. The lunar surface boundary exosphere may also possess a significant dust component, whose dynamics are dominated by the combination of vacuum, solar radiation, and the local plasma environment found at the Moon.

1.1 Lunar Atmosphere

Prior to Apollo, the search for evidence of a lunar atmosphere placed successively lower and lower limits on the surface pressure of plausible constituents (see Stern 1999, for a short history), culminating in pre-Apollo estimated limits of 3×10^{-9} bar for hydrogen, $\sim 8 \times 10^{-10}$ bar for He, and $\sim 8 \times 10^{-12}$ bar for Ar (Johnson 1971).

Both space and grounded-based measurements during and since the Apollo missions have confirmed the presence of Ar, He, Na, and K in the lunar atmosphere, and established upper limits for many other constituents. Experiments at the Moon during Apollo measured a few atmospheric species. Suprathermal Ion Detector Experiments (SIDE) delivered to the lunar surface measured ions derived from the lunar atmosphere, including those in the mass ranges of 20–28 amu and 40–44 amu. Both neon and argon were suggested as candidates (Benson et al. 1975). On one occasion, the Apollo 14 SIDE instrument observed a 14-hour long interval of water ions, later believed to be due to the sublimation of Lunar Module-derived water out of the soil after sunrise (Freeman and Hills 1991). Also placed on the surface during Apollo were three Cold Cathode Gauge Experiments (CCGEs) and the Lunar Atmosphere Composition Experiment (LACE). During lunar day, the CCGEs and LACE were swamped by contaminants from the Lunar Module and other equipment on the lunar surface; but at night uncontaminated measurements were made of the lunar atmosphere. The CCGEs provided estimates of total atmospheric pressure, and LACE discovered argon-40 and helium (Hodges et al. 1974). Argon-40 evidently derives from the decay of potassium-40 in lunar rocks and soils. Helium, as a product of alpha-emitting radioactive elements, should also be diffusing out of the lunar interior, but the solar wind also supplies helium to the Moon (in the form of doubly-ionized He). ^{40}Ar is a condensible gas on the Moon, and LACE showed that on the nightside most of the argon adsorbs to the cold regolith grains. The LACE data indicated that, at sunrise, the surface warms and the condensed argon atoms are released, forming a local maximum in density just after sunrise. These LACE data also revealed that helium, which does not condense on the lunar nightside, follows a $T^{-5/2}$ density dependence as predicted by Hodges and Johnson (1968). ^{222}Radon, a radioactive noble gas product of uranium decay, was observed during Apollo through its alpha-particle decay (Gorenstein and Bjorkholm 1973), and again later by Lunar Prospector (Lawson et al. 2005). Both pointed to episodic venting at features such as Aristarchus.

Motivated by the spectroscopic discovery of sodium and potassium in the exosphere of Mercury, these same species were sought and found at the Moon (Potter and Morgan 1988; Tyler et al. 1988). Because Na and K can be measured telescopically from Earth, we understand some aspects of their behavior. For example, the sodium exosphere appears to consist of at least two populations, a thermal and a superthermal component (Potter and Morgan 1988; Sprague et al. 1992). This suggests at least two source processes. There is also telescopic evidence that Na abundance decreases with solar zenith angle (Mendillo et al. 1993; Potter and Morgan 1997). The energetic component of the sodium exosphere

evidently forms a long tail, due to light pressure on the atoms (Smith et al. 1999; Wilson et al. 1999). The sodium exosphere has been observed to vary as the Moon transited the magnetotail (Potter et al. 2000), suggesting a solar wind role in its production. Moreover, transits through the magnetotail plasma sheet force additional variability (Wilson et al. 2006; Kagitani et al. 2010). Curiously, sodium observations from Kaguya showed no systematic drop in density while the Moon crossed the magnetotail. Nevertheless, plasma conditions appear to be important in the production of alkali metal exospheres.

Despite decades of searching, other species thought to derive from the lunar surface have not been found—only upper limits (cf. Stern 1999). Since then, other observations have been made: the Lyman Alpha Mapping Project (LAMP) far-ultraviolet spectrometer aboard the Lunar Reconnaissance Orbiter (LRO) confirmed the presence of helium in the exosphere, and observed helium variability apparently linked to the solar wind (Stern et al. 2012; Feldman et al. 2012). Diatomic hydrogen was discovered by LAMP (Stern et al. 2013), and the experiment has set new upper limits for many species (Cook et al. 2013).

1.2 High Altitude Lunar Dust

In the late 1960's, shortly before the Apollo landings took place, the Surveyor lander television cameras observed a narrow horizon glow shortly after sunset. This surprising feature, apparently limited in altitude but laterally extensive, was interpreted to be due to a population of fine dust electrostatically levitated a few meters above the surface (Rennilson and Criswell 1974). Later Apollo visual observations and orbital photography of more vertically extensive (10's to 100 km) excess brightness along the dark lunar limb motivated the idea that a tenuous dust exosphere also exists at the Moon. Astronaut observations of rays and streamers just before orbital sunrise have been interpreted as due to dust with densities as low as 10^{-4} cm^{-3} at 50 km altitude (McCoy 1976). Some level of dust must exist due to ejecta from the more or less steady micrometeoroid flux. But because the densities ofMcCoy (1976) are higher than expected for ejecta, it was suggested that electrostatic forces acting on charged dust grains could lead to the levitation of these particles, possibly to high altitudes (Stubbs et al. 2006). A reanalysis of Apollo 15 orbital imagery excess brightness suggested dust densities of 0.01 cm^{-3} at 10 km altitude, but could not constrain densities at higher altitudes (Glenar et al. 2011). However, recent LAMP observations also placed limits on exospheric dust densities, $<10^{-5}$ cm^{-3} at the surface assuming 0.1 μm grains and a scale height of 10 km (Feldman et al. 2014). So, no resolution to the high-altitude dust mystery has thus far been found.

2 Mission Requirements

The planetary community has recognized that solar system exploration must fill gaps in our knowledge concerning surface boundary exospheres and the physics of putative dust levitation at nearly airless bodies. Several National Research Council decadal surveys and the "Scientific Context for Exploration of the Moon" (SCEM) report identified the investigation of the pristine state of the lunar atmosphere and dust environment as important priorities for future lunar science missions. Some urgency was expressed regarding measuring the lunar dust and exospheric environment because the Constellation program would send humans missions to the Moon within a decade, potentially overwhelming the natural environment. As seen during Apollo, and as first described by Vondrak (1974) (cf. also Sect. 5.1 in Stern 1999), the Moon's exosphere can recover from limited injections of exotic materials from

natural or manmade events because loss processes can promptly adjust. However, with intensive human activity the delivery rate can become sufficiently high, the atmosphere can become dense enough to reduce the loss rates nonlinearly. The bulk of the atmosphere then would be maintained by products that are delivered by spacecraft and/or leaked from habitats.

In March 2008, the Lunar Atmosphere and Dust Environment Explorer (LADEE) Mission was initiated to address this priority. The LADEE mission was designed to achieve two major scientific goals: (1) to determine the composition of the lunar atmosphere and (2) to understand the lunar dust environment.

Through an understanding of the lunar surface boundary exosphere and dust environment, we learn by extension about other objects in the solar system where similar conditions exist, including larger asteroids, the moons of Mars Phobos and Deimos, most moons of the outer planets, and Kuiper Belt Objects. There is particular synergy with Mercury, in seeking to understand the role of the exosphere in the delivery and sequestration of volatiles at the poles.

In spring 2008, NASA formed a Science Definition Team (SDT) to devise goals and measurement objectives for LADEE and to consider candidate payloads. Like the LADEE mission, the SDT was small and focused. Dr. Laurie Leshin (then at GSFC) chaired the SDT and Dr. William Farrell (GSFC) was Vice-Chair. A complete list of SDT members and their affiliations can be found in the SDT report http://lunarscience.arc.nasa.gov/files/LADEE_SDT_Report.pdf.

In analyzing key science questions, the SDT formulated two science objectives for LADEE: (1) Determine the composition of the lunar atmosphere and investigate the processes that control its distribution and variability, including sources, sinks, and surface interactions; (2) Characterize the lunar exospheric dust environment and measure any spatial and temporal variability and impacts on the lunar atmosphere.

The SDT went on to make specific recommendations concerning measurements of the exosphere. (1) LADEE should provide a thorough species inventory traceable back to atmospheric sources. (2) If the species is one of the few definitively known to exist (i.e., Ar, He, Na, K as of 2008), define the species variability to as short a time-scale as possible. (3) For species that have only upper limits (no known detection), either reduce the known upper limit or make the discovery detection of the species. (4) A sampling of species in each of the primary sources (solar wind, regolith, and radiogenic) is desired. (5) Fly a set of instruments that reliably provides the largest possible coverage of species detection. (6) At least one other instrument, complementary to neutral mass spectrometry, is required to obtain composition. (7) An ultraviolet/visible spectrometer that can address remote measurements beyond LADEE orbit and can connect lunar exospheric gas and particulates is recommended. (8) An ion mass spectrometer is also a candidate instrument, capable of detecting trace species; any such instrument on LADEE should have temporal resolution and sensitivity improvement over the Kaguya Ion Mass Analyzer. (9) The set of instruments should fly for no less than one lunation to ensure LADEE passes through the magnetotail.

The SDT also made recommendations concerning exospheric dust: (1) An in-situ dust detector should be able to detect sub-micrometer particles to increase the likelihood of sensing small lofted grains. (2) LADEE should take full advantage of the extreme variations of the driving external environment to increase the likelihood of dust detection, including sensing incoming micro-meteoroids and associated ejecta during predicted meteor showers and detecting lofted dust during plasma sheet crossings and solar storms (when the surface potential can be large and negative). (3) Use both in situ and remote sensing techniques to obtain a complementary and consistent dust detection data set. (4) Dust measurements should be made over at least one lunation.

Regarding LADEE's launch, science orbit design, and to minimize the risk of exhaust contamination of observations, the SDT recommended: (1) the orbit be retrograde (inclination $180° \pm 20°$),[1] and as close to circular, with as low an altitude and as nearly equatorial as possible (but no higher than 50), consistent with delivering a payload mass of at least 20 kg. (2) The recommended orbit altitude target was a box of $+/-5$ km centered at 45 km altitude or lower over the lunar-sunrise terminator. (3) The Project should consider a dedicated launch at a schedule more compatible with the spacecraft and payload development (SMD initially considered co-manifesting LADEE with another mission as a cost-savings measure). (4) The Project should provide a systemic approach to spacecraft environmental cleanliness, including early development of plans to mitigate the effects of outgassing, thruster firings, and EMI.

The SDT recommended creation of a strong science team, both in instrument selection and in an active participating science community, including exospheric and dust modeling expertise, and encouraged their early integration into LADEE science planning. The SDT recommended a lunar observation ground campaign to occur concurrent with the LADEE mission, and inclusion of space weather monitoring data sets for correlation with LADEE atmosphere and dust observations, to greatly enhance the science return.

The final, top-level Science Mission Directorate programmatic and science requirements for the LADEE project were aimed at accomplishing the following mission objectives:

(1) Determine the composition of the lunar atmosphere and investigate the processes that control its distribution and variability, including sources, sinks, and surface interactions
(2) Characterize the lunar exospheric dust environment and measure any spatial and temporal variability and impacts on the lunar atmosphere
(3) Demonstrate the Lunar Laser Com Demonstration (LLCD)
(4) Create a low-cost reusable spacecraft architecture that can meet the needs of certain planetary science missions
(5) Demonstrate the capability of the Minotaur V as a launch vehicle for planetary missions

The mission was designed to accomplish all required science measurements within the first 100 days after completion of commissioning. The science instrument commissioning and LLCD operations were decoupled, with 4 days of LLCD operations alternating with 3 days of science instrument activities. Following commissioning and the LLCD demonstration, the spacecraft was transferred to the appropriate orbit to begin science operations, marking the start of the planned 100 days of science operations. LADEE science operations actually continued for over 140 days, well beyond the required nominal mission.

3 Mission Description

LADEE was launched on September 7th, 2013 03:27 UTC, from the Wallops Island Flight Facility (WFF) on a Minotaur V launch vehicle (LV). The LV inserted LADEE into an Earth-centered phasing orbit followed by a direct lunar transfer. At lunar arrival, LADEE was inserted into a retrograde equatorial orbit at an inclination of 157°, at which point a commissioning/checkout phase was conducted, followed by the science phase. (The mission's orbit inclination requirement was revised. Orbit dynamics studies had revealed a significant fuel savings for orbit designs with slightly greater deviation from 180°. The science

---

[1]A retrograde orbit provides anti-sun facing orientation for the ram-facing neutral mass spectrometer over the sunrise terminator, a key region of the exosphere. There was concern that spacecraft outgassing on the sun-facing side would contaminate measurements.

Table 1 LADEE Baseline Science Requirements

	Science Requirements
1	Measure the relevant spatial and temporal variations of Ar, He, Na, and K. The temporal scales covered shall range from 12 hours to 1 month. The spatial scales covered shall be as follows: Ar, within $\pm 20°$ of the terminator regions of the Moon; He, sufficient coverage to resolve variations from noon to midnight; K, Na, sufficient coverage to resolve variations over the lunar dayside
2	Detect or establish new limits for selected other species for which previous detections have been attempted. These shall include the following from the family of exogenic/volatile species (CH_4, O, OH, H_2O, CO, S), and the following from the family of endogenic (regolith-derived refractory) species (Si, Al, Mg, Ca, Ti, Fe)
3	Perform a survey for the presence of other species beyond those listed above, or positive ambient ions of these species and other atoms or compounds, within a mass range of 2–150 Da and a sensitivity of several particles/cc
4	Detect or set new limits for the spatial and size distribution of atmospheric dust over an altitude range from 3 km up to 50 km, with a height resolution of 3 km, at a minimum detectable density of 10^{-4} grains/cc, for grains from 100 nanometer to at least 1 micrometer in radius. These observations shall be conducted at the temporal and spatial scales for Ar as outlined in the first science requirement above

team saw no adverse impact to this change.) The total mission duration was 223 days; mission phase details are in Sect. 4.2. The mission was decommissioned by impact into the Moon on April 18th, 2014. The LADEE science mission was designed to fulfill the science requirements in Table 1.

To address the missions's science goals, LADEE's science payload suite was comprised of three high-heritage science instruments: a neutral mass spectrometer to analyze exospheric neutral and ionized gas particles, an ultraviolet/visible spectrometer to measure emissions of gas species and scattered light from possible dust, and an in-situ dust sensor to register the size and density of any dust particles in the exosphere. In addition to these science instruments, LADEE also carried a laser communications system technology demonstration.

The neutral mass spectrometer (NMS) instrument development was directed to NASA Goddard Space Flight Center (GSFC), the ultraviolet/visible spectrometer (UVS) to NASA Ames Research Center (ARC). The dust detector was competed, and the Lunar Dust Experiment (LDEX) from the Laboratory for Atmospheric and Space Physics, University of Colorado, was selected. The science instruments are described in accompanying papers in this journal (Mahaffy et al. 2014; Horanyi et al. 2014; Colaprete et al. 2014). A separate articulated laser assembly comprised the LLCD. Data from the science instruments (NMS, UVS, and LDEx) were processed and will be submitted to the PDS for access by the scientific community. The raw and calibrated data from the nominal mission are expected to be available in August, 2014, and data from the extended phase the following September.

The LADEE project, spacecraft development, integration and test, and mission operations were managed by ARC. LADEE's payload instruments and science operations center were managed by the GSFC. LADEE was part of the Lunar Quest Program, managed by NASA Marshall Space Flight Center.

LADEE addressed objectives that were not currently covered by other US or international efforts. LADEE's success also demonstrated the effectiveness of a low-cost, rapid

Fig. 1 LADEE spacecraft and
instport instrument locations
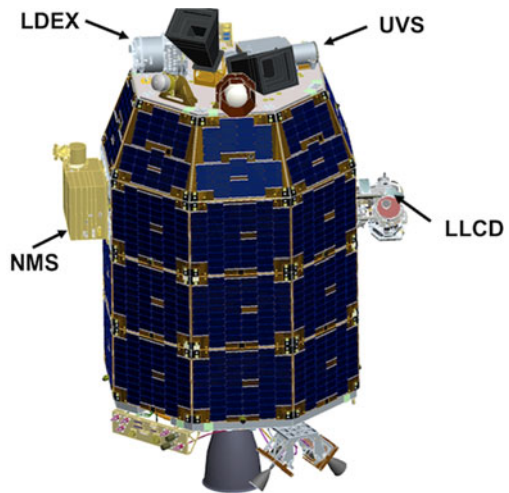
development program, utilizing a modular bus design. LADEE also ushered in use of the
Minotaur V launch vehicle for future lunar and other missions.

3.1 LADEE Spacecraft

The LADEE spacecraft bus design, derived from the Modular Common Spacecraft Bus
architecture, is a small, low-cost spacecraft architecture designed to deliver scientifically
and technically useful payloads to a variety of locations including lunar orbit. The space-
craft bus is a modular bus design that can be configured for a variety of mission objectives.
Figure 1 shows the spacecraft bus in the LADEE configuration, with the instruments at-
tached.

3.1.1 Modular Common Bus Project Guidelines

Since the Common Bus was designed to accomplish a variety of missions, it was designed
independently of any particular payload. The original development guidelines are listed be-
low:

SSO-1: Develop missions with destinations within the inner solar system, with destinations
such as lunar orbit, lunar surface, earth-moon lagrange points, and near earth objects
(NEOs).
SSO-2: Develop low-cost missions. This includes costs for small spacecraft development,
launch vehicle, mission specific services/integration, instruments, operations, & re-
serves.
SSO-3: Utilize cost effective launch vehicles and launch opportunities (e.g., Minotaur V,
ESPA).
SSO-4: Develop missions within a short (<36-month) period.
SSO-5: Use a "Design-to-Capability" approach.
SSO-6: Manage projects as a NASA Category III, Risk Classification D Mission.
SSO-7: Use the following priority in hardware selection:

   (A) Existing hardware with space flight history
   (B) Existing hardware designed for space flight

Fig. 2 LADEE Bus Modules
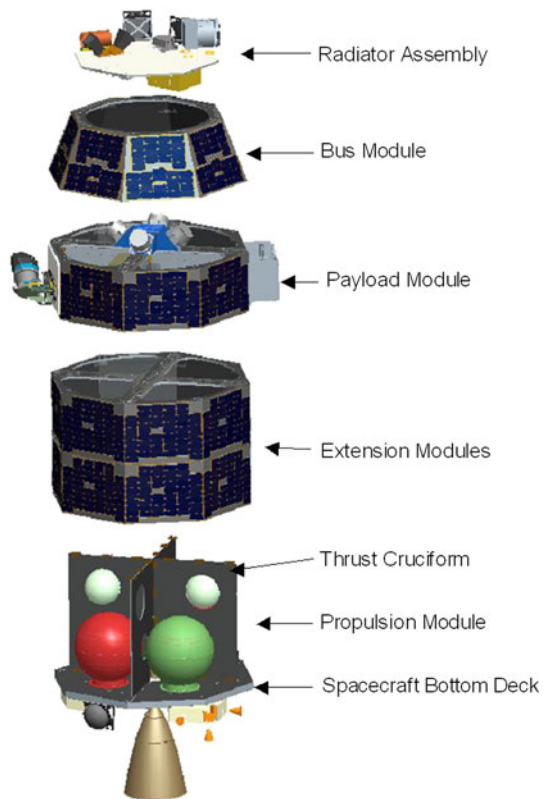
(C) Appropriate commercial-off-the-shelf (COTS) hardware designed for space
(D) New design

SSO-8: Utilize technologies developed by other government technology programs.
SSO-9: Develop and operate multiple simultaneous projects that are appropriately phased.

3.1.2 Design Overview

The spacecraft bus was a lightweight carbon composite structure designed to accommodate launch loads and provide attenuation of impact loads. It was also designed for ease of manufacturing and assembly. The modularity of the design was intended not only for multiple mission configurations but also parallelism in development and assembly. The system-level components were drawn from low-cost flight-proven product lines.

For LADEE, the spacecraft bus modules consisted of: (1) the Radiator Module, which carried the avionics, electrical system, and attitude sensors, (2) the Bus Module, (3) the Payload Module, which carried the two largest instruments, (4) the Extension Module, which housed the propulsion system, and (5) the Propulsion Module. The bus design is shown schematically in Fig. 2.

One prominent characteristic of the bus design is that the solar arrays are body-mounted and fixed. While this arrangement reduces the available power, it eliminates deployment and articulation mechanisms, which eliminates several failure modes. It also ensures power production in almost any attitude, which enables very robust safe modes. This design also

LADEE Bus Architecture Functional Block Diagram
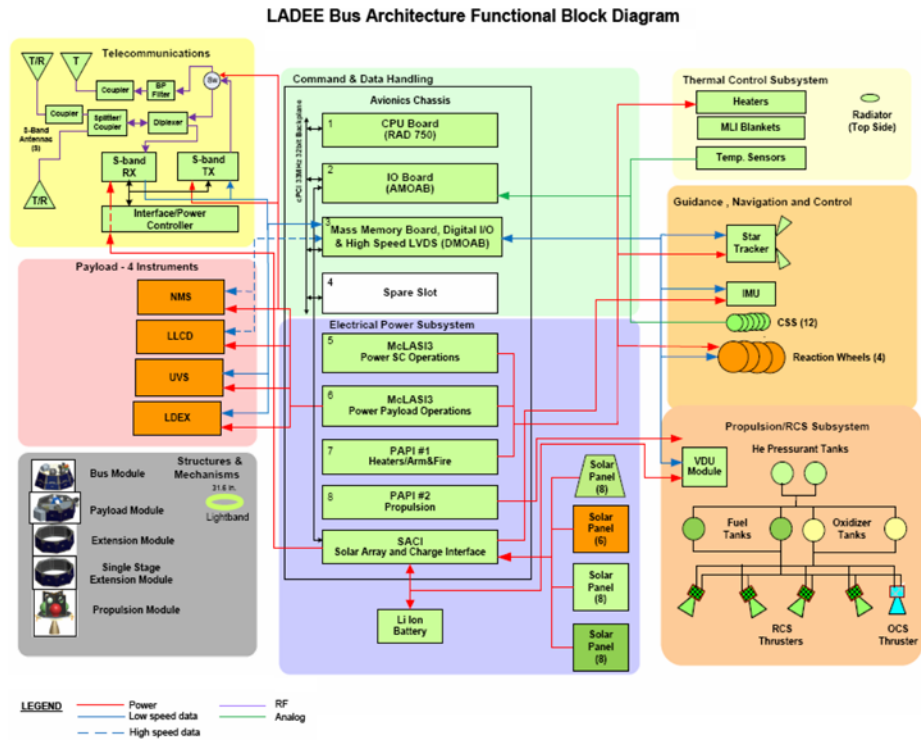
Fig. 3 LADEE System Block Diagram

allowed spacecraft attitude to be used for thermal control, and eliminated a hot and a cold side, which minimized the need for heater power. The spacecraft could be flown in either a spinner or 3-axis control mode.

3.1.3 System Diagram

Figure 3 shows the LADEE system block diagram. The flight avionics packages consisted of a commercially available 8-slot 3U cPCI integrated avionics system providing the following functions:

- Command & Data Handling Avionics
- Power Distribution
- Solar Array and Battery Charge Management
- Pyrotechnic Actuation

A separate electronics box in the Propulsion Module handled the valve driver actuation. The power system consisted of an array of body-fixed solar panels, connected to batteries through the solar array control card within the avionics chassis. The body-fixed array design minimized articulation on the spacecraft bus. LADEE's solar array consisted of 22 panels (each with 22.3 cm^2 cells) on the Payload Module, Extension Module and Single Stage Extension, as well as 8 panels on the bus module (each with 27.5 cm^2 cells). For typical LADEE science orbit attitudes, the arrays provided between 260 and 295 W. The electrical power subsystem included a battery with heritage on a number of missions; the vendor was

Table 2 LADEE Propulsion Fluids Summary

Fluid	Beginning of Mission		End of Nominal Science Mission	
	Mass (kg)	Pressure (psia)	Mass (kg)	Pressure (psia)
Fuel (MMH)	51.2	250	0.9	160
Oxidizer (N_2O_4)	82.1	250	1.5	160
Pressurant (He_2)	0.26	3500	0.28	345

ABSL Power Solutions. LADEE's battery had a 24 A-hr capacity, 691 Wh energy, minimum and maximum voltage of 20 and 33.6 V respectively. Its mass was 6.5 kg.

The propulsion system was a bipropellant propulsion system consisting of a main thruster, four attitude control thrusters, two fuel tanks, two oxidizer tanks, two pressurant tanks, an ordnance valve driver box, and associated tubing and cabling. The propulsion fluids parameters are shown in Table 2. Table 3 shows a summary of the propulsion maneuvers over the course of the mission. Total delta-V for the mission was 1134.6 m/sec. At impact the propulsion system had an estimated <8 % fill fraction. The largest and longest burn, Lunar Orbit Insertion-1, used the Orbit Control System thruster, which fired for 252.6 sec with a delta-V of 330.5 m/sec. After achieving the nominal science orbit on 21 November 2013, all orbit maintenance maneuvers (OMMs) were carried out using the smaller reaction control system thrusters. The longest of these, OMM-21, was 80 sec in duration.

The spacecraft bus communications system consisted of a modern architecture and modular design. The radio had separate receiver, transmitter and HPA modules and produced 5 Watts of RF transmitter power with flexible transmission power modes.

The spacecraft used an evolved Omni-directional/Medium Gain antenna design, developed at ARC, to achieve omni-directional coverage with a smaller area of medium gain response. At lunar distances, downlink on the omni antennas was typically 8 kbit/sec, and on the medium gain antennas 128 kbit/sec. Uplink was 8 kbit/sec through the omnis.

The avionics, batteries, attitude sensors, and two of the smaller science instruments are integrated into the Radiator Assembly (see Fig. 4). This arrangement simplifies integration and testing.

The two larger instruments (NMS and LLCD) were mounted on the Payload Module on opposite sides to balance the center of mass. The reaction wheels, in a pyramid configuration, were also attached to the Payload Module. Figure 5 shows the layout of the Payload Module.

The LADEE wet mass at launch was 375.5 kg, of which 134.8 kg was propellant. The remaining dry mass of 240.7 kg was comprised of 49.6 kg for the instruments/payload, and 191.1 kg of spacecraft bus.

4 Mission System Architecture

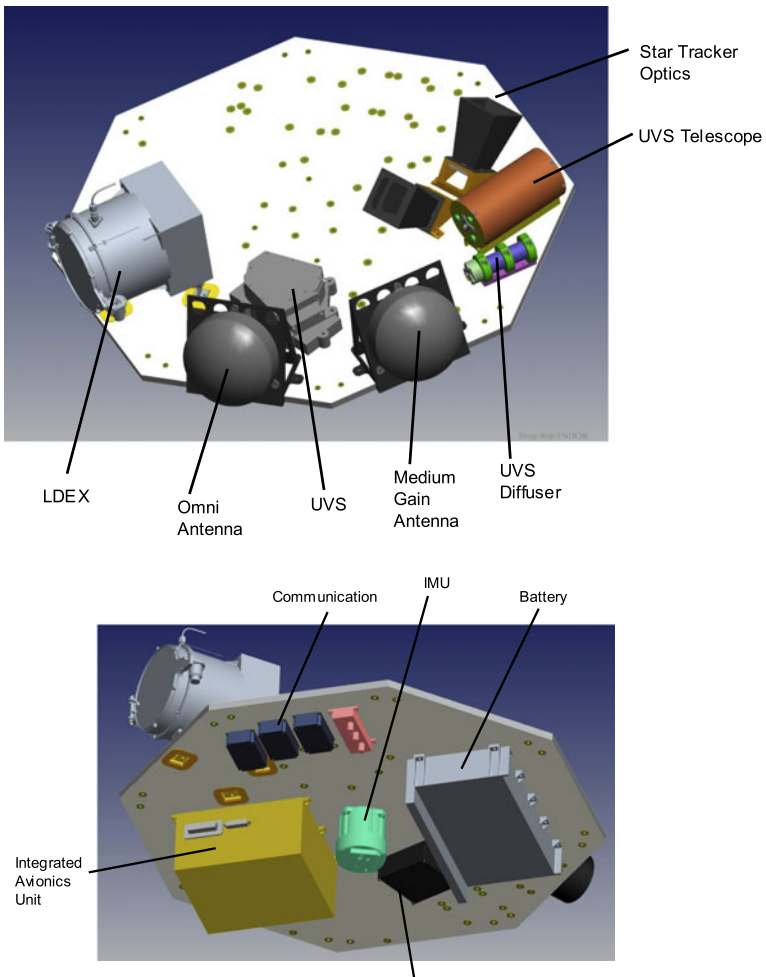The ground system was composed of the ground-based elements dispersed across the NASA centers and facilities. The LADEE Mission used the Mission Operations Center (MOC) located at ARC in Moffett Field, California. The project's Science Operations Center (SOC) was located at GSFC in Greenbelt, MD. LADEE used all three Deep Space Network stations in order to maintain a cost-effective mission operations staffing schedule throughout the

Table 3 LADEE Maneuver Summary and Statistics

Mnvr	Maneuver Type	Pre Mnvr Prop Mass (kg)	Pre Mnvr Fill Fraction	RCS Burn Duration (sec)	Actual DV (m/s)	Performance
AM1b	OCS PR	134.50	1.00	20.90	NA	NA
PM1	OCS PR	133.44	0.99	20.90	16.760	−1.23 %
PM2	OCS PR	131.54	0.97	20.90	17.490	0.00 %
TCM1	RCS PR	129.02	0.96	5.60	0.922	4.20 %
LOI1	OCS PR	128.88	0.95	20.90	330.500	−0.90 %
LOI2	OCS PR	90.97	0.67	20.90	291.045	−0.63 %
LOI3	OCS PR	60.78	0.45	20.90	244.230	0.35 %
OLM3	OCS PR	37.72	0.27	20.90	35.430	−0.26 %
OLM4	OCS PR	34.29	0.25	20.90	33.890	−0.60 %
OMM01	RCS BD	31.03	0.23	31.00	6.830	5.70 %
OMM02	RCS BD	30.47	0.22	48.60	10.710	0.25 %
OMM03	RCS BD	29.07	0.21	21.20	4.603	−1.30 %
OMM04	RCS BD	28.45	0.20	23.10	5.048	0.15 %
OMM05	RCS BD	27.40	0.20	29.60	6.428	−1.00 %
OMM06	RCS BD	26.54	0.19	26.90	5.838	−0.15 %
OMM07	RCS BD	25.77	0.19	39.10	8.479	−0.53 %
OMM08	RCS BD	24.64	0.18	24.70	5.358	0.75 %
OMM09	RCS BD	23.21	0.17	16.70	3.594	−0.07 %
OMM10	RCS BD	22.72	0.17	28.10	6.054	−0.21 %
OMM11	RCS BD	21.93	0.16	30.30	6.526	0.40 %
OMM12	RCS BD	21.07	0.16	41.80	8.931	−0.24 %
OMM13	RCS BD	19.91	0.15	29.00	6.229	0.21 %
OMM14	RCS BD	19.09	0.14	28.30	6.045	0.08 %
OMM15	RCS BD	18.31	0.14	24.40	5.212	0.50 %
OMM16	RCS BD	17.63	0.13	25.80	5.482	−0.07 %
OMM17	RCS BD	16.92	0.13	42.30	9.013	0.62 %
OMM18	RCS BD	15.76	0.12	28.50	6.055	0.13 %
OMM19	RCS BD	14.98	0.11	32.90	6.969	−0.03 %
OMM20	RCS BD	14.03	0.10	23.00	4.859	0.39 %
OMM21	RCS BD	13.41	0.10	80.10	16.945	0.02 %
OMM22	RCS BD	11.25	0.08	46.30	9.747	0.15 %

lunar month (instead of using White Sands, for example, which would require LADEE MOS engineers to work changing shifts).

The data from the ground station(s) was routed to the MOC at ARC for processing, distribution and data storage/archiving. Science and instrument data, along with processed spacecraft health and safety data, was transmitted to the GSFC SOC. The SOC pushed the raw telemetry files to the Instrument Operations Centers (IOCs). Figure 6 shows a schematic representation of the Mission System Architecture and command and data flow within it.

Star Tracker
Optics

UVS Telescope

LDEX

Omni
Antenna

UVS

Medium
Gain
Antenna

UVS
Diffuser

Communication   IMU   Battery

Integrated
Avionics
Unit

Fig. 4 (*Top*) Radiator assembly top view. (*Bottom*) Radiator assembly bottom view

Fig. 5 Payload Module
Configuration

Reaction Wheel
Pyramid

LC Optical
Head Plate

Ballast

LC Control

LC Optical
Head

LC Modem

NMS
Instrument

14
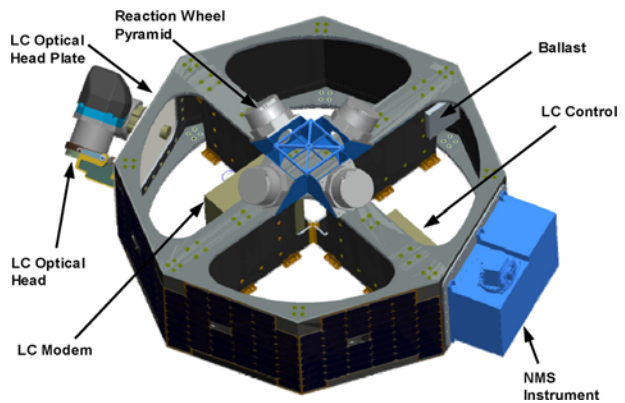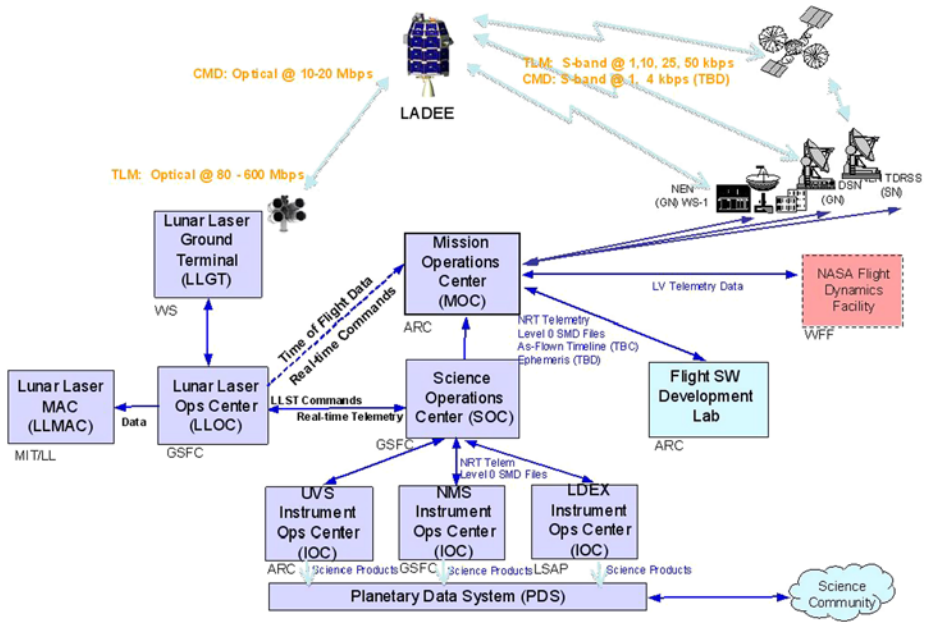
Fig. 6 The Mission System Architecture showing data flow paths

Table 4 LADEE Payload Parameters

Instrument	NMS	LDEX	UVS	LLST
Mass	11.8 kg	3.6 kg	3.6 kg	30.7 kg
Power	36 W	$\leq$5.0 W	13 W (avg)	141 W (operating)
Sensitivity	$\sim 2 \times 10^{-2}$ (counts/s)/(particles/cc)	0.3 μm radius @ 1.6 km/s	Mean noise-equivalent power $\sim$45 R/nm	
Data	3.5 kbit/s	$\leq$200 kbit/s	3.3 kbit/s for limb viewing activities 14.7 kbit/s occultation activities	622 Mbits/s downlink, 20 Mbit/s uplink

4.1 Instrument Payload

LADEE carried three science instruments and a technology demonstration. The payload parameters are shown in Table 4.

4.1.1 Neutral Mass Spectrometer

The LADEE NMS measured the mass distribution of neutral species over a mass range between 2–150 Daltons. NMS drew its design from similar mass spectrometers developed at GSFC for the MSL/SAM, Cassini Orbiter, CONTOUR, and MAVEN missions. The NMS used a dual ion source that provided a means to measure both surface reactive and inert

species with a quadrupole mass spectrometer. For inert species, NMS achieved sensitivities of approximately 2×10^{-2} (counts/sec)/(particle/cm^3).

NMS had two ways of sampling the lunar exosphere: (1) the closed ion source used a small aperture in a spherical antechamber, and a portion of the intercepted gas molecules is ionized and focused into the mass analyzer; (2) the open source was designed to allow analysis of more reactive species by collimating the incoming beam of neutral molecules, ionizing a subset of them with a different electron beam, and passing these to the mass. The closed source approach enables high sensitivity for nonreactive species, while the open source permits analysis of metals and other reactive species.

NMS was operated in several modes: RAM pointed the NMS aperture in the direction of LADEE's orbital motion—this was used to track the noble gases; TILT mode called for LADEE to point the NMS field of view downward 30 deg off ram, which enabled NMS to measure more energetic sputtered species; WAKE mode was performed when LADEE pointed the aperture in the anti-ram direction, permitting measurements of instrument background when essentially no atmospheric gas entered the instrument; ION mode pointed the aperture toward ecliptic normal, looking for exospheric ions that have been picked up in the solar wind electric field.

At low altitudes, NMS was capable of measuring the abundance of gases such as ^{40}Ar, which may indicate internal geophysical processes at the Moon. Measurements of He are being used to understand the importance of the solar wind in the generation and dynamics of the helium exosphere. NMS was also designed to detect refractory elements in the exosphere (Si, Al, Mg, Ca, Ti, Fe), as well as Na and K, which may be indicative of more energetic processes acting on the lunar surface such as sputtering and impact vaporization. In terms of volatiles, NMS could detect H_2O, OH and CO. There is also an ion-detection mode. Ultimate sensitivity for detection of most species is in the range of a few particles/cc. A complete instrument description is provided by Mahaffy et al. (2014).

4.1.2 Ultraviolet/Visible Spectrometer

The UVS instrument was a next-generation, high-reliability version of the LCROSS UV-Vis spectrometer, spanning 250–800 nm wavelength, with high (<1 nm) spectral resolution. UVS was designed to be used in both limb and occultation mode. In limb mode, UVS searched for resonant scattering emissions from exospheric species as well as scattering of sunlight from lunar dust. In occultation mode, UVS searched for scattering of sunlight by dust using a separate solar viewing optic. UVS could detect volatiles such as OH, K, Li, Ba, and Na, as well as more refractory elements such as Al, Ca, Si, Ti, and Mg. UVS could also detect water (H_2O) in several of its positively ionized states. A complete instrument description is provided by Colaprete et al. (2014).

UVS consisted of two optics, a spectrometer with data processing and command/telemetry IO, optical fibers, integrated mechanical and thermal structure and a single-deployment aperture door. The fore-optics were a catadioptric telescope of 76.2 mm aperture and 1-degree field of view (FOV), and a separate solar-viewing element consisting of a series of concentric aperture disks defining a 1-deg FOV, followed by a ground fused silica diffuser. This diffuser attenuated the solar input to an acceptable level and provided an extended light source to the end of the fiber optic cable. The telescope system was designed to capture light from exospheric atomic and molecular emissions in the UV and visible, as well as scattered light from dust. The solar viewer was designed for measurements of solar radiance extinction as the light path from the sun to the instrument approached the lunar surface in the course of an orbit.

UVS used several modes of operation. *Limb viewing* activities involved alternately staring at a fixed grazing altitude above the limb, or "nodding" so that the grazing altitude varied during the activity. Limb viewing was usually done approximately parallel to the ecliptic plane, but sometimes viewing to the north or south to observe latitudinal variations. *Sodium Tail* observations pointed the telescope at an angle off anti-sunward, viewing the sun-illuminated gas but from the nightside part of LADEE's orbit. *Occultation* activities used the solar viewer aimed exactly at the solar disk, to look for extinction of sunlight by exospheric dust as the spacecraft moved from day to night. Other activities were performed to monitor background levels and to check for stray light contributions.

4.1.3 Lunar Dust Experiment

LDEX was an impact ionization dust detector. Each dust particle impact on a large hemispherical target created a cloud of electron and ion pairs. The latter are focused and accelerated in an electric field and detected by a micro-channel plate. The LDEX design heritage includes instruments aboard the HEOS 2, Ulysses, Galileo and Cassini missions. It was designed to operate at the relatively low LADEE orbital speed of 1.6 km/s and altitudes of 50 km and below, and was capable of detecting particles with radii ∼0.7–5 μm as single impacts. The presence of even smaller particles, down to 0.1 μm, could also be detected by LDEX through their collective signal. The LDEX aperture was 12.4 cm in diameter, and had an acceptance angle of ±68 deg off the central axis of the instrument. A complete instrument description is provided by Horanyi et al. (2014).

Nominal LDEX operations were carried out when LADEE was in ram attitude, and were generally scheduled whenever it was safe to operate, that is, when the LDEX FOV did not include the sun. However, the LDEX team also wanted off-ram measurements, including anti-ram measurements to determine background levels. Because of the low LDEX power requirements and desire for of sun-safe, off-ram measurements, it had a higher duty cycle than the other instruments.

4.1.4 Lunar Laser Communications Demonstration

LLCD was a technology demonstration designed to test the feasibility of high bandwidth optical communications from deep space. It consisted of the Lunar Laser Space Terminal (LLST, the hardware on LADEE), and the Lunar Laser Ground Terminals at White Sands, NM. LLCD also used the Lunar Lasercom OCTL Terminal (LLOT), at the NASA Jet Propulsion Laboratory's Optical Communications Telescope Laboratory at Table Mountain in California, and the Lunar Lasercomm Optical Ground System (LLOGS), residing at European Space Agency's OGS on Tenerife, the Canary Islands. All operations were coordinated from the Lunar Lasercomm Operations Center (LLOC) at the MIT Lincoln Laboratory in Lexington, MA.

The LLST consisted of an optical module housing the laser system and telescope, and two other modules, a modem and the controller electronics.

LLCD was operated during the Commissioning Phase, on a schedule that alternated blocks of days with science instrument commissioning. An LLCD operation consisted include 13 to 15 minutes of "on" time of the LLST with no science instruments. Power constraints limited the number of LLCD operations that could be run in sequence before a dedicated orbit for recharging the batteries must occur. During the technology demonstration, the spacecraft had to be pointed at the Earth with an accuracy error of <1 degree. The LLCD achieved downlinks as high as 622 Mbits/sec, and received uplink at 20 Mbits/sec. For more detail on LLCD, see Boroson and Robinson (2014).

Fig. 7 LADEE phasing loops
(approximate periods of 6, 8, and
10 days, respectively) and
translunar cruise segment. P1, P2
and P3, and A1, A2 and A3 refer
to phasing orbit perigees and
apogees
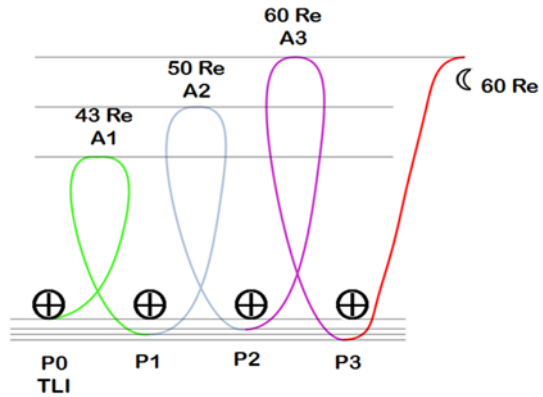
4.2 Mission Phases

The LADEE mission profile consisted of the following major phases: launch, ascent, activation & checkout, phasing orbits, lunar transfer, lunar orbit acquisition, commissioning, nominal science operations, extended science, and lunar impact.

4.2.1 Launch

Launch occurred on September 7th, 2013 at 03:51 UTC, from WFF on the first Minotaur V launch vehicle. The ascent phase lasted 24 minutes at which point LADEE separated from the last (5th) stage of the vehicle. This was followed by a day of spacecraft activation and checkout in a low-Earth orbit, culminating in a maneuver to increase the LADEE apogee into the Earth-centered phasing loop orbits.

4.2.2 Phasing Loops

After ascent, LADEE was inserted into Earth-centric phasing loop orbits on September 7th, 2013, ranging in period from 6 to 10 days each. LADEE executed a total of three phasing orbits over a period of almost 24 days prior to a maneuver that placed LADEE into a translunar trajectory (Fig. 7). The purpose of the phasing loops was to accommodate the potential launch dispersions arising from performance variations in the five solid rocket stages of the Minotaur V. If the launch vehicle under- or over-performed, LADEE would use its own propulsion to compensate, adjusting the orbit in such a way as to arrive at the Moon with the proper approach geometry at the correct time. As it happened, the Minotaur V launch was essentially perfect, and LADEE's phasing loop maneuvers were minimal. This resulted in a substantial fuel margin for LADEE at the Moon.

4.2.3 Lunar Transfer & Acquisition

Initiation of the trans-lunar trajectory began on October 1, 2013 at 10:55 UTC. The translunar trajectory phase ended with the lunar orbit acquisition phase, which commenced with the first lunar orbit insertion (LOI-1) burn that captured LADEE into lunar orbit. Two subsequent LOI maneuvers sequentially lowered the lunar orbit from the arrival hyperbola to a 250 km circular orbit as shown in Fig. 8. During this phase LADEE approached the Moon while over the far side (white line) in the figure shown, and was captured into a 24 hour orbit
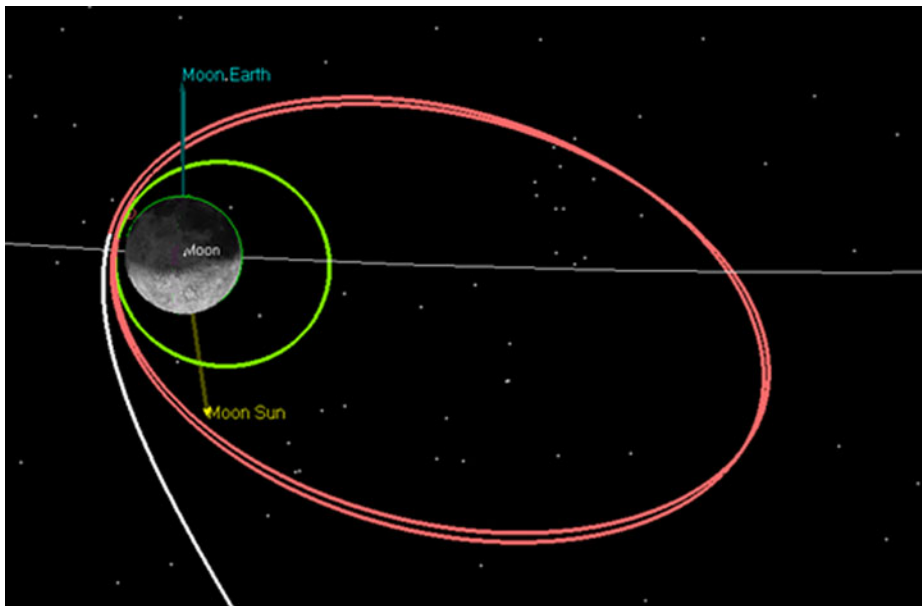
Fig. 8 LOI phase of the LADEE mission. Last phasing loop (*white*), LOI-1 orbits (*orange*), LOI-2 orbits (green), and LOI-3 transition to the commissioning orbit (*darker green semi-circle* on the upper half of the Moon)

with a 155786 km apoapsis where the spacecraft remained for 3 revolutions lasting 3 days. LOI-2 lowered the orbit down to a 4 hour orbit with a 2184 km apoapsis. Finally, LOI-3 lowered the orbit down to a 250 km × 250 km lunar commissioning orbit on November 21st, 2013 at 04:53 UTC (see Fig. 8).

4.2.4 Commissioning Phase

During the commissioning phase the LLCD technology demonstration and basic checkout of the science payload was completed. The prime operational phase of the LLCD was conducted during the first 30 days while LADEE was in the 250 km circular orbit at 157° inclination. During this time, science payload activation and initial checkout was also initiated. During the last 10 days of the commissioning period, the LADEE periapsis was lowered to 50 km while science payload checkout activities continued, and the first measurements of the lunar exosphere and dust properties were performed. The commissioning phase ended on November 21st, 2013, when LADEE was maneuvered into the science orbit. Figure 9 shows the orbit altitudes (perigee and apogee altitudes) as a function of mission phase from the commissioning phase through impact.

4.2.5 Science Phase

The primary science phase began on November 21st, 2013 at 04:53 UTC and lasted 100 days. Orbit Maintenance Maneuvers (OMMs) were used during this period to keep the periapsis altitude at or below 50 km and the apoapsis altitude below 150 km to the extent possible. The orbit design with OMMs during the science phase is shown in Fig. 9 OMMs were designed to maintain the periapsis over the lunar sunrise terminator.
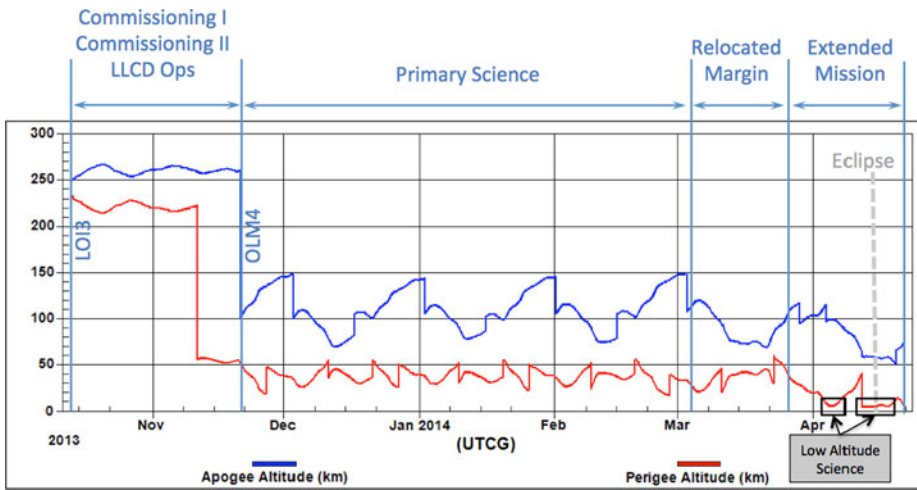
**Fig. 9** LADEE orbit altitude profile throughout the commissioning, science, and extended science mission phases. Abrupt changes in periapsis (*red*) or apoapsis (*blue*) altitudes are due to Orbit Maintenance Maneuvers, OMMs, that manage the preferred LADEE science orbit periapsis over the sunrise terminator

Fig. 10 Two dimensional histogram of LADEE orbital coverage in altitude and solar phase angle (and local time) over the course of the nominal and extended science phases. Color scale is in total minutes per bin. Note LADEE's concentrated sampling over a particular area of interest, the sunrise terminator
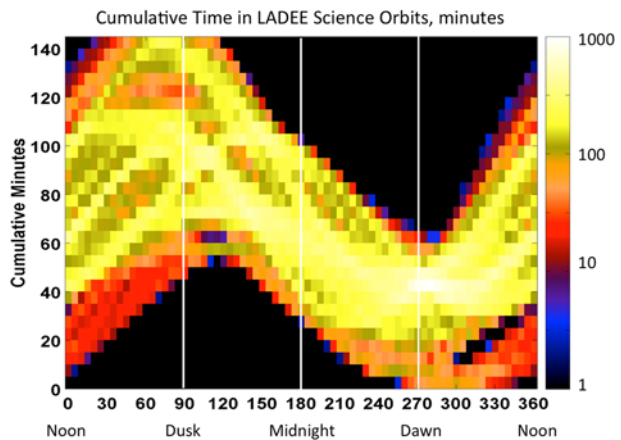
4.2.6 Extended Science Phase

The extended science phase began on March 1st, 04:53 UTC. During this time the orbit periapsis was allowed to decrease in order to achieve low-altitude science observations. An eclipse period was encountered on April 15th, which precluded science activities starting on April 14th, 22:00 UTC. Science observations resumed on April 15th, 16:53 UTC and continued through the end of the extended science phase on April 18th, 2014.

Figure 10 shows LADEE's orbital coverage in local time and altitude (not to scale) for the prime plus extended science phases. Color code is number of minutes spent within each 5 deg by 5 km bin.

4.2.7 Impact

The planned impact of LADEE into the Moon took place on April 18, 2014 at 04:31:47 UTC at 11.840 deg latitude and −93.252 deg longitude (Moon-centered Mean Earth coordinates). This location is on the eastern outer rim of Sundman V, a 19-km diameter impact crater centered at 11.9° N, 93.5° W.

5 LADEE Science Planning & Operations

A number of engineering constraints governed the way LADEE science activities were planned and executed. As can be seen in Fig. 1, the LADEE science instruments were body mounted, and the required instrument pointing and stability was accomplished with the spacecraft attitude control system. Both NMS and LDEX were usually operated in the preferred ram orientation, with their boresights aligned with the velocity vector of the spacecraft in orbit. However, at times both made use of off-ram activities: for example NMS would monitor instrument backgrounds by operating in an anti-ram, or wake, attitude during which no exospheric molecules could enter the instrument aperture. LDEX made use of these same anti-ram attitudes to check impact flux and background currents when no elevated dust could possibly be observed. UVS was most often operated in a limb-stare mode, with the telescope field of view fixed on a selectable grazing point altitude above the limb. UVS also performed occultation activities with its solar viewer optic, measuring the extinction of sunlight due to possible dust above the lunar surface. Thus, UVS activities generally placed the spacecraft attitude several degrees to many degrees off ram, generally outside the useful range for NMS measurements.

Added to these mutually exclusive science attitudes were a number of other engineering and operations constraints and flight rules that defined when the instruments could not operate. For example, LADEE's estimated orbit-average energy budget precluded the simultaneous operation of NMS and UVS (LDEX, with a lower power draw, could be operated simultaneously). To preserve the highest quality tracking data for orbit determination, off-ram activities were prohibited during tracking passes (but LDEX and NMS ram activities were allowed). During real time operations, when spacecraft engineering, data downloads and command sequence uploads took place, the spacecraft was in an attitude that pointed LADEE's medium gain antenna (MGA) at the Earth; no science activities were permitted at these times.

This mutual exclusion of both attitude and energy constraints led to instrument operations plans that alternated UVS and NMS activities when other engineering activities did not preclude such operations. LDEX operations were instantiated for those times when the instrument field of view did not include the sun, and the instrument could be safely operated.

The participants in the activity planning process included the Mission Planning and Sequencing Team, the Science Operations Center (at Goddard Space Flight Center), the Project Scientist and Deputy, and the instrument operations teams. All participants used a common planning tool, the LADEE Activity Scheduling System or LASS, and managed version control of activity plans through a Sventon version control system maintained by the Mission Operations Center at ARC.

LADEE's science planning process began with the mission planners and spacecraft engineering teams building a lunation plan. This roughly 1-month plan captured all the key engineering activities such as MGA passes for real time supports, and tracking passes for orbit determination, placeholders for absolute time sequence (ATS) uploads and executions,

as well as many other real time activities. These lunation plans also carried placeholders for the approximately once-per-week orbit maintenance maneuvers (OMMs) that were required to keep LADEE flying at the desired altitudes for science purposes.

From each lunation plan was drawn an engineering skeletal plan spanning 10 or 11 days; ESPs captured spacecraft engineering activities with higher temporal fidelity, based on updated ephemerides. The ESPs were used for scheduling and negotiating ground station coverage from the Deep Space Network. ESPs also formed the basis for an Orbit Allocation Plan (OAP), created by Project Science, to provide guidance to the instrument teams in planning their activities for a strategic period covering seven days.

Guided by the OAPs, the individual instrument teams would make activity requests by way of Instrument Activity Plans, one from each instrument team, that would then be integrated together and deconflicted at a twice-weekly Science Operations Working Group meeting, led by Project Science and the Science Operations Center. This meeting resulted in a Strategic Activity Plan (SAP), a seven-day plan with detailed instrument operations equitably distributed to meet science requirements, and a new Orbit Allocation Plan for the next block of time. The Mission Planning and Sequencing team would extract 80-hour pieces out of the SAP to create a Tactical Activity Plan (TAP) with updated ephemerides and engineering activity times. TAPs were reviewed by the mission operations teams and Project Science before and after being turned into command plans and ATS files for upload to the spacecraft.

The science planning and execution process was highly effective and resulted in far more science activities than the minimum required. Figure 11 shows how each of the three science instruments far exceeded the minimum number of daily activities necessary to meet requirements. LDEX typically achieved at least eight sunrise crossing activities every day; the minimum required was one every twelve hours, or two per day. NMS regularly ran three or four sunrise crossing activities to monitor ^{40}Ar and He (and other species), as well as other focused activities aimed at either sputtered secondary particles or ions across the mass range. UVS performed three to four two-limb activities every day, to monitor Na and K systematically across noon and either the sunrise or sunset terminator; this permitted UVS characterization of the spatial and temporal evolution of the alkali exospheres. UVS also performed regular solar extinction measurements in a search for dust. Cumulative data volumes from science instruments (Sept. 7, 2013 through April 18, 2014) are as follows: NMS: 2.7 Mbyte housekeeping data, 45.6 Mbyte science data; UVS: 2.4 Mbyte housekeeping data, 212.9 Mbyte science data; LDEX: 7.4 Mbyte housekeeping data, 410.5 Mbyte science data.

6 Conclusions

The LADEE mission was in every way a success. The science instruments aboard LADEE have acquired more than sufficient data to meet the mission Level 1 science requirements. These data are being analyzed and early results indicate that the exospheric science objectives were met in the 100-day prime science mission phase. Orbital measurements were successfully acquired that characterize the density, spatial- and size-distribution of exospheric dust. Early results indicate that objectives have been exceeded. Exospheric gas and dust science data were also acquired at unprecedented low altitudes in the 48-day extended science mission prior to impact. The Lunar Laser Communication Demonstration (LLCD) experiment was a success, with the instrument achieving the full 622 Mbps downlink and 20 Mbps uplink goals. The LADEE bus design and development demonstrated the effective use of a low-cost reusable spacecraft architecture that can meet the needs of specific planetary science missions. LADEE demonstrated the utility of the Minotaur V as a launch vehicle for planetary missions.
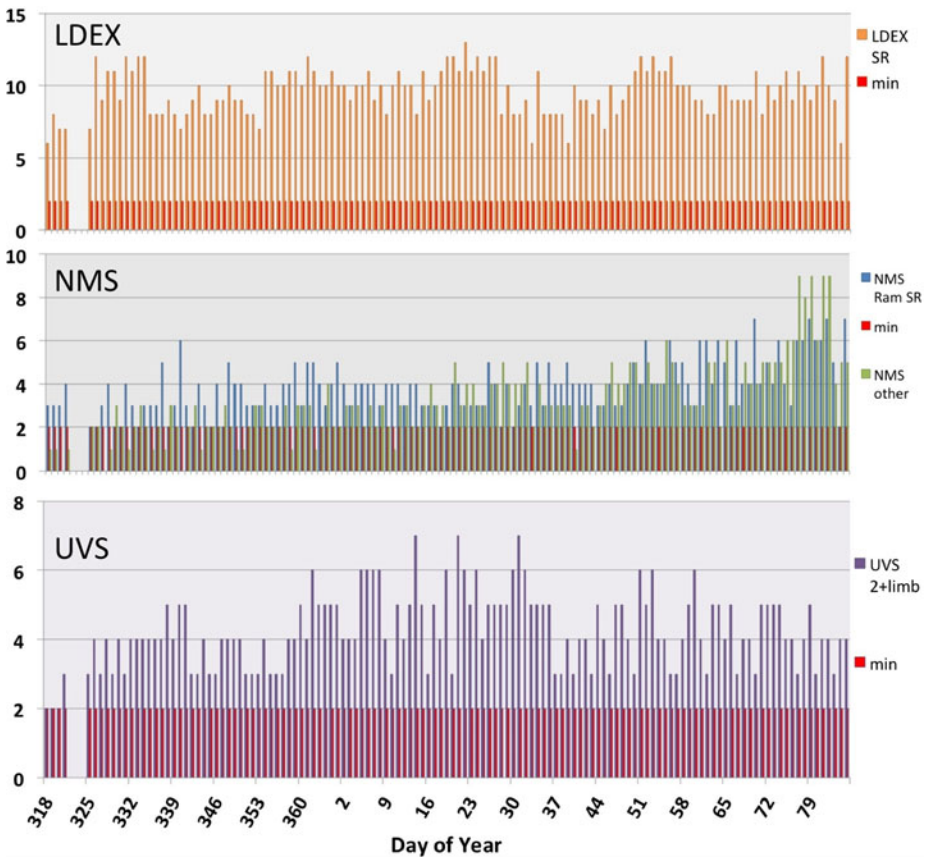
Fig. 11 The daily number of science operations carried out by LADEE's three science instruments during the mission. For each plot, the minimum number of activities is two per day, separated by 12 hours to meet the cadence requirement. Each instrument exceeded this requirement, particularly later in the science mission. "SR" for LDEX and NMS refers to the sunrise terminator crossing, necessary to meet Level 1 requirements

Preliminary data analysis has revealed the following: LADEE found that the three most abundant exospheric constituents are noble gases: argon, neon, and helium.

We now know that the two most abundant, neon and helium, come from the solar wind. Helium is far more abundant than neon in the solar wind, so it appears that helium delivery is balanced by significant thermal loss, whereas neon establishes a near-equilibrium situation with the slow loss process being photoionization.

The third noble gas, ^{40}Ar, comes from the lunar interior and may provide information on deep partial melt in the Moon's mantle. There is very clear evidence of a preferred location on the near side where enhanced ^{40}Ar densities occur. It is not yet known if this is due to some physical aspect of the lunar surface or if the diffusion rates are higher in some locations.

LADEE systematically monitored two minor but very important species, sodium and potassium, and found they vary with many factors. We now know that sodium responds to meteoroid input—when the Earth-Moon system passed through the Geminid meteoroid stream, UVS detected an increase the sodium density. The Moon's sodium and potassium exospheres seem to diminish as the Moon approaches Full phase. As the Moon approaches

Full, it leaves the solar wind and enters the geomagnetic tail. Here, sputtering by solar wind is absent, and sodium and potassium atoms on the surface are more protected. As soon as the Moon leaves the geomagnetic tail, it returns to the solar wind again and there follows a rapid rise in sodium and potassium in the exosphere. Other species being investigated include H_2, O, OH, H_2O, CO, Mg, Al, CO_2, Ti.

LADEE discovered a lunar dust exosphere. The dust appears to be on the *morning* side of the Moon, where meteoroids tend to impact because of the 30 km/sec motion of the Earth-Moon system around the Sun. It appears this dust population is mainly ejecta from high-speed micrometeoroid particles impacting the lunar surface. The observed dust particles are very small, and extremely tenuous in density: from 0.6 μm up to a few μm, at densities of 10^{-4} particles per meter cubed, and highest near the surface. LADEE did not find evidence of an electrostatically levitated population of dust. If present, such a population is far below the densities theoretically predicted, and much less important than the dust ejected by micrometeoroid impacts.

References

J. Benson, J.W. Freeman, H.K. Hills, The lunar terminator ionosphere, in *6th Proc. Lunar. Sci. Conf.* (1975), pp. 3013–3021

D.M. Boroson, B.S. Robinson, The lunar laser communication demonstration: NASA's first step toward very high data rate support of science and exploration missions. Space Sci. Rev. (2014, this issue)

A. Colaprete et al., The LADEE ultraviolet/visible spectrometer. Space Sci. Rev. (2014)

J.C. Cook, S.A. Stern, C.C.C. Tsang, K. Retherford, G.R. Gladstone, P. Feldman, New upper limits on numerous atmospheric species in the native lunar atmosphere. Icarus **225**, 681–687 (2013)

P.D. Feldman, D.M. Hurley, K.D. Retherford, G.R. Gladstone, S.A. Stern, W. Pryor, J.Wm. Parker, D.E. Kaufmann, M.W. Davis, M.H. Versteeg, the LAMP Team, Temporal variability of lunar exospheric helium during January 2012 from LRO/LAMP. Icarus **221**, 854–858 (2012)

P.D. Feldman, D.A. Glenar, T.J. Stubbs, K.D. Retherford, G.R. Gladstone, P.F. Miles, T.K. Greathouse, D.E. Kaufmann, J.Wm. Parker, S.A. Stern, Upper limits for a lunar dust exosphere from far-ultraviolet spectroscopy by LRO/LAMP. Icarus **233**, 106–113 (2014)

J.W. Freeman Jr., H.K. Hills, The Apollo lunar surface water vapor event revisited. Geophys. Res. Lett. **18**(11), 2109–2112 (1991)

D.A. Glenar, T.J. Stubbs, J.E. McCoy, R.R. Vondrak, A reanalysis of the Apollo light scattering observations, and implications for lunar exospheric dust. Planet. Space Sci. **59**, 1695–1707 (2011)

P. Gorenstein, P. Bjorkholm, Detection of radon emanation from the crater Aristarchus by the Apollo 15 alpha particle spectrometer. Science **179**, 792–794 (1973)

R.R. Hodges Jr., F.S. Johnson, Lateral transport in planetary exospheres. J. Geophys. Res. **73**(23), 7307–7317 (1968)

R.R. Hodges, J.H. Hoffman, F.S. Johnson, The lunar atmosphere. Icarus **21**, 415 (1974)

M. Horanyi, Sternovsky, M. Lankton, C. Dumont, S. Gagnard, D. Gathright, E. Gruen, D. Hansen, D. James, S. Kempf, B. Lamprecht, R. Srama, J.R. Szalay, G. Wright, The Lunar Dust Experiment (LDEX) onboard the Lunar Atmosphere and Dust Environment Explorer (LADEE). Space Sci. Rev. (2014)

F.S. Johnson, Lunar atmosphere. Rev. Geophys. **9**(3), 813–823 (1971)

M. Kagitani, M. Taguchi, A. Yamazaki, I. Yoshikawa, G. Murakami, K. Yoshioka, S. Kameda, S. Okano, Variation in lunar sodium exosphere measured from lunar orbiter SELENE (Kaguya). Planet. Space Sci. **58**, 1660–1664 (2010)

R.M. Killen, W.-H. Ip, The surface-bounded atmospheres of Mercury and the Moon. Rev. Geophys. **37**(3), 361–406 (1999)

S.L. Lawson, W.C. Feldman, D.J. Lawrence, K.R. Moore, R.C. Elphic, R.D. Belian, S. Maurice, Recent outgassing from the lunar surface: The Lunar Prospector Alpha Particle Spectrometer. J. Geophys. Res. **110**, E09009 (2005). doi:10.1029/2005JE002433

P.R. Mahaffy, R. Richard Hodges, M. Benna, T. King, R. Arvey, M. Barciniak, M. Bendt, D. Carigan et al., The neutral mass spectrometer on the lunar atmosphere and dust environment explorer mission. Space Sci. Rev. (2014). doi:10.1007/s11214-014-0043-9

J.E. McCoy, Photometric studies of light scattering above the lunar terminator from Apollo solar corona photography, in *7th Proc. Lunar Sci. Conf.* (1976), pp. 515–517

M. Mendillo, B. Flynn, J. Baumgardner, Imaging experiments to detect an extended sodium atmosphere on the Moon. Adv. Space Res. **13**(10), 313–319 (1993)

A.E. Potter, T.H. Morgan, Discovery of sodium and potassium vapor in the atmosphere of the Moon. Science **241**, 675–680 (1988)

A.E. Potter, T.H. Morgan, Evidence for suprathermal sodium on Mercury. Adv. Space Res. **19**(10), 1571–1576 (1997)

A.E. Potter, R.M. Killen, T.H. Morgan, Variation of lunar sodium during passage of the Moon through the Earth's magnetotail. J. Geophys. Res. **105**, 15,073–15,084 (2000). doi:10.1029/1999JE001213

J.J. Rennilson, D.R. Criswell, Surveyor observations of lunar horizon glow. The Moon **10**, 121–142 (1974)

S.M. Smith, J.K. Wilson, J. Baumgardner, M. Mendillo, Discovery of the distant lunar sodium tail and its enhancement following the Leonid meteor shower of 1998. Geophys. Res. Lett. **26**(12), 1649–1652 (1999). doi:10.1029/1999GL900314

A.L. Sprague, R.W.H. Kozlowski, D.M. Hunten, W.K. Wells, F.A. Grosse, The sodium and potassium atmosphere of the Moon and its interaction with the surface. Icarus **96**, 27–42 (1992)

A.S. Stern, The lunar atmosphere: history, status, current problems, and context. Rev. Geophys. **37**, 453 (1999)

S.A. Stern, K.D. Retherford, C.C.C. Tsang, P.D. Feldman, W. Pryor, G.R. Gladstone, Lunar atmospheric helium detections by the LAMP UV spectrograph on the Lunar Reconnaissance Orbiter. Geophys. Res. Lett. **39**, L12202 (2012)

S.A. Stern, J.C. Cook, J.-Y. Chaufray, P.D. Feldman, G.R. Gladstone, K.D. Retherford, Lunar atmospheric H2 detections by the LAMP UV spectrograph on the Lunar Reconnaissance Orbiter. Icarus **226**, 1210–1213 (2013)

T. Stubbs, R. Vondrak, W. Farrell, A dynamic fountain model for lunar dust. Adv. Space Res. **37**, 59–66 (2006)

A.L. Tyler, R.W.H. Kozlowski, D.M. Hunten, Observations of sodium in the tenuous lunar atmosphere. Geophys. Res. Lett. **15**(10), 1141–1144 (1988)

J.K. Wilson, S.M. Smith, J. Baumgardner, M. Mendillo, Modeling an enhancement of the lunar sodium atmosphere and tail during the Leonid meteor shower of 1998. Geophys. Res. Lett. **26**(12), 1645–1648 (1999). doi:10.1029/1999GL900313

J.K. Wilson, M. Mendillo, H.E. Spence, Magnetospheric influence on the Moon's exosphere. J. Geophys. Res. **111**, A07207 (2006) doi:10.1029/2005JA011364

The Scientific Context for EXPLORATION of the MOON, Space Studies Board, Division on Engineering and Physical Sciences, National Research Council of the National Academies (The National Academies Press, Washington, 2007). The online version of this reference can be found here: http://www.nap.edu/openbook.php?record_id=11954

R.R. Vondrak, Creation of an artificial lunar atmosphere. Nature **248**, 657–658 (1974)

The Neutral Mass Spectrometer on the Lunar Atmosphere and Dust Environment Explorer Mission

Paul R. Mahaffy · R. Richard Hodges · Mehdi Benna · Todd King · Robert Arvey · Michael Barciniak · Mirl Bendt · Daniel Carigan · Therese Errigo · Daniel N. Harpold · Vincent Holmes · Christopher S. Johnson · James Kellogg · Patrick Kimvilakani · Matthew Lefavor · Jerome Hengemihle · Ferzan Jaeger · Eric Lyness · John Maurer · Daniel Nguyen · Thomas J. Nolan · Felix Noreiga · Marvin Noriega · Kiran Patel · Benito Prats · Omar Quinones · Eric Raaen · Florence Tan · Edwin Weidner · Michael Woronowicz · Cynthia Gundersen · Steven Battel · Bruce P. Block · Ken Arnett · Ryan Miller · Curt Cooper · Charles Edmonson

Abstract The Neutral Mass Spectrometer (NMS) of the Lunar Atmosphere and Dust Environment Explorer (LADEE) Mission is designed to measure the composition and variability of the tenuous lunar atmosphere. The NMS complements two other instruments on the LADEE spacecraft designed to secure spectroscopic measurements of lunar composition and in situ measurement of lunar dust over the course of a 100-day mission in order to sample multiple lunation periods. The NMS utilizes a dual ion source designed to measure both surface reactive and inert species and a quadrupole analyzer. The NMS is expected to secure time resolved measurements of helium and argon and determine abundance or upper limits for many other species either sputtered or thermally evolved from the lunar surface.

Keywords Moon, lunar volatiles · Mass spectrometry · Noble gases · Argon · Helium

P.R. Mahaffy (✉) · M. Benna · T. King · R. Arvey · M. Barciniak · M. Bendt · D. Carigan · T. Errigo ·
D.N. Harpold · V. Holmes · C.S. Johnson · J. Kellogg · P. Kimvilakani · M. Lefavor · J. Hengemihle ·
F. Jaeger · E. Lyness · J. Maurer · D. Nguyen · T.J. Nolan · F. Noreiga · M. Noriega · K. Patel · B. Prats ·
O. Quinones · E. Raaen · F. Tan · E. Weidner · M. Woronowicz
NASA Goddard Space Flight Center, 8800 Greenbelt Rd., Greenbelt, MD 20771, USA
e-mail: Paul.R.Mahaffy@nasa.gov

R. Richard Hodges
Laboratory for Atmospheric and Space Physics, University of Colorado, Boulder, CO 80303, USA

C. Gundersen
AMU Engineering, Miami, FL 33156, USA

S. Battel
Battel Engineering, Scottsdale, AZ 85253, USA

B.P. Block · K. Arnett · R. Miller · C. Cooper · C. Edmonson
Space Physics Research Laboratory, University of Michigan, Ann Arbor, MI 48109, USA

1 Scientific Objectives of the LADEE NMS

1.1 Lunar Atmosphere

The atmosphere of the moon is so tenuous that collisional interactions between free particles are entirely negligible. Each atom travels through the atmosphere in a ballistic trajectory that begins and usually ends on the lunar surface. The exceptions are particles that are ionized by solar photons, and those that leave the surface with speeds greater than the escape speed, which is nominally 2.38 km s^{-1} but vary with the acceleration due to radiation pressure, and with the proximity of the trajectory to the L1 or L2 Lagrangian equilibrium point.

As envisioned pre-Apollo by Hodges and Johnson (1968), there are 2 categories of atoms, those that "condense" on the cold nighttime surface of the moon, and those that do not. Gases that condense at night ride on the rotating lunar surface, as on a conveyor belt, and evaporate as the surface temperature increases following sunrise, forming a pocket of gas over the sunrise terminator. Those that do not condense tend to obey the law of exospheric equilibrium (1), which to first order is

$$nT^{5/2} \approx \text{constant} \tag{1}$$

where n is surface concentration and T is temperature.

With the knowledge gained from Apollo returned samples, the theory of the surface interaction process has evolved into something more complicated than condensation and evaporation. Upon striking the lunar surface, an atom finds itself in a fairy-castle-like structure of loosely packed, micron-scale grains, wherein the grain surface area is several thousands of cm^2 per gram. The statistics of inter-grain vertical transport is similar to a 1-dimensional random walk, that is, the mean number of encounters is about 2, but the average is infinite (Hodges 1980). Each encounter with a grain can end in 2 ways. One is elastic scattering through phonon transfer. The other is thermal accommodation, a 2-step process of adsorption, followed by desorption with a residence time determined by the temperature dependence of the Arrhenius equation. The adsorption/desorption process is analogous to condensation/evaporation in the sense that vapor pressure is derived from the former.

Elastic scatter tends to create a Maxwellian distribution of velocities, while desorbing atoms have a higher energy Knudsen (or Maxwell-Boltzman-flux) distribution. The result of multiple grain encounters is a hybrid velocity distribution and a non-barometric altitude profile.

1.2 Ground Truth

The Apollo 17 mass spectrometer established the presence of helium and argon-40 in the nighttime lunar atmosphere. Owing to operational constraints, there are no daytime data.

Black curves in Fig. 1 show the nighttime part of the diurnal variation helium at the Apollo 17 site during the first 10 lunations of 1973 (Hodges and Hoffman 1974). Overlays in red are Monte Carlo simulations derived with the aid of the LExS (Lunar Atmosphere Simulation) tool kit (Hodges 2011). On average, the nighttime maximum of helium approximates the $T^{5/2}$ law of exospheric equilibrium. Fluctuations of the black curves with respect to the red ones reflect variations in one of the sources of helium, which are solar wind α-particles and radiogenic He escaping from the lunar interior.

The presence of ^{40}Ar in the lunar atmosphere was foretold by Apollo 11 soils that had apparent K/Ar ages that are older than the solar system. Yaniv et al. (1972) gave a prescient

Fig. 1 Helium data from the
Apollo 17 mass spectrometer
(*black*) and simulated data (*red*).
Day of year 1973 is annotated on
abscissa
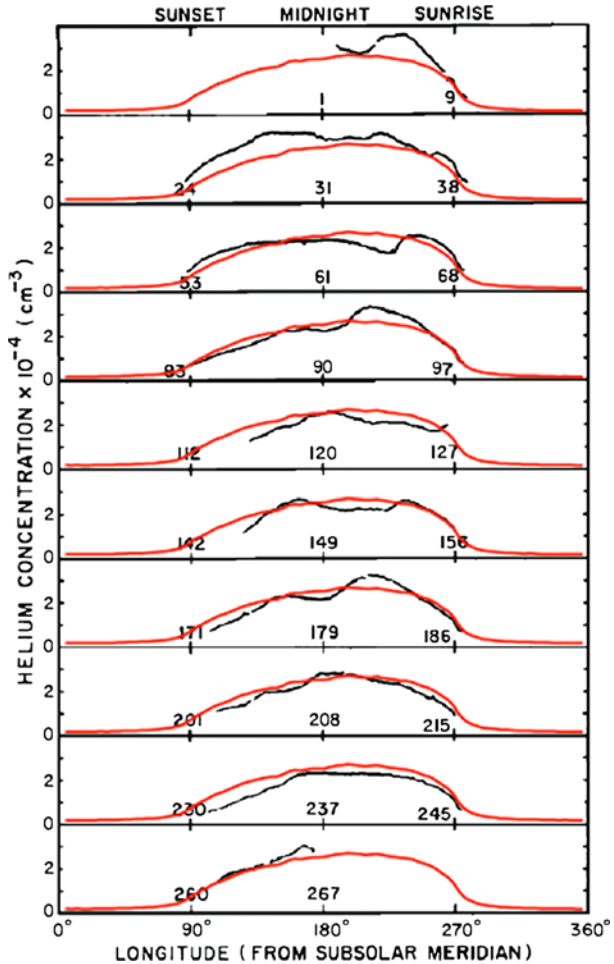
explanation of the parentless argon as re-trapped atmospheric ions. In other words, the atmosphere of the moon includes argon that is supplied by radiogenesis in the interior of the moon.

Thus it was not surprising that ^{40}Ar was detected by the Apollo 17 mass spectrometer. However, the diurnal behavior shown for 2 lunations in Fig. 2 (Hodges and Hoffman 1974) was unexpected. In the distinctly non-equilibrium nighttime pattern, the post-sunset decay of argon is easily associated with adsorption as the surface cools, and the pre-sunrise build-up suggests rapid desorption at sunrise. This is essentially the prediction of Hodges and Johnson (1968) for a condensable gas, like water vapor. For argon, this behavior requires pristine grain surfaces that have not been exposed to enough water vapor to form a monolayer (Hodges 2001).

A second noteworthy feature of Fig. 2 is the difference in the amplitudes of the diurnal profiles, which implies that during the March to July interval, escape exceeded supply, creating a noticeable decrease in the total abundance of argon on the moon. What is clear is that the release of radiogenic gases from the interior of the moon is episodic; the Apollo 17 data
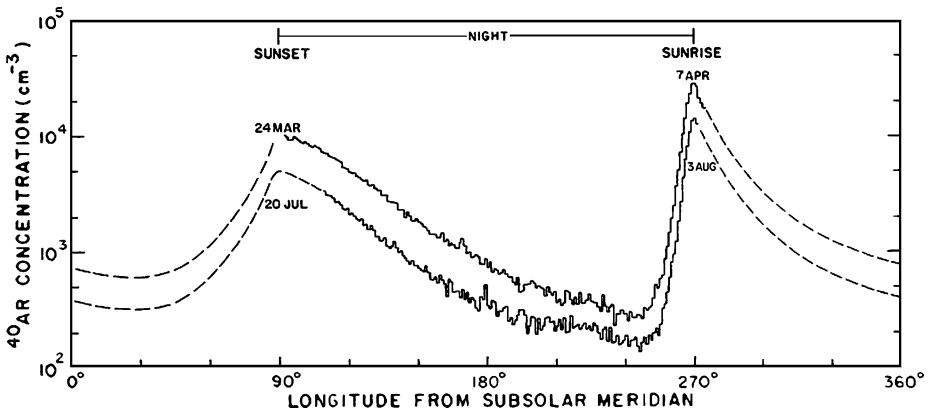
Fig. 2 Apollo 17 measurements of ^{40}Ar from 2 lunations of 1973

suggest a correlation with tele-seismic events. It follows that argon may disappear from the lunar atmosphere during prolonged periods of low seismic activity.

1.3 Expectations of the LADEE NMS

Simulations of expected NMS orbital data, constructed with the aid of LExS and using instrument sensitivities described in this manuscript, are shown in Fig. 3 for orbits with periapses at sunrise. In addition to helium and argon whose densities are predicted from previous observations (e.g. Hodges et al. 1974; Stern 1999), the graph includes several species that might be supplied by thermalized solar wind. Since these species have not been observed, these simulations are included primarily to illustrate the LExS predictions of their variation along a typical LADEE orbit. The abscissa is time from periapsis and the sunrise terminator. The scale of ordinates, counts per second, is chosen to emphasize the degree of statistical uncertainty in the expected data if these species are detected and the vulnerability of the data to the background artifacts. Oxygen is presumed to combine on internal NMS surfaces to form O_2 although the actual behavior of atomic oxygen in the closed source in this low density environment cannot be predicted from the available data.

Wide segments of the curves of Fig. 3 cover periods of operation of the NMS, while thin line extensions are what could be expected if sufficient power were available to operate throughout an orbit.

1.4 Reduction of Orbital Data

To make sense of the orbital data it is necessary to project concentrations measured at various satellite altitudes to a reference level, the logical candidate being the USGS reference geoid radius of $r_0 = 1737.4$ km. This projection will be derived from the altitude profile

$$\ln \frac{n}{n_0} = \sum_i A_i \{(r/r_0)^i - 1\} \tag{2}$$

where the $i = 1$ term is hydrostatic equilibrium that would arise if all atoms were to accommodate and leave the surface with a Knudsen distribution of velocities. Higher order terms are needed to account for the Maxwellian component as well as the mix of gas temperatures in the down-coming fraction due to lateral gradients of surface temperature (Hodges 1972).

Fig. 3 Simulated LADEE NMS data for 3 orbits with periapsis at sunrise. *Bold lines* cover power-limited measurement periods; *light extensions* what would be measured if additional power were available
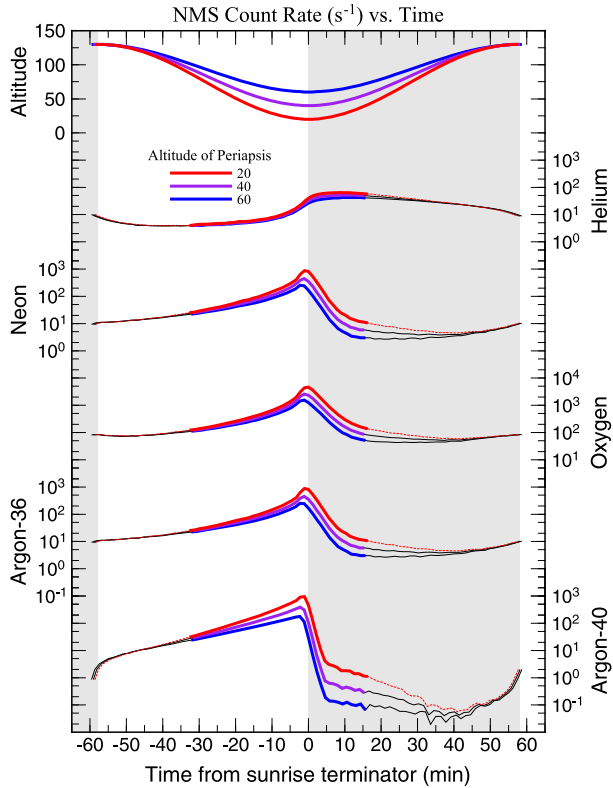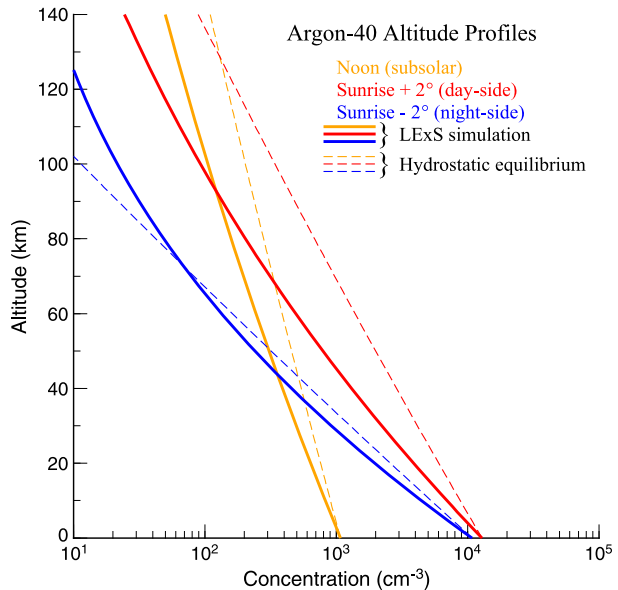

Figure 4 illustrates the differences between altitude profiles for hydrostatic equilibrium (dashed lines) and LExS simulations that account for lateral flow and the un-accommodated fraction of atoms leaving the surface. Note that at high altitudes the slope of the simulated dayside profile for sunrise +2° approaches the slope of hydrostatic equilibrium. However, just 2° on the night side of the sunrise terminator, where upward going atoms are cold while the day to night flux is relatively hot, the latter obviously dominates at high altitude.

A fortuitous aspect of the LADEE mission is that frequent orbit maintenance maneuvers are required to keep periapsis above the surface. Contamination modeling demonstrated that the flux of gas from the LADEE thrusters located well away from the NMS during these maneuvers into the NMS would be negligible. NMS measurements of ambient gas concentrations collected immediately before and after each OMM will provide local scale heights over a substantial range of altitudes. At the end of the mission, the OMM data set will be used to create normalized altitude profiles that, in turn, will facilitate the reduction of orbital data to the geoid radius. In addition, these data will be invaluable in the synthesis of accommodation coefficients and energies of activation in the lunar regolith

1.5 The LADEE Mission Duration and Orbit

The LADEE spacecraft bus is a modular design utilizing a carbon composite structure that could be adapted for use with a variety of launch vehicles. In this case the spacecraft with its three instruments and a laser communications technology demonstration unit are adapted to a Minotaur V launch vehicle launched from the Wallops Flight Facility for a nominal 100

Fig. 4 Simulated vertical profiles of ^{40}Ar at noon and sunrise at +2° longitude. *Dashed lines* are classical hydrostatic equilibrium profiles included to elucidate non-thermal properties

Argon-40 Altitude Profiles
Noon (subsolar)
Sunrise + 2° (day-side)
Sunrise - 2° (night-side)
} LExS simulation
} Hydrostatic equilibrium

day science mission after a commissioning period of 30 days. The commissioning phase in a lunar elliptical orbit of approximately 250—275 km also allows the tests of the optical communications module. For the science orbit an elliptical orbit will also be utilized to conserve propulsion but with periapsis to 50 km and below and an orbital time of typically less than 2 hours. With limited battery capacity the measurement time during orbits will typically be shared between the NMS, the Lunar Dust Experiment (LDEX), and the Ultraviolet and Visible Light Spectrometer (UVS) but not operating all three instruments concurrently.

2 Instrument Description

2.1 Introduction and Heritage

Many elements of the Neutral Mass Spectrometer have a heritage in mass spectrometers previously developed for planetary or Earth orbiting satellites. The quadrupole mass analyzer and detector systems are similar to those developed for Venus (Niemann et al. 1980), the upper atmosphere of Mars (Niemann et al. 1998), the deep atmosphere of Jupiter (Niemann et al. 1992), and the atmosphere of Titan (Niemann et al. 1997). In all of these experiments the gas sampling and pumping systems, if required, were specifically designed for the target environments. Direct heritage for the NMS design came from the Ion and Neutral Mass Spectrometer (INMS) on the Cassini Orbiter (Kasprzak et al. 1996) and the Comet Nucleus Tour (CONTOUR) (Veverka et al. 1995) Neutral Gas and Ion Mass Spectrometer (CONTOUR-NGIMS) which were modifications of the NGIMS instrument design for the Comet Rendezvous Flyby Mission (CRAF) that was under development when that mission was canceled. In fact, the approach taken for the LADEE-NMS was to utilize the engineering unit sensor from the CONTOUR-NGIMS and to develop a new set of electronics. The CONTOUR NGIMS and the Cassini INMS (Kasprzak et al. 1996; Waite et al. 2004) experiments utilized an electrostatic 90 degrees deflector (Mahaffy 1990) designed to multiplex two separate ion sources to the quadrupole analyzer (Fig. 5).

**Fig. 5** A schematic view of the gas and ion path in the NMS
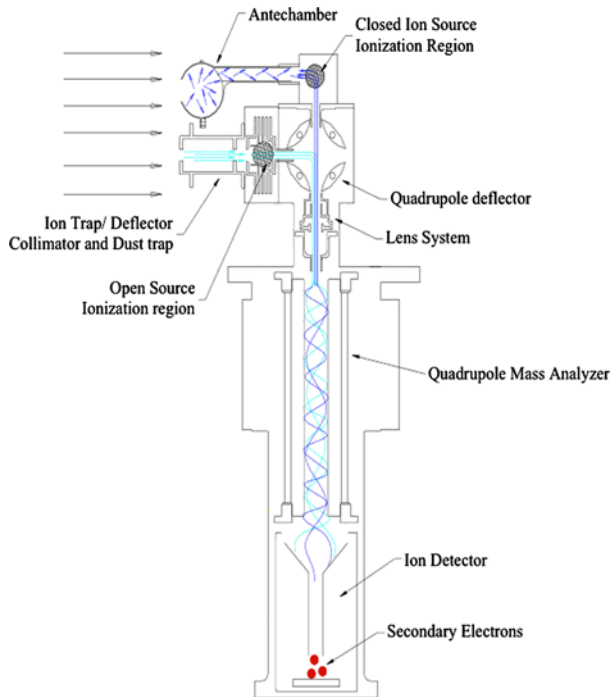
Significant improvements to the INMS design, however, were implemented in both the CONTOUR-NGIMS and the NMS designs to optimize the measurement for sensitivity. In order to allow the measurement of trace species in the short integration time available in a comet nucleus flyby and in the low-density exosphere of the moon, the sensitivity of the CONTOUR-NGIMS and the LADEE-NMS were extended considerably beyond that of any mass spectrometer previously developed for planetary applications with nominal sensitivity for ^{40}Ar of 2.3×10^{-2} (counts/sec)/(part/cc). In addition, the CONTOUR NGIMS was designed with mass dependent adjustment of the quadrupole bias and electrode focusing voltages for the considerably higher comet nucleus flyby velocities in the cometary coma nuclei encounters compared to the Cassini Orbiter flyby velocity at Titan. Each of the heritage mass spectrometers could operate at unit mass resolution over the full spectral range (2–99 Da in the case of the Cassini-INMS and 2–294 Da in the case of the CONTOUR-NGIMS). Figures 6, 7, and 8 respectively show the NMS instrument during and after integration, the ion source and mass analyzer, and the sensor housing and detector assembly.

The mass spectrometer schematic (Fig. 5) shows the sensor including the ion source assembly with the quadrupole deflector for multiplexing ions from the two sources into the mass analyzer, the sensor housing, the quadrupole rod assembly, and the dual detector system. Several of the instrument performance specifications are given in Table 1. The block diagram (Fig. 9) shows the various electronic subsystems.

2.2 Neutral Gas and Ion Sampling

Closed Ion Source The classic design of a closed ion source (Spencer and Carignan 1988) for upper atmosphere space research consists of a small aperture in a spherical antechamber.
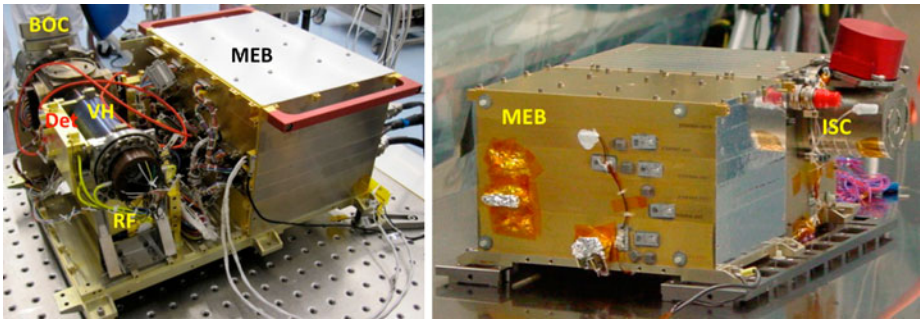
Fig. 6 The *left panel* shows the main electronics box (MEB), the break off cap (BOC), the vacuum housing (VH), the radio frequency (RF) electronics, and the detector (Det) electronics. In the *right panel* view the covers and *red tag* items are also shown as is the ion source cover (ISC)

Fig. 7 The ion source assembly is shown *on the top left* with the open source (OS), closed source (CS), and quadrupole deflector (QD). The quadrupole rod assembly is shown *on the right*
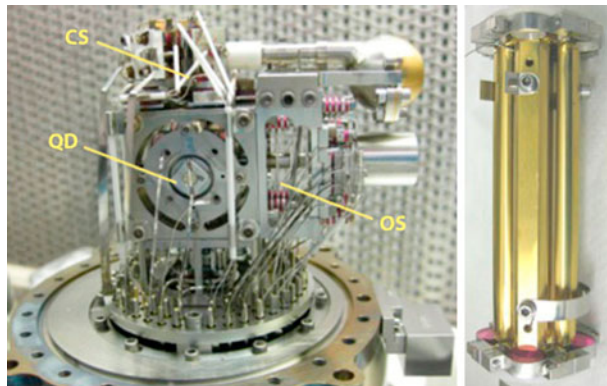
Fig. 8 The mass spectrometer housing is shown in the *left panel* and the detector assembly *on the right*. The outside diameter of the detector housing is 5.08 cm. The larger pins on the welded electrical feedthrough assembly are for the RF voltages applied to the quadrupole rods. The pinch-off tube is seen *to the left* of the feedthrough assembly. The dual detector assembly show *at right* is mounted on a flange that utilizes a gold plated Inconel "c" seal to achieve ultra-high-vacuum. The NMS specifications are shown in Table 1
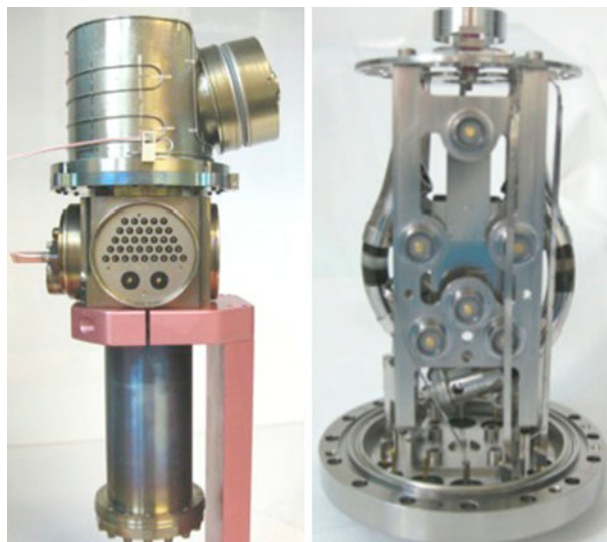
Table 1 NMS specifications

Neutral gas sampling	(1) open source/molecular beaming (2) closed source
Positive ion sampling	Thermal and suprathermal through open source
Ion source	Electron beam ionization
Electron energy	75 eV
Ion source sensitivity	$\sim 2 \times 10^{-2}$ counts/sec/part/cc for argon
Mass range	2–150 Da
Detector system	Detector pulse counting electron multipliers
Scan modes	(1) programmed mass mode (2) survey—scan full range in 1 amu or 0.1 amu steps
Deployment mechanism	Metal ceramic breakoff cap, pyrotechnically activated
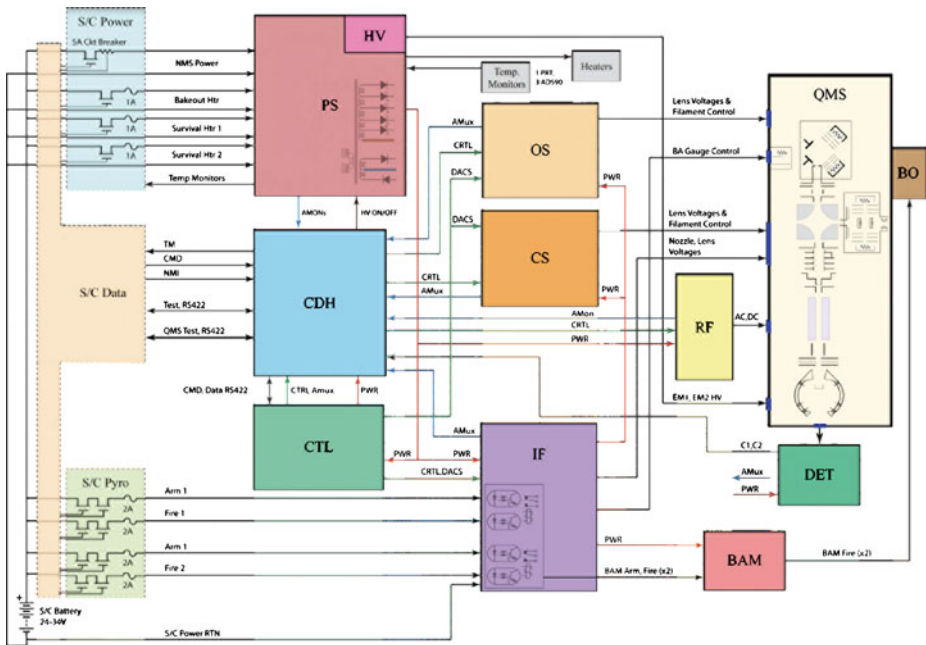
Fig. 9 The NMS electrical block diagram

Gas flows into the source through this aperture and most of the gas eventually leaves through the same aperture after thermalization with the walls of the source.

A portion of the gas leaks out through a relatively small ion exit aperture, and another small portion is ionized and accelerated out of the source through the electrostatic deflector and into the entrance lens focusing system of the mass analyzer. The vent orthogonal to the open source axis that was included in the Cassini INMS design was closed in the NMS design to better quantify the relationship of the density in the ionization region to the ambient density. In the NMS design the entire sensor volume acts as a closed source. The density in a closed source of this geometry for species i can be shown (Wurz et al. 2007) from the relevant gas kinetic equations to be:

$$n_{s,i} = n_{a,i}(T_{a,i}/T_{s,i})^{1/2}\left(\exp(-S_i^2) + \pi^{1/2}S_i\left[1 + \mathrm{erf}(S_i)\right]\right)$$

$$\text{with } S_i = V \cos(\alpha)/c_i \text{ and } c_i = (2kT_{a,i}/m_i)^{1/2}$$

where n = density and T = temperature, with the subscripts a and s designating the ambient and source values respectively for species i. V is the apparent bulk speed of the atmosphere in the spacecraft reference frame, α = the angle between the normal to the orifice and the spacecraft velocity vector, c_i = the most probable speed of the ambient gas particles, and k = Boltzmann's constant. The classic closed source configuration will typically accept gas from nearly a 2π steradian field of view and will provide nearly a 50 % measurement duty cycle on a spinning spacecraft. The LADEE spacecraft is 3-axis stabilized during the NMS measurement periods.

Open Ion Source The open ion source is designed to measure or lower the upper limit on species such as OH with a high upper limit of $\sim 1 \times 10^7$ particles/cc that would be destroyed or transformed by collisions in the closed ion source. The NMS can also search for metal atoms or their oxides with this source.

In the open ion source, collimating apertures form a neutral beam of particles that pass through a crossed electron beam generated by focusing electrons emitted from a hot, 97 % tungsten, 3 % rhenium, 0.005″, 6-coil filament. A fraction of these particles are ionized and transported through the electrostatic deflector to the quadrupole analyzer. Ambient ions are swept out of the inlet path by a set of deflection electrodes before they reach the ionization region.

The electrostatic deflector is an energy dispersive device. The kinetic energy $(0.5mv^2)$ of a neutral exospheric gas particle with mass m and velocity v in the spacecraft frame of reference is established by the spacecraft velocity combined with the velocity of the lunar particle determined by where it is on its ballistic trajectory after release from the lunar surface. The bandpass of the deflector is approximately 25 eV with the voltages selected for the NMS operation. The bias on the grid at the exit to the ionization region is set slightly positive to discriminate against the gas that has thermalized in the mass spectrometer. The efficiency of the open source is expected to be similar to that of the closed source with an identical electron gun design, but the exact relationship of the sensitivity of the two sources will only be established in space by comparison of the signals from a relatively abundant gas such as He or Ar from the open and closed sources since the voltage settings for nominal open source operation in lunar orbit are optimized through simulations to discriminate against open source thermalized gas and cannot be further verified in the laboratory without an atomic beam source.

2.3 Quadrupole Mass Analyzer and Detector

Quadrupole Mass Filter The mass analyzer consists of four quadrupole rods precisely fabricated and assembled into a rigid parallel assembly to which a combination of radio frequency (RF) and static (DC) voltages are applied to achieve mass separation. The voltages $(V_{dc} + V_{ac} \cos(\omega t))$ and $-(V_{dc} + V_{ac} \cos(\omega t))$, where ω is the frequency of V_{ac}, are applied to opposite rod pairs resulting in a two-dimensional quadrupole field of the form

$$\phi(x, y) = \left(V_{dc} + V_{ac} \cos(\omega t)\right)\left(x^2 - y^2\right)/R_o^2$$

where R_o is the distance from the z (symmetry) axis to the nearest rod surface, and x and y are the axes crossing both the z axis and nearest point of the adjacent rods. Two fixed frequencies were used over the 2–150 Da mass range of NMS: 3.0 MHz for the mass range 2 to 20.5 Da and 1.4 MHz for the range 20.5 to 150.5 Da. Small amplitude changes in

the RF are made under software control to compensate for any temperature or frequency drifts. These corrections keep the analyzer tuning essentially constant over the instrument operating temperature range of $-20\,°C$ to $+40\,°C$.

The V_{dc} has an additional bias voltage, V_{bias}, added to it that is a function of the mass. This voltage is adjusted during tuning to allow ions to spend sufficient time (cycles) in the mass resolving RF field thus reducing the mass peak width and hence increasing the mass resolution.

Detector Assembly   The NMS detector assembly consists of a system of ion focusing lenses and two redundant off-axis continuous channel electron multipliers. The ion focusing lens system consists of four lenses positioned between the exit of the quadrupole analyzer and the entrance of the multipliers. A voltage ranging from -200 V to 550 V is applied to each lens to focus the ions exiting the analyzer into the detectors.

The model 4870-channeltron electron multipliers were purchased from Photonis and were assembled in house. Finite element analysis was employed in the design of the detector housing to insure that these glass devices would not be damaged during the considerable vibrations incurred during the LADEE launch and the subsequent solid rocket motor burn. The NMS multipliers begin to saturate at several million counts per second with an average gain of 6×10^7, and a background noise level of ~ 8 counts per minute. The operating voltage is between -2400 V and -3000 V. The multipliers are positioned off axis of the quadrupole to avoid detecting spurious photons and neutrals. The two multipliers are assembled facing each other within their housing, providing a redundant system.

2.4 Electrical Design

Spacecraft Interface   The NMS Main Power is supplied via a single-string, spacecraft-switched, 5 A resettable circuit breaker operating at the nominal spacecraft bus voltage of 28 VDC with an operating range of 24 VDC to 34 VDC (Fig. 9). NMS Heater Power is also supplied by the spacecraft power bus via single-string, spacecraft-switched, 1A resettable circuit breakers. One switch is dedicated to the Bakeout Heater and two switches are dedicated to the Main Electronics Box (MEB) and RF Survival Heaters. Any, or all, buses may be turned on in any order and the maximum possible power from all busses is approximately 45 W. Power usage during experiment operation is a function of the commanded instrument mode with the power sequencing on 30 ms intervals.

The spacecraft also provides four switches for commanding the two bellow actuators in the break-off cap. These switches serve as the Arm and Fire commands for each pyro and are electrically isolated by opto-couplers. As well, the spacecraft interface includes monitoring capability for one Platinum Resistive Thermometer (PRT) temperature sensor and three AD590 temperature sensors located on the sensor and on the electronics. The spacecraft Data Interface consists of a single string, high speed (2 Mb/s) along with a discrete interface (NMI) used for interface reset if needed.

NMS Module Overview   Most of the NMS instrument electronics are integrated into the MEB as 6 slices or modules. The list below is in the order they are incorporated as slices into the MEB.

- *PS/HV*—Power Supply/High Voltage
- *CDH*—Command Data Handling
- *CTL*—Control
- *IF*—Ion Focus

- *CS*—Closed Source
- *OS*—Open Source

The two stand-alone modules are the *RF* (Radio Frequency) and DET (Detector) which are both attached to the Quadrupole Mass Sensor (QMS) housing. With exception of the survival and bakeout heaters, all of the modules receive their power from the common NMS power supply.

Power Supply/High Voltage (PS/HV) Module   PS/HV Module utilizes a two stage design that provides good line and load regulation without post-regulators and provides primary and secondary isolation. A Pulse Width Modulator (PWM) pre-regulator operating at 50 KHz feeds a 75 W DC-DC converter (slaved to the 50 KHz oscillator) providing six independent ground-isolated secondaries (DC and AC outputs). Load regulation is better than 5 % over expected load and temperature conditions and the power supply operates within specification over an input voltage range of 22 VDC to 36 VDC.

Other features include filter pre-charging and soft-start control to limit inrush current, EMI filtering with a common-mode Balun, under-voltage detection, primary side power monitoring, input power limiting, and auto restart from a fault condition. Two high voltage (HV) supplies are integrated into the module providing two DAC programmable outputs up to -3500 VDC for the Channel Electron Multipliers (CEMs).

Command and Data Handling (CDH) Module   The NMS Command and Data Handling module (CDH) is based on a radiation hardened, 32-bit Coldfire microprocessor. The module contains 2 megabytes of rad-hard static RAM (SRAM) memory, 32 kilobytes of PROM and 1 megabyte of Electrically Erasable PROM (EEPROM). The PROM memory contains a non-changeable bootloader which allows NMS to update the main flight software application stored in the EEPROM memory. In addition, tables and scripts are uploaded into the EEPROM as required. The SRAM memory is used to run the flight software, which controls operation of the NMS instrument, and for temporary data storage.

In addition to providing the computer controller for NMS, the CDH module also contains two 16-bit analog to digital converters (ADC) for sampling various housekeeping parameters within the system, such as voltages, currents and temperatures. A master AMUX is used to multiplex 152 channels of analog data to these two ADCs. Fifteen digital to analog converters (DACs) are provided for controlling the NMS filaments and the RF subsystem. Two additional DACs are employed for setting the threshold for pulse counters. The CDH module communicates with the LADEE spacecraft via a synchronous 422 serial command and telemetry bus along with a discrete interface (NMI). All data collected by NMS is packetized by the flight software and sent to the LADEE spacecraft via this interface. All NMS housekeeping data will be archived with the science data to make obvious any changes in instrument modes during data acquisition.

Control Electronics (CTL) Module   The Control module (CTL) provides twenty-eight 8-bit, thirty-eight 12-bit and two 16-bit digital to analog converters. These devices are used to control the Open Source (OS), Closed Source (CS) and Ion Focus (IF) electronics that in turn control the higher voltages required by the QMS. All of the DACs are controlled by the flight software running on the CDH and are synchronized with the operations of the CDH hardware. Additionally, the CTL module provides local low-voltage regulation for the CTL, CDH and DET modules.

Ion Focus (IF) Module   The IF module contains electronics to operate the Bayard-Alpert (BA) gauge pressure sensor and provides DAC controlled electrode bias functions for the Quadrupole Mass Spectrometer. It also provides spacecraft controlled power switching to fire the redundant bellows actuators.

The BA gauge filament is controlled by a single voltage loop under DAC control and does not have direct emission regulation. The BA gauge is normally used to check the internal sensor pressure before turning on the QMS filament. As part of the BA measurement circuit, the filament is biased at +20 VDC using a virtual ground configuration to allow a direct emission current measurement, up to 1 mA. +160 VDC bias for the Grid and an electrometer capability are also provided in order to make the pressure measurement.

The IF module also provides DC voltage supplies for the IF, CS, and OS high voltage amplifiers. Nineteen DAC controlled amplifiers on the IF provide the biases required by the QMS for proper focusing, including eight −900 VDC and one +900 VDC outputs. The error amplifier drive for each electrode is monitored in the housekeeping data such that a short to structure or to another electrode can be determined from the telemetry.

Two independent Pyro firing circuits are commanded by spacecraft controlled power switches through opto-isolators. The ARM command enables the circuit by switching a mechanical relay to remove a short across the pyro leads. The FIRE command switches on continuous current to the pyro sufficient to ensure its firing. The current source is a dedicated winding on the PS/HV main transformer and is capable of providing 5 V at 5 A continuously. In order to fire a pyro, the NMS Main Power Switch must be switched on, the ARM command must be issued then the FIRE command must be sent.

Open Source and Closed Source (OS/CS) Modules   The OS/CS consists of two modules dedicated to filament emission control and electrode bias functions for the QMS Open and Closed Ion Sources. Each ion source contains two filaments that are not operated simultaneously. A linear pre-regulator with an independent control loop is employed to minimize the effects of line and load variations on the emission current. Two DACs are utilized for ion source operation; one to control filament voltage and the second to set emission current. This allows the flight software to soft start the filament by creeping up the filament voltage until the stable emission operating point is reached. The emission control level is programmable from 20 uA to 400 uA with control normally set to either 50 or 200 uA. A unique feature of the emission control loop design is that the filament floats at −70 VDC using a virtual ground configuration to allow direct measurement of the emission current. A latching relay sets the bias voltage on the active filament with the inactive filament referenced to ground.

Each module provides 18 DAC settable bias voltages ranging from −300 volts to +300 volts for the QMS focusing electrodes in order properly focus the electrons and ions. All DAC settings are recorded in telemetry. The electrode voltages are regulated to 2 % absolute and 0.5 % relative accuracy.

RF Electronics   The NMS RF Electronic Subsystem primary function is to provide two selectable and stable AC frequencies to the Quadrupole Rods of the NMS instrument. The amplitude of the DC and RF voltages provided to the QMS rods is controlled by the analog output of 16 bit DACs located in the CDH. The RF tuning requires an unusually high accuracy and stability. For example, a 1/10th Da shift can result from an amplitude change of 0.03 % or a frequency change of 0.015 %. This sensitivity requires tight requirements for the stability of these open loop analog circuits over the wide temperatures that this circuit is required to operate under. A tank circuit Q above 120 is required to achieve low power (8 W) and high voltage (1200 Vp-p), and the necessary frequency stability.

Fig. 10 Elements of the flight software. The SRAM image occupies approximately 150 KB
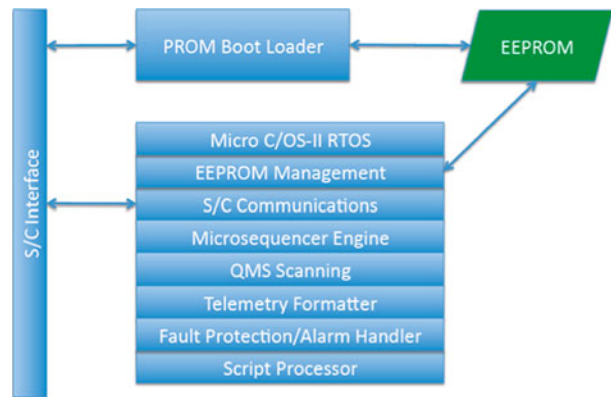
The frequencies are defined as High Frequency (HF) 3.0 MHz ($+/-0.3$ MHz) corresponding to 2–20.5 Da and Low Frequency (LF) 1.4 MHz ($+/-0.1$ MHz) corresponding to 20.5–150.5 Da. The dynamic range is linear from 50 Vp-p to 700 Vp-p for HF and 50 Vp-p to 1200 Vp-p for LF. The AC waveform stability is such that mass peaks are stable to $+/-2$ % over a temperature range of -20 °C to $+45$ °C.

The two ROD+ and ROD− outputs are 180 degrees out of phase and have controllable and inverted DC biases of up to $+/-150$ VDC. There is also a controllable DC offset Quad Bias voltage of $+11$ VDC to -10 VDC that float both outputs. Total RF power required is under 8 W peak and 4 W average. The time required to reach a nominal mass value (within $+$ or -0.1 AMU) in the same frequency range is less than 3 milliseconds and in a different frequency range is well under 20 milliseconds.

DET Electronics   The NMS detection system consists of redundant Photonis Channel Electron Multipliers. The DET electronics provides independent channels for each multiplier and leverages a custom low power, high speed Pulse Amplifier hybrid. The Pulse Amplifier is capable of providing roughly 30–33 dB of gain at about 100 MHz and the completed assembly will consume <500 mW over worst-case flight conditions at End Of Life. The amplified outputs are passed via coaxial cable to the CDH for discrimination and counting.

2.5 Flight Software and Scan Sequences

The elements of the flight software used by the NMS Coldfire processer are illustrated in Fig. 10. The software can be loaded into SRAM either from the spacecraft or from the NMS EEPROM. The flight software is fully uploadable and modifiable safely in flight.

PROM Boot Loader   When power is applied to the NMS the boot loader gains control. If no commands are received from the spacecraft interface within 30 seconds it begins to load the operational image from EEPROM. After this load is finished control is transferred to its entry point. If a command is received within the first 30-second interval after power up the boot loader waits for further commands. The boot loader has a command set that enables it to maintain the EEPROM file system by creating, modifying, copying, moving, or deleting files. The boot loader can also erase and reformat the EEPROM. It can also mark bad blocks and select among operational image files for booting. After the boot loader carries out the chip-level and board-level initialization it enters a loop and listens for commands with the only exit from this loop being via a program load operation. The boot loader operates in safe mode with no operating system or interrupts.

EEPROM File System   The parameter tables, script files, and other data as well as the operational software image are stored in this non-volatile memory. The EEPROM file system was taken entirely from the flat file system designed for the SAM suite. Redundant directories located at the high and low end of the memories employ automatic fail-over and are protected by checksums. Both the boot loader and the operational image can access the EEPROM file system. Each file created in EEPROM is assigned a unique ID number, an assignable type code, and a file checksum computed when the file is written. These files occupy contiguous blocks of memory and the checksum is stored in the file's directory entry. Files cannot be used unless the checksum in the directory matches that computed from the file. The message log telemetry includes the ID, checksum, type, and name for each file.

Script Processor   This command system was also taken entirely from the SAM design and consists of a BASIC interpreter that employs the full set of language constructs, such as FOR-NEXT, DO-LOOP, IF-ELSE-ENDIF, and nested subroutine calls. It also employs unique built-in commands to operate the instrument in all its various modes. Functions or subroutines can be defined that contain multiple lines of BASIC script that can take arguments or parameters and may return a value. These functions called by name are the building blocks of the NMS experimental sequences that will typically operate for a full or a partial lunar orbit. The script processor developed for the Mars Science Laboratory SAM experiment on which the NMS script processor is based has been more fully described (Mahaffy et al. 2012).

Scan Sequences   The flight software implements several methods to control the QMS scanning sequence, which are invoked through script commands as originally developed for SAM. For NMS, a new method was implemented to allow precise control over the timing of the mass scans, so measurements can be tailored to the anticipated conditions at every orbital position, thereby increasing spatial resolution and signal strength for rare species.

2.6 Mechanical Configuration

Design Process   The design software tool ProE was used throughout this development for all mechanical elements of NMS. Prior to fabrication, stress and modal analysis was performed on the housing structure assembly. The finite element model was created in the finite element application FEMAP and processed in Nastran. The parts of structure analyzed were the housing base, the external and internal structural panels, the sensor support bracket, and various fasteners and mounting hardware. The outcome of this analysis was that the fundamental frequency was found to exhibit positive safety margins for maximum stress in the assembly and for all fastening hardware in tension and shear.

Pyrotechnic Breakoff   The pyrotechnic operation that exposes the ion source system to the space environment is scheduled during the commissioning phase of the mission. The NMS electronics provides the high current actuation pulse for this pyrotechnic device. Since the sensor was baked to nearly 300 °C several times, the breakoff cap is designed to be ultra-high-vacuum compatible and consists of an external wedge that upon actuation by a pyrotechnic device, breaks a metal to ceramic to metal seal. Spring loading on the breakoff cap sends this cover away from the spacecraft and the instrument after actuation. The apertures exposed to space after the pyrotechnic actuation are those of the closed and open source that are illustrated in Fig. 5.

2.7 Thermal Design

The thermal design for the NMS was challenged by the wide variations in solar thermal loads of more than 1000 W/m^2 on the sunward side and just a few W/m^2 at night. The design goal for the resulting NMS temperature transients was to keep them at or below 30 °C although the requirements for operation for the MEB were between -20 °C and $+40$ °C with higher limits for the RF electronics ($+55$ °C) and the mass spectrometer sensor ($+65$ °C). The ion source cover was equipped with decontamination heaters designed to bring this part of the sensor housing to $+180$ °C if desired during the orbital mission. The thermal margin philosophy at GSFC for passive thermal designs for protoflight unit testing is to operate 10 °C above and below the hot and cold allowable operating temperatures respectively. The NMS thermal control elements included 5 mil silver Teflon on the external surfaces of the MEB, an aluminum heat strap to further sink the RF electronics located directly under the sensor housing, multi-layer insulation consisting of germanium black Kapton on its outer layer, and Kapton foil heaters. The 50 surfaces/200 node Thermal Desktop model used for analysis duplicated the LADEE orbit around the moon for each of the NMS measurement configurations. For example, in the RAM sampling measurement mode the NMS would be fully exposed to the sun and then fully in the shade at different points in its ~2 hour orbit. During the science part of the mission we expect the NMS MEB temperatures to be safely ~5 °C or more away from the allowable hot and cold temperatures. During the hottest part of the mission peak temperatures can be reduced if necessary by turning NMS off briefly during the sub-solar point of the orbit.

2.8 Ground Support Equipment

GSE Overview   The ground support equipment (GSE) performs test and calibration on individual components of the NMS instrument as well as the instrument as a whole. A rack of computer-controlled non-flight electronics that provided voltages to all the NMS electrodes and the electron gun emission control functions was used to tune and calibrate the quadrapole mass spectrometer (QMS) prior to integration of the QMS with the main electronics board (MEB). Meanwhile, other GSE tested the MEB and the flight software running on the MEB. In order to test the electronics without the QMS attached, the software team created simulators to generate data.

Two primary software applications perform the control and analysis functions. The "LadeeGSE" application sends commands and to the instrument and receives the telemetry stream. The "LadeeDataView" application allows the operator to view the telemetry data in graphs and tables either in real-time as the data arrives, or to review previously recorded data. Both applications were used during rack testing are still in use for operations.

The GSE has deep roots. The equipment and software were originally developed for Contour and have been used for instruments aboard Cassini and Mars Science Laboratory. The configuration of the GSE (Fig. 11) evolved as the instrument development phase moved from the early stages of testing and optimization to calibration then environmental qualification and finally to operation after integration with the spacecraft.

Electronics GSE   This GSE rack generates all the signals required to operate the mass spectrometer. This includes all of the high voltage lenses, the high voltage electron multipliers and the regulated current to the filaments. Pulse counters in the rack also read the detector signal. Custom software on a Linux-based workstation operates the mass spectrometer to allow lens tuning and instrument calibration.
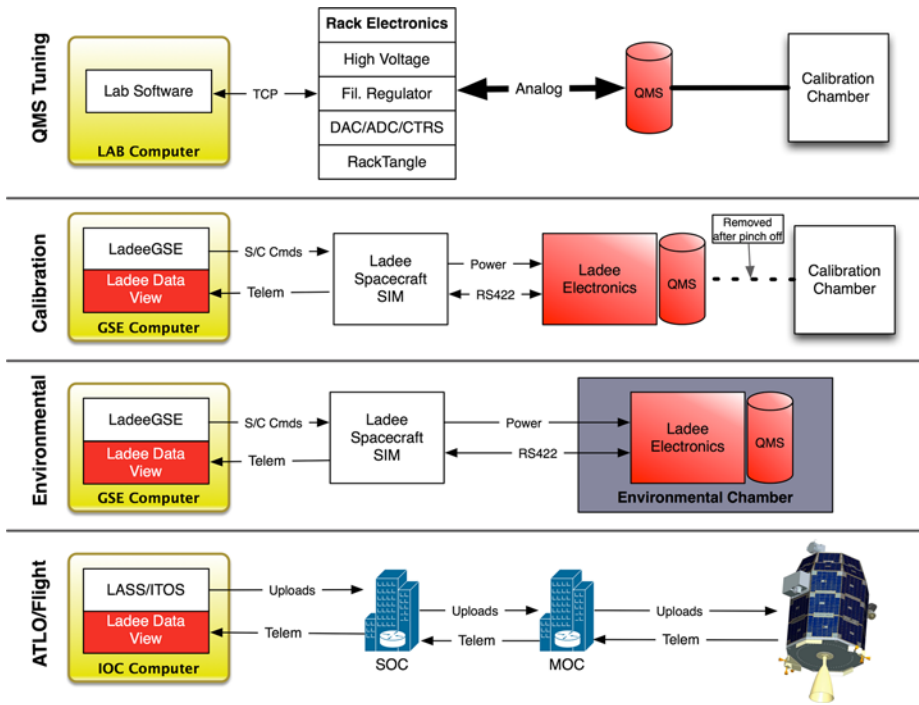
Fig. 11 Migration of the GSE configuration from early development and testing to the Assembly and Test for Launch Operations (ATLO) phase of the mission

Mechanical GSE   This consists of the calibration chamber with associated pressure monitors and a gas manifold. The ultra-high-vacuum system provides continuous vacuum pumping to maintain exceptionally low base pressures ($<1 \times 10^{-10}$ Torr). The gas manifold and associated pressure monitors allows the injection of calibration gases at controlled pressures.

Spacecraft and Instrument Simulators   The spacecraft simulator consists of a set of circuits in a USB-connected laptop-controlled box that provides power and commanding and communication to the NMS instrument equivalent to that provided by the spacecraft. This system was used during qualification and environmental testing and after the NMS had been delivered to the spacecraft bus prior to integration.

NMS flight software commands are sent from the GSE computer to the simulator through a TCP connection (Fig. 12). The simulator converts the commands to the high-speed serial bus that is used aboard the spacecraft. Telemetry from NMS is received by the simulator and passed through via the TCP port to the GSE data viewer application.

The QMS simulator generates artificial mass spectra that allow the NMS flight software to react as if it were acquiring real data. This provides high fidelity testing of flight software and flight scripts as well as verifying end-to-end functionality of software tools. An ideal perfect mass spectrum can be generated and verified to pass through the instrument and to the analysis tools unchanged.
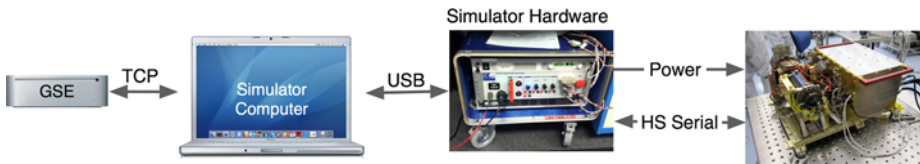
Fig. 12 Elements of the spacecraft simulator including the GSE laptop, the Universal Serial Bus (USB) communication link, the hardware that provides power and digital communication with the flight electronics, and at the far right the flight electronics

Table 2 EMI/EMC tests conducted on the NMS

Test ID	Type	Frequency Range
CE101	Power Leads	30 Hz–10 kHz
CE102	Power Leads	10 kHz–10 MHz
CMCE	Power & Signal Leads	150 kHz–200 MHz
RE102	E-Field	2 MHz–18 GHz
CS101	Power Lines	30 Hz–150 kHz
CS114	Bulk Cable Injection	150 kHz–200 MHz
RS103	E-Field	10 kHz–18 GHz
n/a	Grounding/Bonding	–

3 Instrument Qualification and Calibration

3.1 Environmental Testing

The integrated LADEE NMS instrument was subjected to a full environmental test campaign to demonstrate instrument performance at the anticipated launch and science conditions for the LADEE mission. All tests were conducted to protoflight levels.

EMI/EMC Test An electromagnetic interference and compatibility (EMI/EMC) test was performed at the GSFC EMI/EMC Test Facility to characterize possible interference sources emanating from NMS as well as identifying any vulnerabilities in both a conducted and radiated configuration. The specific EMI/EMC tests are summarized in Table 2. The tests were conducted in accordance with the standard MIL-STD-461F. The test set up for conducted emissions and susceptibility, and radiated emissions and susceptibility are shown in Figs. 13a and 13b respectively.

Conducted emissions testing measured the levels of NMS narrowband conducted emissions over the NMS power and signal leads. The results demonstrate that the NMS did not exhibit any exceedances above the specified limits within the specified frequency ranges.

Radiated emission testing was performed to measure the levels of radiated emissions emanating from NMS or associated cable harnesses between 10 kHz–18 GHz. Test results indicate that NMS exceeded the specified test limits between 40–180 MHz with a maximum 19 dB exceedance at 140 MHz, between 220–380 MHz with a maximum 16 dB exceedance at 320 MHz, and lesser exceedances (< 3 dB) at 2.04 GHz and 2.06 GHz. A S/C level EMI analysis was conducted and it was determined that the NMS exhibited exceedances were not mission critical as they occurred during portions that NMS would be powered off.

Conducted susceptibility testing was performed to ascertain degradation in NMS performance when exposed to conducted RF. Test results show that NMS exhibited no degradation in performance when subjected to RF signals injected into the NMS power and signal leads.
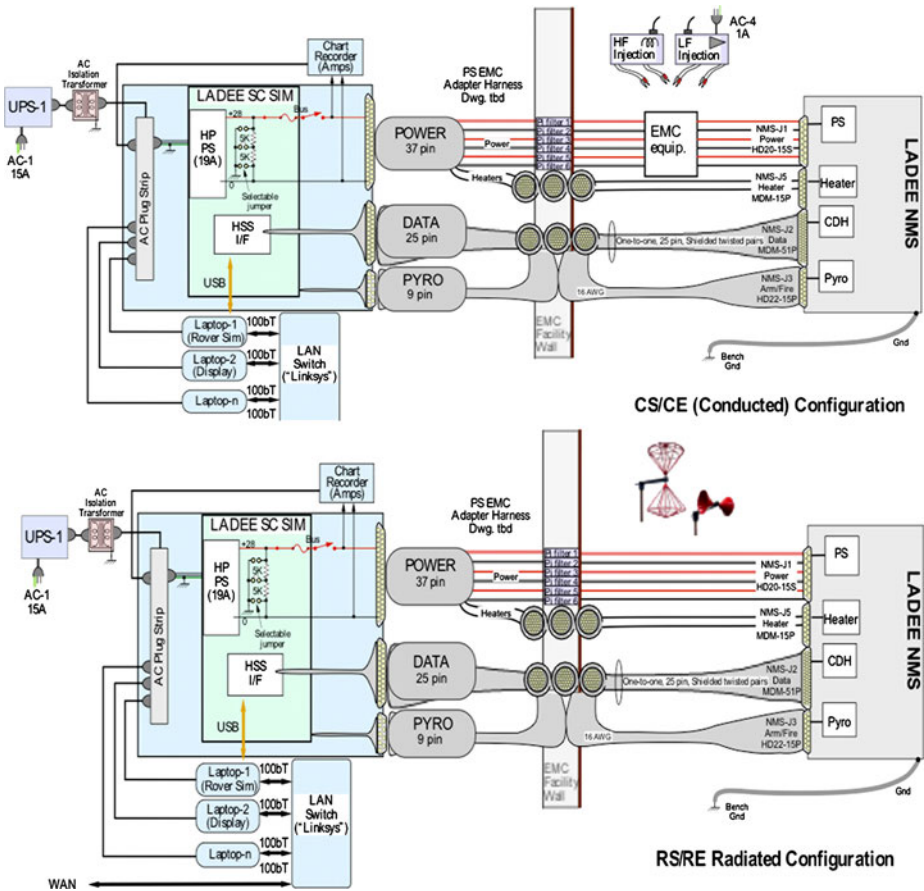
Fig. 13 The configuration for conducted and radiated EMI/EMC tests are shown the *top* and *bottom panes* respectively

Radiated susceptibility testing was performed to characterize degradation in NMS performance when irradiated at various frequencies. The NMS instrument was not susceptible to electric fields in the range of 2 MHz–18 GHz.

Random Vibration Test   The flight NMS was tested to the proto flight random, sinusoidal, and sine burst vibration levels as defined by the anticipated LADEE mission loads environment. Testing was performed at the Goddard Space Flight Center (GSFC) Vibration Test Lab.

Accelerometers (Fig. 14) were attached to the instrument in order to monitor the acceleration responses during testing.

During testing the instrument was double bagged in order to protect it from contamination. Additionally, a nitrogen gas flow was established into the inner bag in order to create a positive pressure in the bag to prevent contamination and maintain low humidity within the bag. At the conclusion of the *X* axis series of proto flight tests, the electrical baseline test results indicated an electrical anomaly. Further examination revealed that the electrical anomaly was due to a piece of conductive foreign object debris (FOD) as well as a sharp

Fig. 14 NMS prepared for vibration tests with accelerometers attached (*top pane*) and bagged and mounted on the vibration plate (*lower pane*)
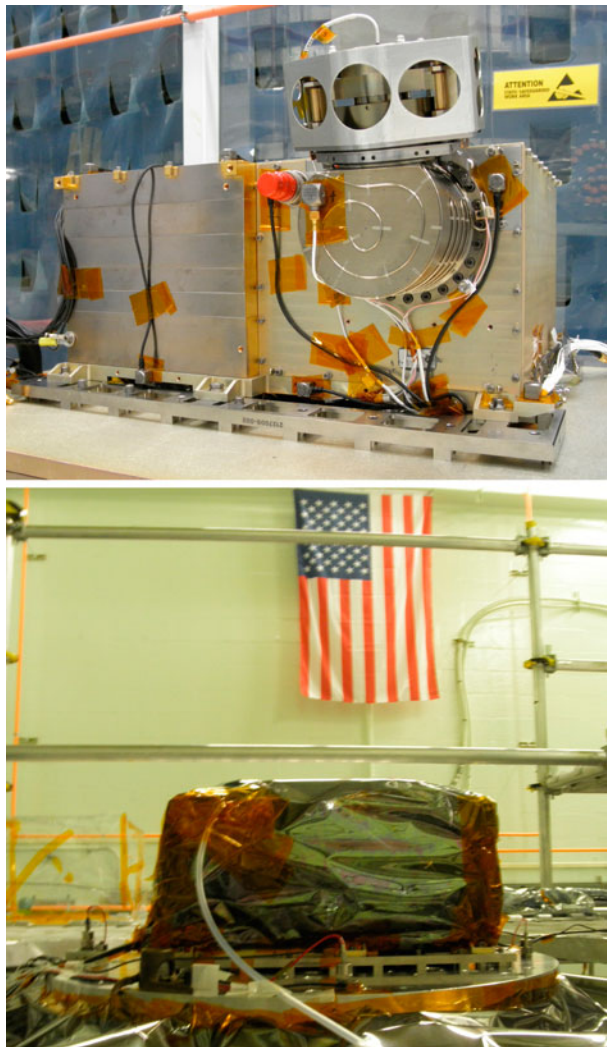
edge at one location within the NMS instrument which compromised some harness insulation. These issues were corrected and the NMS instrument was reassembled returned for vibration testing. Before resuming the *Y* axis proto flight test, the NMS was subjected to a *X* axis minimum workmanship level random vibration test and *X* axis proto flight level sinusoidal test at the levels specified by the Goddard General Environmental Verification Specification (GEVS), with no apparent damage to the assembly. The proto flight level *Y* and *Z* axis series of tests were resumed and completed.

The test met the success criteria with visual inspection, pre and post-test sine sweep signatures showing less than a 5 % shift in frequency, and successful completion of the between-axis EBT and the post-vibration functional tests.

Thermal Balance and Thermal Vacuum Tests   The NMS instrument was configured with flight-like thermal blankets and underwent a thermal balance test to validate the NMS ther-
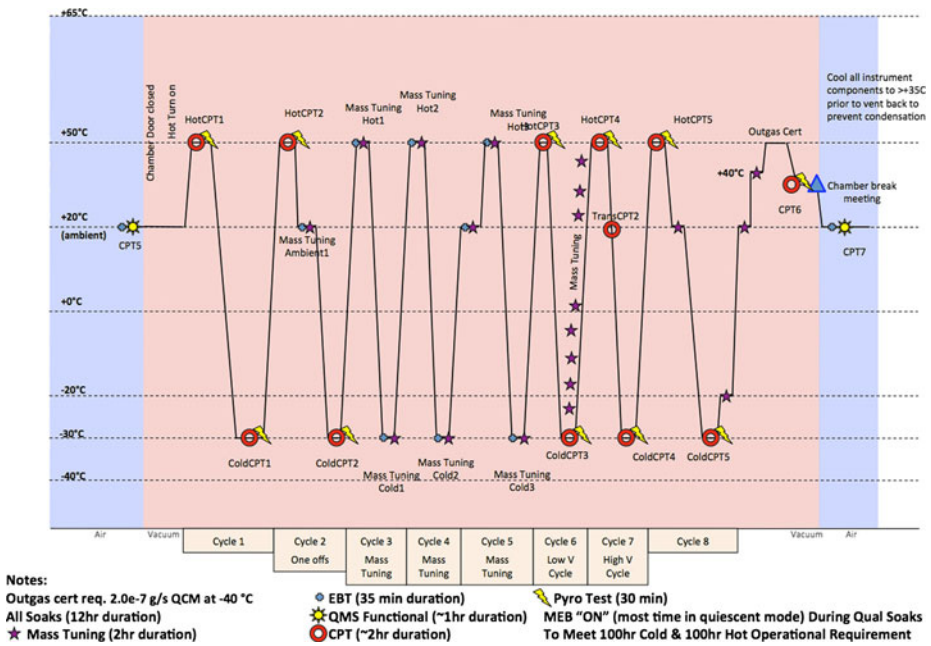
Fig. 15 The thermal vacuum sequences and tests run during this part of the environmental test program are illustrated. The 2 hour comprehensive performance test (CPT) exercised the full range of NMS operations

mal model which is used to generate temperature predictions during different phases of the LADEE mission. A special test science script was used to operate NMS in a flight-like manner at three different thermal balance temperatures spanning the NMS operational temperature range. Thermal simulations of different phases of the LADEE lunar orbit were conducted at each balance point to mimic subsolar operation, nominal science operation with 40 % duty cycle, and cold orbit operations. Thermal balance results were used to refine the NMS analytical thermal model by replacing an assumed instrument power dissipation level with an actual measured value of 34 watts. The NMS thermal model was used to generate on-orbit temperature. During the thermal balance testing, NMS was taken to the cold survival temperature of -40 °C. The NMS temperature was maintained at this level by the NMS survival heaters and held in this condition for 4 h. NMS was successfully powered on after this cold survival soak with no identifiable issues.

The NMS instrument was then reconfigured for thermal vacuum testing to allow for more expeditious temperature transitions for thermal cycling. The entire thermal vacuum profile is shown in Fig. 15. Eight thermal cycles were performed between the temperature range of -30 °C and $+50$ °C. Comprehensive Performance Tests (CPT) were conducted at each temperature plateau and select transitions. In order to compensate for thermal effects in the RF electronics, mass tuning activities were conducted at various temperatures during thermal vacuum testing. A hot turn-on was conducted during the first excursion to $+50$ °C with no identifiable issues.

The CPT results indicate nominal NMS performance was nominal from both an engineering and science acquisition perspective. Mass spectra (Fig. 16) taken of the encapsulated noble gas mix inside the QMS sensor demonstrate stable mass peaks across the entire operational temperature range.
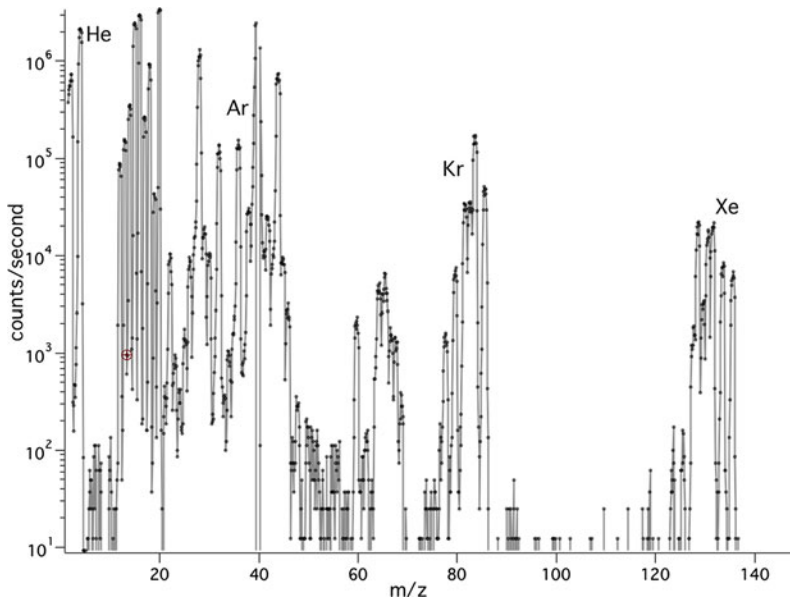
Fig. 16 A mass spectrum obtained in the fractional scan mode during calibration shows the noble gases introduced to allow the instrument performance over its full mass range to be monitored over time. The small chemical getter in the mass spectrometer helps reduce the density of active gases in the instrument while the getter does not pump the noble gases

3.2 NMS Calibration

The calibration of the mass spectrometer was initiated with the sensor connected to a static calibration manifold through a small umbilical tube. Calibration continued after the tube was pinched-off and during instrument final integration, environmental testing, pre-launch operations and post launch checkout. The calibration activities aimed to characterize instrument sensitivity over its mass range and to assess the stability of the instrument response in its flight environment.

During the initial calibration phases, He, Ne, Ar, Kr and Xe gases in pure forms or as mixtures were introduced into the NMS through a mixing manifold and the response of the instrument was established over a range of pressures. These gases were selected to provide signal over a wide mass range while avoiding interaction with the NMS getter (the getter does not pump noble gases). After this initial characterization, the sensor was sealed with a well characterized mixture of these nobles gases (17.25 % of He, 82.29 % of Ar, 0.36 % of Kr and 0.10 % of Xe) at a total pressure of 4.53×10^{-7} mbar. This mixture was used to assess variations in the instrument response as it went through integration, environmental testing, and pre and post launch assessments.

Since the instrument sensitivity varies slightly as a function of how the filaments and the multipliers are paired during operations, a set of calibration data were acquired for the trio CS filament #1/ OS filament #1\ CEM #1 as a group and for the trio CS filament #2/ OS filament #2\ CEM #2 as a group. The latter being chosen as a primary group for flight operations.

Characterization of the Detection Chain
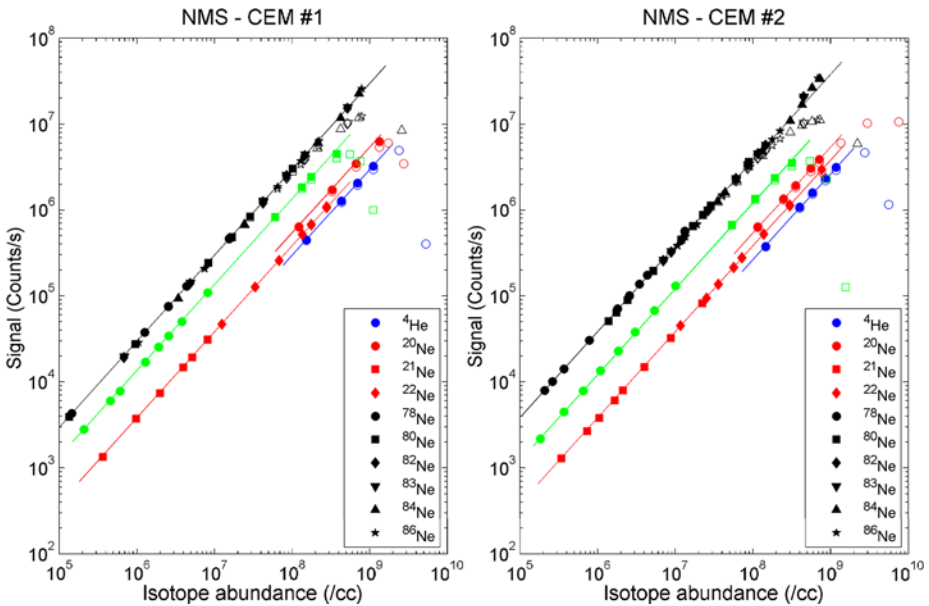
Fig. 17 Linearity of the Channel Electron Multipliers (CEMs) for He, Ne, Ar, and Kr collected using the closed source with a filament emission of 200 µA. *Clear symbols* are the raw CEM values while *colored symbols* are the dead time corrected values (up to the CEM roll over point). The bias voltage of the CEMs used to acquire this data ranges from −2500 V to −2860 V. The intercept each linear fit (bias from $x = y$ line in the log-log scale) translates the sensitivity in log scale of the instrument for that given isotope. Note that ^{20}Ne sensitivity is different from that of ^{21}Ne and ^{22}Ne. This is due to the frequency change that occurs at 20.5 amu

Linearity and dead time correction: NMS relies on two identical and redundant detection chains. Each detection chain is comprised of a channel electron multiplier (CEM), a pulse amplifier, a pulse height discriminator and a counter. The linearity of each detector chain was established using He, Ne, Ar, and Kr for densities that range from 10^5 to 10^{10} atoms/cc. This density range provided a signal on these species and their associated isotopes that ranges from 10^3 c/s to 2×10^7 c/s. The data, presented in Fig. 17 shows that both chains have a very comparable gain for a CEM bias voltage lower than −2500 V. Moreover, the two detection chains exhibit good linearity up to 2×10^6 c/s above which they display a non-linear behavior common to all paralyzable counting systems. In such systems, as the counting rate goes up, a correction in the form of:

$$m = n \exp(-n\tau)$$

where n is the true event rate in counts/s, m is the measured event rate in counts/s and τ is the per event dead time in seconds associated with the detection chain. The required dead time correction for each detection chain was derived using measurements of Kr isotopes signals at multiple sensor pressures. The three-isotope experimental method (Fahey 1998) was used to mitigate the effect of isotopic mass fractionations of Kr introduced in most vacuum systems. Figure 18 shows the variation of the dead time τ as a function of ^{84}Kr abundance. The dead time for both detector chains can be fit by the analytical formula:

$$\tau = A \exp\left((mB)^C\right)$$

Fig. 18 Variation of the dead time correction with count rate for the Channel Electron Multipliers (CEMs) derived using Kr measurements. The coefficient of the exponential fit are provided for each detector
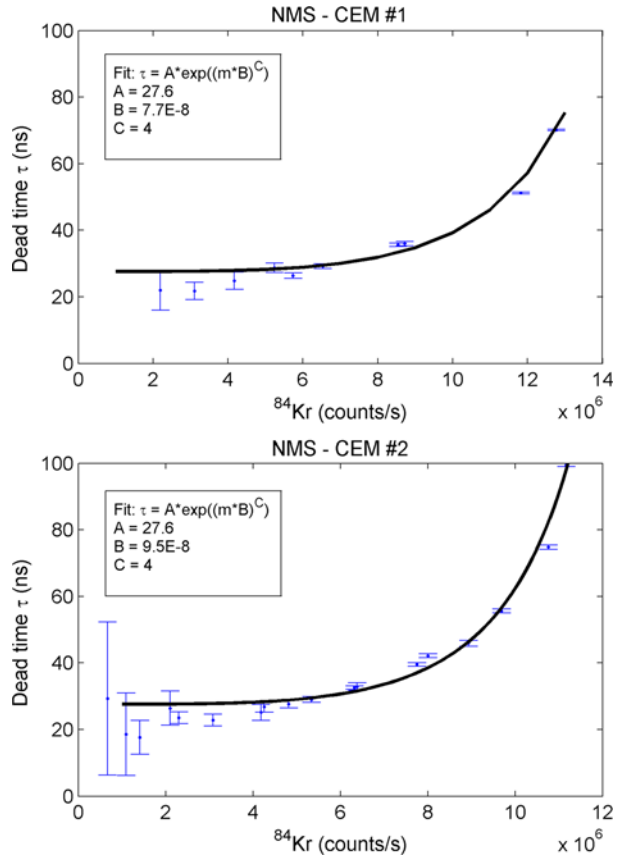

where A, B, C are constants that characterize each detector chain. Dead time corrected signals for He, Ar, Ne, and Kr are provided in Fig. 18 to show that the linearity of both detection chains can be extended up to 10^7 c/s after processing.

Pulse Height Distribution: The NMS instrument pulse height discriminator is commanded by an 8 bits DAC and provides 255 level of discrimination. The CEM bias voltage was decreased progressively from -2400 V during instrument integration and was set to -2800 V during the first two months of the mission. Pulse height distributions were acquired regularly throughout the development and operation phases to verify the performance of the CEMs. Figure 19 presents comparisons between He pulse height distributions for CEM #1 and #2 for bias voltages ranging from -2800 V to -2400 V. This pulse height distributions were acquired during the checkout phase of the instrument (few days after launch) while it was still sealed. As expected the gain of each multiplier increases as the bias voltage decrease from -2400 V to -2800 V. Moreover these data shows that CEM #2 has a higher gain and a better performance than CEM #1 for the same bias voltage. During normal operations, the discriminators of both detector chains were set to 28 DAC units, low enough to allow the discriminator to capture the majority of the multiplier pulses, but high enough to reject any low level noise that may trigger false counts. The bias voltage for both multipliers was set to -2800 V.

Noise level in the detector chain: The instrument was designed to minimize the noise level in the detector chain. This goal was achieved by a careful isolation of the multipliers from

Fig. 19 Pulse height distributions (PHDs) for CEM #1 and #2 using He. These PHDs were acquired at various bias voltages. The *dotted line* indicates the minimum discriminator setting that allows an effective noise rejection. The *solid line* indicated the discriminator setting used during nominal operations
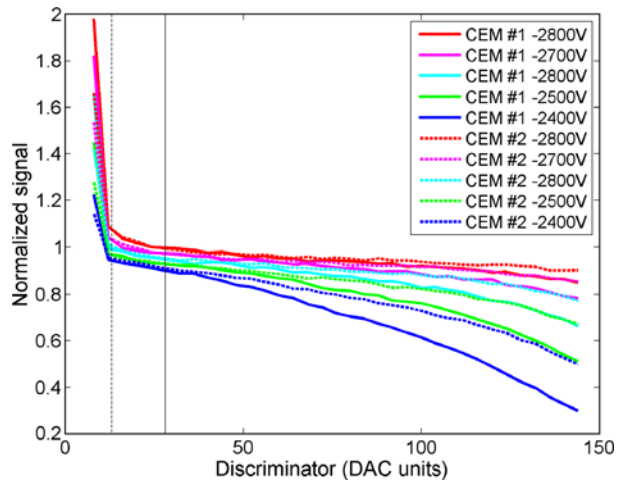
any stray electrons that originate in the ionization sources. Moreover, the detector electronics were placed at a very short distance from the multipliers to minimize noise pickup. Noise levels in the active detection chain were assessed by turning on the closed source while configuring the switching lenses to select the open source. In that configuration all recorded counts can be assumed to be noise. During instrument checkout the noise level on both detection chains were found to be less than 8 counts/min.

Instrument Chemical Background During integration the sensor underwent a multi-day high temperature bake out to insure the cleanliness of the internal surfaces and to minimize chemical background. Shortly after the ejection of the breakoff cap assembly, the instrument was assessed for the level of residual instrument background induced by internal surface outgassing, getter outgassing, filament outgassing, or spacecraft contamination. While this background tend to decay as the cumulative operational time of the instrument increases, the level and the nature of this background sets the detection limits of the instrument. Figure 20 shows the instrument background as it was measured in the first 3 months of the mission. This measurement is done by pointing the instrument boresight to the anti-ram direction. Filament outgassing is the source of most of the background in m/z 12–18, 28, and 44. Surface and getter outgassing are responsible for the residual water and for most of the hydrocarbon fragments seen in the spectra from both sources. As expected, the background in most mass channels decayed exponentially and was reduced by many several order of magnitudes after the first 3 months in space.

One would notice the much lower background level in the open source compared to the closed source. This lower background is the result of the presence of a 1 V retarding potential grid that rejects most thermal ions (energy below 1 eV). This electrostatic background suppression increases the SNR of the open source for energetic exospheric neutrals that may be the result of surface sputtering processes.

Although its apertures had no direct geometric views of the spacecraft, it was still possible the instrument chemical background could be influenced by the self-scattered flux of various molecular species outgassed from the spacecraft. These species were dominated by water vapor, which in high vacuum readily effuses from non-metallic materials contained within various electronics units, multilayer insulation blankets, and even the spacecraft structure itself. Based on an analytical development by Robertson from the Bhatnagar-Gross-Krook approximation to the Boltzmann equation (Robertson 1976), a relationship was
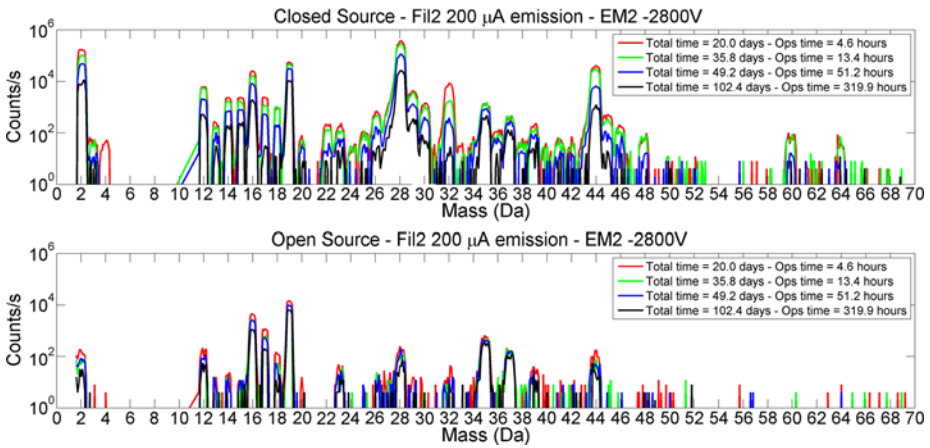
Fig. 20 Instrument background in the closed and open source modes collected at various days after the deployment of the breakoff assembly. Total time refers to the elapsed time since breakoff assembly while operation time refers to the cumulative time during which the filaments were on

developed that linked this sensitive chemical background contribution to limits on spacecraft outgassing of water vapor. Even accounting for the exposure history of LADEE to the high vacuum of space prior to commencement of operations, predictions indicated this limit could only be met if all bus gaps were sealed and a dedicated vent was incorporated into the spacecraft design to allow water vapor from internally-carried sources to be directed radially away from the observatory on the side opposite NMS.

Instrument Sensitivity The instrument sensitivity was initially measured in a static mode for He, Ne, Ar, Kr and Xe. In a static mode, the gas is leaked into the ionization source at a very low pressures and left to equilibrate before pressure readings are taken by an external stable ion gage while the corresponding instrument response is recorded. The measurements from the instrument are processed for dead time correction and background subtraction. After the sensor was pinched off sensitivities was continuously tracked using the noble gas mixture that was sealed in the instrument. The last direct sensitivities measurement for several multiplier voltage settings was conducted prior to the break-off cap ejection. This set of flight data was used to update the sensitivities that were established during ground calibration for the multiplier voltage and discriminator setting chosen for flight. The sensitivities in the closed source mode for the three key exospheric species (He, Ne and Ar) are provided in Table 3. Closed source normalized sensitivity S_n for another species s of mass m_s and electron ionization cross section (at 70 eV) σ_s can be derived through interpolation of the normalized sensitivities of Table 3 as a function of mass. To derive an absolute sensitivity S_a for the species, the normalized sensitivity S_n needs to be corrected for RF frequency and for ionization cross-section as:

$$S_a = S_n * C_{RF}(m_s) * \sigma_s$$

where C_{RF} is a sensitivity correction factor:

$$C_{RF} = \begin{cases} 0.71 & \text{if } m_s \leq 20.5 \\ 1.00 & \text{if } m_s > 20.5 \end{cases}$$

Table 3 NMS closed source sensitivities for He, Ne and Ar

Filament #	CEM #	Species	EI cross section[*] ($A°^2$)	Absolute sensitivity (counts/s)/(particle/cc)	Normalized sensitivity (counts/s)/(particle/cc)/A°
1	1	^{4}He	0.296	0.00351	0.00829
1	1	^{20}Ne	0.475	0.00687	0.01013
1	1	^{22}Ne	0.475	0.00485	0.01020
1	1	^{36}Ar	2.520	0.02702	0.01072
1	1	^{40}Ar	2.520	0.02639	0.01047
1	1	^{40}Ar^{2+}	0.137	0.00232	0.01184
2	2	^{4}He	0.296	0.00264	0.00625
2	2	^{20}Ne	0.475	0.00526	0.00775
2	2	^{22}Ne	0.475	0.00372	0.00784
2	2	^{36}Ar	2.520	0.02281	0.00905
2	2	^{40}Ar	2.520	0.02257	0.00896
2	2	^{40}Ar^{2+}	0.137	0.00285	0.01457

[*] Electron impact ionization cross sections are from Rejoub et al. (2002)

Fig. 21 Example of sensitivity variation due to mass peak shape drifts
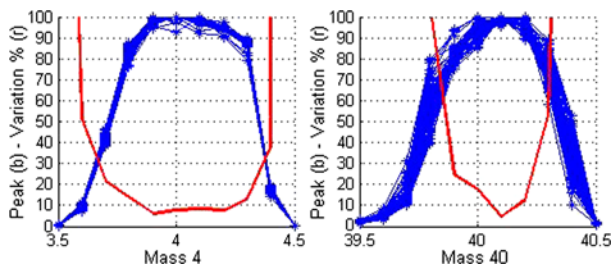
The sensitivity of the open source cannot be directly derived using the encapsulated calibration gas but will be determined in flight by comparing the count rates for exospheric He, Ne, and Ar that were collected alternately using the closed and the open source.

Sensitivity Dependence with Temperature   The NMS sensitivities will drift from the values given in Table 3 as the instrument electrical and mechanical components warm up from dissipated electrical energy. This sensitivity variation is mainly due to two sources:

1. Shifting of the position of mass peaks due to RF thermal drift.
2. Thermomolecular pressure difference that forms between the hot closed source and the much cooler sensor.

RF thermal drift: Due to fringe field effects in the quadrupole rods, the transmission of the mass filter varies for small excursions from the center target mass. This creates small structures in any given mass peak. As the RF electronics warms-up the AC and DC analogue outputs drift slightly. These voltage drifts will slightly shift (up to 0.2 Da) the selected mass on the targeted peak and consequently the observed count level. If the density of the measured gas is constant, this drift will show as a sensitivity change for the measured species (Fig. 21).

The amplitude of these sensitivity changes are temperature and mass dependent. Table 4 presents the maximum perceived sensitivity change as measured during the NMS thermal

Table 4 Maximum sensitivity variation observed during NMS thermal qualification (-30 °C to $+50$ °C)

Mass	Variation %
2.0	15.5
4.0	9.7
12.0	11.9
13.0	9.1
14.0	17.1
15.0	14.2
16.0	17.3
20.0	13.6
28.0	17.3
36.0	17.6
40.0	17.5
44.0	16.5

qualification tests. During those tests the instruments was operated at varying temperatures (from -30 °C to $+50$ °C). The sensitivity variations values provided in Table 4 should be taken into consideration when calculating the uncertainty of the NMS measurement.

Thermomolecular pressure difference: The instrumental effects on sensitivity discussed above relate to the efficiency of conversion of gas in the closed source to ions and thence to detector counts. In as much as NMS operation requires a hot filament, there is a wide range of temperatures within the instrument, which, in turn, results in a non-uniform distribution of gas density. The equivalent of hydrostatic equilibrium for a collisionless gas in a bounded system like the closed source and its appendages is $nc = $ constant, where n is local gas density and $c = \sqrt{kT/2\pi m}$ is one-fourth the mean thermal speed of atoms of mass m. The effective gas temperature T is a local average of internal surface temperatures. At the interface of the closed source entrance and the lunar exosphere the flux of atoms out of the instrument is $n_{CS}\sqrt{kT_{CS}/2\pi m}$ and the influx from the exospheric influx is

$$\phi_{exo} = \int_{-\infty}^{\vec{x}\cdot\vec{v}_{sc}} dv_x (\vec{x}\cdot\mathbf{v}_{sc} - \mathbf{v}_x) \int_{-\infty}^{\infty} dv_y \int_{-\infty}^{\infty} dv_z f_{exo}(\mathbf{v})$$

where the x-axis coincides with the axis of the field of view of the CS, $\vec{x}$ is a unit vector in the $+x$ direction, $\mathbf{v}_{sc}$ is the spacecraft velocity, and f_{exo} is the exospheric velocity distribution function. If f_{exo} is approximated as Maxwellian, the evaluation of the integrals is trivial, and the influx to the CS can be expressed as
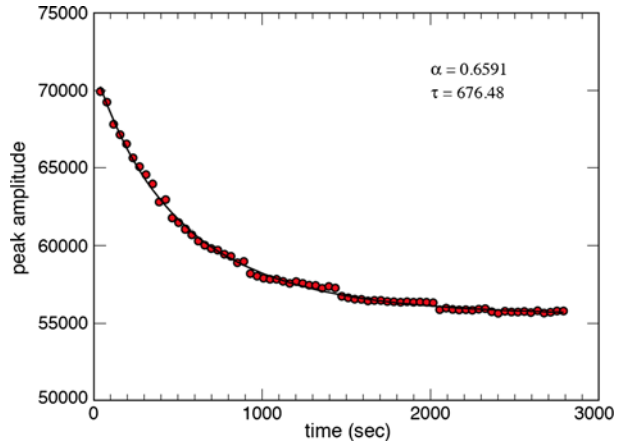
$$\phi_{exo} = n_{exo} v_{eff}$$

where the effective velocity is

$$v_{eff} = \frac{\mathbf{x}\cdot\vec{v}_{sc}}{2}(1 + \operatorname{erf}(\mu)) + \sqrt{\frac{kT_{exo}}{2\pi m}} \exp(-\mu^2)$$

$\mu = \vec{x}\cdot\mathbf{v}_{sc}\sqrt{m/2kT_{exo}}$, n_{exo} is the exospheric concentration, and m is atomic mass.

Fig. 22 Sequential CS measurements of ^{36}Ar in detector counts per second prior to cap ejection. Time is measured from the application of power to the filament

In other words, the relationship of detector output, δ (counts per second), to the concentration of atoms in the exosphere is

$$n_{exo} = \frac{\delta}{S_a v_{eff}} \sqrt{\frac{kT_{CS}}{2\pi m}}$$

The time dependence of the temperature of the closed source, T_{CS}, as it is heated by the active filament has been determined from a dedicated sequence of repeated measurements of the ^{36}Ar peak, in flight but before the cap was ejected. Results of this experiment are shown as dots in Fig. 22. The data are interpreted as

$$n_{CS} = n_0 \sqrt{T_{CS}/T_0}$$

and the subscript 0 identifies initial conditions. The underlying curve is

$$n_0 \left[1 + \alpha \left(1 - e^{-t/\tau} \right) \right]^{-1/2}$$

where t is time from filament turn-on, $\alpha = 0.6591$, and $\tau = 676.48$ s. The fit is sufficiently strong to suggest that

$$\frac{T_{CS}(t)}{T_0} = 1 + \alpha \left(1 - e^{-t/\tau} \right)$$

is a good approximation for modes of operation wherein only the CS is active, and the CS is active continuously.

4 Instrument Operations and Expected Results

4.1 Overview of NMS Measurement Modes

NMS measurement scenarios that impact the spacecraft attitude are RAM, TILT, WAKE, and ION campaigns. In the RAM mode the spacecraft points the NMS closed source inlet along the velocity vector and the spacecraft rotates at 1 revolution per orbit. This mode
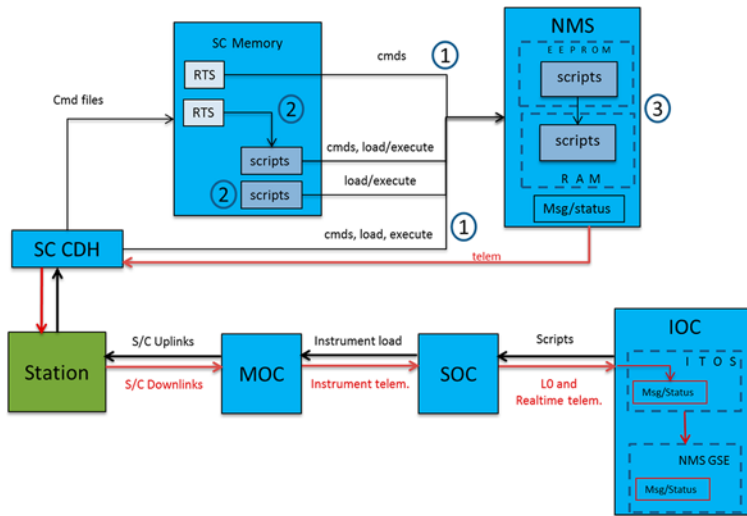
Fig. 23 The command and telemetry paths to the NMS from the Instrument Operations Center (IOC) shown in the *bottom right*, to the Science Operations Center (SOC), the Mission Operations Center (MOC), the uplink station, and the spacecraft command and data handling system (SC CDH) to the NMS. As illustrated, scripts can also be retrieved from the spacecraft memory and downloaded to the memory of the NMS

is the primary mode for measurement of He and Ar and other inert species and the wide field of view of the closed source allows a relaxed 2 degree pointing requirement. WAKE is designed to allow instrument background measurements to be made by pointing the NMS 180 degrees away from RAM. LExS models show that a negligible flux of gas enters the closed source in this configuration. TILT mode is intended to optimize open source measurements for sputtered species that would not be detected after a collision with a surface in the mass spectrometer. A typical tilt away from RAM pointing of the open source axis would be 30 degrees toward nadir although other tilt angles are possible to optimally match the sputtered velocity with the spacecraft orbital velocity of 1.6 km/sec. Particles with energies of greater than $\sim$25 eV will not be detected by the NMS in the open source mode at the nominal settings of the quadrupole deflector (Fig. 5). ION mode to reorients the axis of the spacecraft perpendicular to the orbital plane to search for ions in the NMS open source. Ions are only expected to be detected if the magnetic field happens to be in a direction that enables pick up ions to flow into the open source.

4.2 Commanding and Operations Overview

Operationally, since power sharing is required, the instrument is only powered for $\sim$48 minutes for observations. During this time the instrument is powered on, loaded, configured, and started for the science scenario, and then powered off again at the end of the window. All operations must be guided within this window. During the early checkout and commissioning phases, this restriction is not needed and functional testing is allowed longer durations; such as the CPT. The NMS operation is thought of in two separate disciplines: the commanding performed to the instrument and the data received from the instrument. Figure 23 shows the general overview of the end-to-end paths for each of these functions.

Commanding   The primary mode of commanding the instrument is through stored files of commands and code functions called scripts. There are two comprehensive scripts, one functional and one science, which define all operations desired for the instrument in a modular format. This allows loading smaller configuration scripts to define how the operations will be executed (i.e., which modules to execute). The functional script is stored in EEPROM and config files are loaded to define checkout activities, from as simple as an aliveness check to a comprehensive performance test. As would be expected, the science configurations orchestrate the collection scenarios throughout the lunar orbits, by interacting much more intensively with the hardware in setting the various DACs, etc. The script processor is and adaptation of that developed for SAM commanding and is a small, portable system that enables implementation of complex measurement sequences without the generation of new low level code. The scripting language provides access both to the NMS count data and to all housekeeping data. It is integrated with the alarm handler and incorporates a scriptable timer for periodic operations. A library is included for commonly used functions. The script processor enables rapid changes to flight sequences should this be desired.

Individual commands are also used for the instrument, to perform pre-defined functions, such as loading memory or controlling the execution of scripts. A more general RAW command is also used for invoking subfunctions that are not easily defined ahead of time. These database-defined commands use an upload execution code to define what priority the FSW needs to give to the execution (i.e., store for later or execute immediately).

Commanding is handled operationally in three ways, each allowing a slightly different functionality:

1. Individual commands either directly from the ground to the instrument, or from the CDH to the instrument on invocation of stored sequences of commands in spacecraft memory.
2. Script files that are loaded to the instrument and invoked, either directly from the ground or from the CDH on invocation of stored sequences of commands in spacecraft memory.
3. Script files previously loaded to the instrument invoked from the EEPROM.

Individual Commands   Transmission of individual commands (Sequence 1 in Fig. 23) allows more conservative stepping of procedures and insight to success and end-item verification. From the GSE, these commands are transmitted through use of ITOS, resident in the IOC via a VM connection (see GSE section). They are defined in the Project database and selected through a GUI interface. It is also possible that commands can be sent from sequences stored in spacecraft memory, called Relative Time Sequences (RTSs). These are generated using ITOS features and the database to compile the files and upload them to the Observatory for later use. This allows activities requiring sequences of commands to be performed more easily and with less reliance on solid communication with the MOC.

Scripts by 'Load-and-Go'   The primary commanding of the instrument is via loading the desired script(s) to the instrument memory and commanding it to execute; coined 'load-and-go' execution (Sequence 2 in Fig. 23). This can be accomplished from the ground or from RTS. If commanded from the ground, the prime script is transmitted to instrument memory, followed by the configuration script, then the command to execute is sent. If performed via RTS, the scripts are loaded to the instrument-designated directory in spacecraft memory, the RTS(s) is loaded to the correct slot in spacecraft memory, and then the RTS is executed to load the scripts and execute the sequence.

Scripts from Memory   Scripts can also be stored in the instrument memory, then commanded to RAM and started (Sequence 3 in Fig. 23). This is the method used when executing functional tests. Functional tests are primarily used during the initial checkout activities after launch. This can be performed from the ground or via RTS. The primary script is loaded to RAM, the configuration script applied, and then the command is sent to begin the activity.

Planning Activities   In order to ease the complicated sequencing needed between subsystems and entities to perform a successful science collection scenario, the scenarios are defined through use of activities in the LASS planning tool. These activities dictate the RTS required, script files needed, pre and post sequences needed (such as power on/off), Observatory attitude required, data rates, etc. An activity is the comprehensive inclusion of all required resources for success. This is translated into the entire series of commands to orchestrate the end-to-end operation of that science scenario. For NMS, these scenarios are defined as the RAM, TILT, WAKE, and ION campaigns.

Product Configuration Management   As with all efforts, an important aspect is the control of that effort to ensure consistency and safety of the instrument. All scripts used for the FM are verified via the team CM process; requiring first review of the script. Following completion of that gate, it is initially placed in the SVN repository and execution on the breadboard is carried out. Once verified as safe from doing harm to the instrument, it is tested on the EM. After successful completion of this process, the script is finalized in the SVN system and marked ready for flight. The script is then transferred to the MOS SVN repository to await approval and implementation.

Telemetry   Telemetry is received by two different methods: real-time dataflow to the IOC and post-event file retrieval.

Only housekeeping telemetry is received during real-time contacts. This data is passed from the MOC, through the SOC, to the IOC in CCSDS frames (acronyms referenced in Table 5). At the IOC, the ITOS VM both unpacks the NMS Instrument Transfer Frames (ITF's) and transfers to the LADEE GSE software for processing, and processes some of the data for display itself. This data is used for assessment of the health of the MEB and QMS. Both OTPS and LADEE GSE software packages allow limit checking and plotting besides the usual conversion displays.

All NMS data, housekeeping and science, is downloaded from the Observatory and stored in separate files of CCSDS frames on the MOS file system for retrieval. These files are retrieved and processed into NMS ITF format for acceptance by the various analysis tools and databases.

'GOLD' Dataset   The retrieved science data dump files retrieved from the MOS file system are used to create the comprehensive dataset for the science collection, known as the 'GOLD' dataset. This is then submitted to the repository and fed to a database for use by the LADEE science team.

4.3 Data Archiving

The full set of NMS data will be archived in the atmospheres node of the Planetary Data System within 4 months of the end of the mission. The NMS archived data will include all detector count data for each m/z value sampled and will include the full set of NMS housekeeping data that enables the commanding of the instrument to be understood. Data

Table 5 Acronyms

ADC	Analog to Digital Converters
AMUX	Analog Multiplexer
BA	Bayard-Alpert
CCSDS	Consultative Committee for Space Data Systems
CDH	Command Data Handling
CEM	Channeltron Electron Multiplier
CPT	Comprehensive Performance Tests
CONTOUR	Comet Nucleus Tour
CRAF	Comet Rendezvous Flyby Mission
CS	Closed Source
CTL	Control
Da	Dalton
DAC	Digital to Analog Converter
DET	Detector (electronics circuit)
EEPROM	Electrically Erasable PROM
FOD	Foreign Object Debris
GEVS	Goddard General Environmental Verification Specification
GSE	Ground Support Equipment
GSFC	Goddard Space Flight Center
HV	High Voltage
IF	Ion Focus (electronics circuit)
INMS	Ion and Neutral Mass Spectrometer
LDEX	Lunar Dust Experiment
LExS	Lunar Atmosphere Simulation
LADEE	Lunar Atmosphere and Dust Environment Explorer
MEB	Main Electronics Box
MOC	Mission Operations Center
NGIMS	Neutral Gas and Ion Mass Spectrometer
NMS	Neutral Mass Spectrometer
OMM	Orbital Maintenance Maneuver
OS	Open Source
QMS	Quadrupole Mass Spectrometer
PROM	Programmable Read Only Memory
PRT	Platinum Resistive Thermometer
PS/HV	Power Supply/High Voltage (circuit)
PWM	Pulse Width Modulator
RF	Radio Frequency
SAM	Sample Analysis at Mars
SOC	Science Operations Center
SRAM	Static Read Only Memory
T	temperature
USB	Universal Serial Bus
UVS	Ultraviolet and Visible Light Spectrometer

Table 6 Data definitions for NMS

Product name	Description	Estimated size (B = Bytes)	Type	File label
Calibration Housekeeping	Instrument housekeeping packets	6000 KB	Raw ground calibration	gnd_hk
Calibration Science	Instrument science packets	600 KB	Raw ground calibration	gnd _sci
Calibration Message Log	Instrument message log	10 KB	Raw ground calibration	gnd _msg
Calibration Markers	Instrument markers	10 KB	Raw ground calibration	gnd _mkr
Raw Housekeeping	Instrument housekeeping packets	6000 KB	Raw flight	raw_hk
Raw Science	Instrument science packets	600 KB	Raw flight	raw_sci
Raw Message Log	Instrument message log	10 KB	Raw flight	raw_msg
Raw Markers	Instrument markers	10 KB	Raw flight	raw_mkr
Calibrated Housekeeping	Instrument housekeeping packets	6000 KB	Calibrated flight	calib_hk
Calibrated Science	Instrument science packets	600 KB	Calibrated flight	calib_sci
Calibrated Message Log	Instrument message log	10 KB	Calibrated flight	calib_msg
Calibrated Markers	Instrument markers	10 KB	Calibrated flight	calib_mkr

generated by the NMS instrument will be organized in products according to their processing state and will adhere to the nomenclature of product definition set by the LADEE project. The NMS pipeline processes the Packet Data (binary files as generated by the instrument) to generate the Raw, and Calibrated products that will be archived at the PDS (Table 6).

The Packet Data will be separated by telemetry channel (Housekeeping, Science and Instrument Log) and converted to ASCII to generate the Raw Housekeeping, the Raw Science and the Message Log. These data will be checked for anomalies and will be time-stamped. The Housekeeping units will be expressed in engineering units (Volts and Digital Numbers) when applicable.

Then, the Raw Science will be corrected for detector response (dead time correction) and the Raw Housekeeping will be converted to scientific units (physical unit corresponding to the measurement being made: for example deg C for Temp, A for current or emission, and V for voltage monitor circuits) when applicable. These data will be checked for anomalies and the time-stamp will be corrected for any offset between the instrument and spacecraft clocks. This process will yield Calibrated Housekeeping and Calibrated Science ASCII files.

4.4 Summary

The extended LADEE mission duration that extends coverage for the LDEX, UVS, and NMS instruments through multiple lunations together with regular measurements at tens of kilometers above the surface is intended to enable the variability of both gas and dust in the lunar exosphere to be explored. The observations of emissions many kilometers above the surface by the Apollo astronauts may be better understood after this mission and the lunar environment better characterized before humans again return to the moon and further perturb

this tenuous atmosphere. The NMS and UVS will provide complementary measurements for variations in the known gases (He, Ar, Na, K) the search for new species with NMS targets including He and Ar and UVS targets Na and K and both instruments searching for yet to be measured gases such as CH_4, CO, CO_2, H, H_2O, N, C, S, Si, Al, Ca, Fe, Ti, Al Mg, OH or reductions in their upper limits. The detailed characterization of a surface boundary exosphere should enable better predictions of the space environment around the many similar objects in our solar system.

References

A. Fahey, Measurements of dead time and characterization of ion counting systems for mass spectrometry. Rev. Sci. Instrum. **69**, 1282 (1998)

R.R. Hodges Jr., Applicability of a diffusion model to lateral transport in the terrestrial and lunar exospheres. Planet. Space Sci. **20**, 103 (1972)

R.R. Hodges Jr., Paper presented at the Lunar and Planetary Science Conference Proceedings, n/a 1, 1980

R.R. Hodges Jr., J.H. Hoffman, Measurements of solar wind helium in the lunar atmosphere. Geophys. Res. Lett. **1**, 69 (1974)

R.R. Hodges Jr., J.H. Hoffman, Paper presented at the Lunar and Planetary Science Conference Proceedings, n/a 1, 1974

R.R. Hodges Jr., F.S. Johnson, Lateral transport in planetary exospheres. J. Geophys. Res. **73**, 7307 (1968)

R.R. Hodges, Ice in the lunar polar regions revisited. J. Geophys. Res., Planets **107**, 6-1 (2001)

R.R. Hodges, Resolution of the lunar hydrogen enigma. Geophys. Res. Lett. **38**, 6201 (2011)

R.R. Hodges, J.H. Hoffman, F.S. Johnson, The lunar atmosphere. Icarus **21**, 415 (1974)

W. Kasprzak et al., Paper presented at the Society of Photo-Optical Instrumentation Engineers (SPIE) Conference Series, October 1, 1996

P.R. Mahaffy, Characteristics of an electrostatic quadrupole deflector. J. Vac. Sci. Technol. **8**, 3244 (1990)

P.R. Mahaffy et al., The sample analysis at Mars investigation and instrument suite. Space Sci. Rev. **170**, 401 (2012)

H.B. Niemann et al., Pioneer Venus Orbiter neutral gas mass spectrometer experiment. IEEE Trans. Geosci. Remote **18**, 60 (1980)

H.B. Niemann et al., Galileo Probe Mass Spectrometer experiment. Space Sci. Rev. **60**, 111 (1992)

H.B. Niemann et al., The Planet-B neutral gas mass spectrometer. Earth Planets Space **50**, 785 (1998)

H. Niemann et al., Paper presented at the Huygens: Science, Payload and Mission, n/a 1, 1997

R. Rejoub, B.G. Lindsay, R.F. Stebbings, Determination of the absolute partial; and total cross sections for electron-impact ionization of the rare gases. Phys. Rev. A **65**, 042713 (2002)

S.J. Robertson, BGK model solution of back scattering of outgas flow from spherical spacecraft. Prog. Aeronaut. Astronaut. **51**, 1 (1976)

N.W. Spencer, G.R. Carignan, In situ measurements of thermospheric composition, temperature, and winds by mass spectrometry. Adv. Space Res. **8**, 107 (1988)

S.A. Stern, The lunar atmosphere: history, status, current problems, and context. Rev. Geophys. **37**, 453 (1999)

J. Veverka et al., Comet nucleus tour. Acta Astronaut. **35**, 181 (1995)

J.H. Waite et al., The Cassini Ion and Neutral Mass Spectrometer (INMS) Investigation. Space Sci. Rev. **114**, 113 (2004)

P.B.A. Wurz, V. Coffey, B.K. Dichter, W.T. Kasprzak, A.J. Lazarus, W. Lennartsson, J.P. McFadden, in *ISSI Scientific Report*, ed. by M.E.S. Wuest, R. von Steiger. International Space Science Institute (2007)

A. Yaniv et al., Paper presented at the Lunar and Planetary Science Conference Proceedings, n/a 1, 1972

An Overview of the LADEE Ultraviolet-Visible Spectrometer

Anthony Colaprete · Kara Vargo · Mark Shirley ·
Dave Landis · Diane Wooden · John Karcz ·
Brendan Hermalyn · Amanda Cook

Abstract The Ultraviolet-Visible Spectrometer (UVS) instrument, which flew on the Lunar Atmosphere and Dust Environment Explorer (LADEE) spacecraft (SC), was one of three science instruments used to characterize the lunar exosphere. UVS is a point spectrograph operating between 230–810 nm and used its two optical apertures to make observations of the exosphere just above the surface at a range of local times and altitudes, as well as making solar occultation measurements at the lunar sunrise terminator. The instrument was led out of NASA Ames Research Center with primary hardware being provided by Draper Laboratories. Final instrument integration, testing and operations were performed at NASA Ames. Over the course of the 140-day LADEE mission UVS acquired more than 1 million spectra, providing a unique data set for lunar exosphere gasses and dust.

Keywords LADEE · Lunar Exosphere · Moon · Spectroscopy

1 Science Background and Objectives

The Lunar Atmosphere and Dust Environment Explorer (LADEE) was an orbital lunar science mission designed to address the goals of the 2003 National Research Council decadal survey (2003), the Lunar Exploration Analysis Group Roadmap (2011), and the "Scientific Context for Exploration of the Moon" (SCEM) report (2007), and had been recommended for execution by the 2011 Planetary Missions Decadal Survey (2007). The LADEE mission goal is to determine the composition of the lunar exosphere and investigate the processes that control its distribution and variability, including sources, sinks, and surface interactions. It monitored variations in known gases, such as sodium, potassium, argon and helium, and

A. Colaprete (✉) · K. Vargo · M. Shirley · D. Wooden · J. Karcz · A. Cook
NASA Ames Research Center, Moffett Field, Mountain View, CA, USA
e-mail: Anthony.Colaprete-1@nasa.gov

D. Landis
Draper Laboratory, Tampa, FL, USA

B. Hermalyn
University of Hawaii, Honolulu, HI, USA

Table 1 LADEE UVS species called out in L1/2 requirements with examples of approximate line centers (most species have more than one potential line) (Sarantos et al. 2012), g-factor and assumed L1 pre-LADEE upper limits or average measured value (in the case of Na and K). g-factors are from Sarantos et al. (2012) unless otherwise noted

Species	Emission/Absorption Center (nm)	g-factor (ph sec^{-1})	L1 Upper Limits (#/cc)
OH[1]	308	0.00047	1.E+06
Al	396.3	0.03640	55
Ca	422.7	0.49000	–
Fe	272	0.00770	380
K	766.7	1.94000	2.7
Na	589.2	0.52500	70
Si	251.5	0.00210	48
Ti	363.65	0.08730	1
Mg	285.2	0.03200	6000
O[2]	558	2.0E–02	1000
H_2O^+ [3]	654	0.00650	100

[1]Cageao et al. (1997), [2]Bhardwaj and Raghuram (2012) and [3]Michael et al. (1990)

searched for other, as-yet-undetected gases of both lunar and extra-lunar origin. LADEE was also to determine whether dust is present in the lunar exosphere, and reveal the processes that contribute to its sources and variability. The Ultraviolet-Visible Spectrometer (UVS) is one of three science instruments on board LADEE. This paper describes the science background, measurement objectives, design, performance, and operations of the UVS instrument.

1.1 Lunar Exosphere: Theory and Observations

Until now the tenuous lunar exosphere has been largely unexplored. After the Apollo program and ground-based observing campaigns, nine constituents of the lunar atmosphere have been positively identified: He, Ar, Rn, CH_4, N_2, CO, CO_2, Na, and K (Stern 1999). Argon and Helium are thought to be the main constituents of the exosphere. Sodium and Potassium have been observed in spite of their low abundance due to their strong spectral signatures (e.g., Sprague et al. 1992 and Potter et al. 2000). More recently, observations of sodium at the moon were made by the SELENE spacecraft (Kagitani et al. 2010), although these observations were limited to the night-side hemisphere of the Moon. There are many more species that are expected to exist in the lunar atmosphere that have not yet been confirmed, or lower limits have been established (e.g., Stern et al. 1997; Flynn and Stern 1996; Sarantos et al. 2012). The spatial and temporal variability of the lunar exosphere is not well understood, including the sources, release mechanisms, loss processes, and atmosphere/surface interactions. Models exist to probe these relationships (e.g., Hodges 1980; Sarantos et al. 2012), but there are insufficient data on lunar exospheric variability for validating these models.

Table 1 describes the known and suspected lunar exospheric species (modified from Stern 1999) that the UVS instrument addressed. Previously known species were measured via the Apollo 17 Lunar Atmospheric Composition Experiment (LACE) or via ground-based spectrometry. Those species not previously measured are approximate near-surface upper limits based on optical/UV remote sensing (Stern 1999).

There are multiple sources contributing to the lunar exosphere, including the solar wind, the regolith sputtering products, levitated dust, meteoritic and comet input, and outgassing from the lunar interior. These sources are the reservoirs that supply the constituents. However, the exospheric abundance, spatial distribution, and temporal variations are also de-

termined by the release mechanisms, surface interactions, and loss processes. Sputtering, photon-stimulated desorption (PSD), impact vaporization, and outgassing are four processes that can release particles into the lunar exosphere with different energy distributions at release. The height distribution of species in the lunar exosphere varies from species to species, depending on mass and the distribution of release energy. For all elements, density decreases with increasing altitude. However, the constituents typically have ballistic hop heights in the hundreds of km range (e.g., Crider and Vondrak 2000). Species that make up the lunar exosphere are thus prevalent at 50 km, the altitude the LADEE SC generally maintained over the sunrise terminator, and will have increasing concentration with decreasing altitude.

Sodium and potassium have already been observed in the lunar exosphere through ground-based observing campaigns and, for sodium, the SELENE spacecraft. Na and K are both volatiles, and are easily ejected from the lunar regolith due to their low binding energies. However, there are several possible processes capable of releasing these regolith constituents into the exosphere, and the relationship between these mechanisms is controversial (Sarantos et al. 2008). PSD has been shown to better explain the distribution in the sodium and potassium lunar exosphere (Madey et al. 1998; Sarantos et al. 2010). However, a correlation is observed between incident ion flux and the abundance of sodium; in addition, the sodium exosphere has been observed to increase in density during meteor showers (Matta et al. 2009). The history of observations and the synergy of contemporaneous orbital and Earth-based observations of Na and K will enable a better understanding of the release mechanisms.

Physical sputtering plays a role in release of other regolith-derived components of the exosphere (Si, Al, Fe, Mg, Ca, O, Ti). Abundances of regolith species differing from stoichiometry may be indicative of the ion sputtering process that ejects the species or subsequent interactions. Impact vaporization also occurs on the Moon, presumably adding meteoric material and regolith material to the lunar exosphere.

Two instruments on LADEE contributed to measurements of the gaseous exosphere. In addition to UVS and the species it can measure (Table 1), the LADEE Neutral Mass Spectrometer (NMS) measured a number of neutral gases and ions which UVS could not detect, including a number of noble gases (e.g., He, Ne, and Ar), as well as measuring some gases and ions UVS could measure (e.g., Na, K, and OH) (Mahaffey et al. 2014). Thus the UVS and NMS instruments were very complimentary.

1.2 Lunar Dust: Theory and Observations

The dust environment of the Moon has remained a controversial issue since the Apollo era. Visual observations and photographic images from the Apollo command modules, and images from the Clementine mission have been used to indicate the presence of dust at high altitudes above the lunar surface (Glenar et al. 2011). Most recently, observations with the Lunar Reconnaissance Orbiter star trackers and the Lyman-Alpha Mapping Project (LAMP) spectrograph have continued the search for lunar exospheric dust (Feldman et al. 2014). There are also in situ and remote sensing observations on the lunar surface that indicate dusty plasma processes are responsible for the mobilization and transport of lunar soil.

Television cameras on Surveyors 5, 6, and 7 gave the first indication of dust transport on the airless surface of the Moon (Criswell 1973; Rennilson and Criswell 1974). Images taken of the western horizon shortly after sunset showed a distinct glow just above the lunar horizon that was dubbed horizon glow (HG). This light was interpreted to be forward-scattered sunlight from a cloud of dust particles <1 m above the surface near the terminator. The HG had a horizontal extent of about 3 degrees on each side of the direction to the Sun. Assuming

that the observed signal is dominated by diffraction of sunlight, this horizontal extent corresponds to spheres of radius $\sim$5 μm (Rennilson and Criswell 1974). The astrophotometer on the Lunokhod-2 rover also reported excess brightness, most likely due to HG (Severny et al. 1975).

Apollo 17 crew reported the appearance of bright streamers with fast temporal brightness changes (seconds to minutes) extending in excess of 100 km above the lunar surface. McCoy and Criswell (1974) argued for the existence of a significant population of lunar particles scattering the solar light. The rough photometric estimates indicated $\sim$0.1 μm sized grains. These drawings were analyzed again (Zook and McCoy 1991) and most of the earlier conclusions were verified. This study also estimated the scale height (H) of this "dusty-exosphere" to be $H \sim 10$ km, and suggested that dust levitation could be observed using ground based telescopes. Recent theoretical models suggest that these observations could result from particles lofted from the lunar surface by electrostatic forces (Stubbs et al. 2006). Images of the lunar limb taken by the star-tracker camera of the Clementine spacecraft also showed a faint glow along the lunar surface, similar to the sketches of the Apollo 17 astronauts (Zook and McCoy 1991). The interpretation of these images was complicated by the presence of the scattered light from zodiacal dust particles as well as Earthshine. Analysis by Glenar et al. (2011) concluded that excess light could be explained by more typical sources, including Earthshine and internal camera scatter and thus there was no conclusive evidence for lunar HG resulting from exospheric dust.

The Lunar Ejecta and Meteorites (LEAM) Experiment provided the only in situ dust measurement of the lunar surface to date. LEAM was deployed by the Apollo 17 astronauts and started measurements after the return of the landing module; it continued to make observations for about 3 years. LEAM registered an unexpected population of slow-moving, highly charged lunar dust particles. A subsequent experimental study using the LEAM spare showed that the observations were consistent with the detection of sunrise/sunset-triggered levitation and transport of slow moving ($v < 100$ m/s), highly charged dust grains. LEAM measurements indicated grain radii on the order of hundreds of microns. Though these observations remained unexplained, they are thought to indicate that the undetected smaller grains could be lofted to high altitudes.

While recent emphasis has been on electrostatic lofting of dust to high altitudes, some fraction of the total dust will also include ejecta from meteoroid impacts. The exact fraction of electrostatic vs. ejecta dust at 50 km is currently unknown. However, analysis of the near-surface Surveyor images indicate that the amount of dust electrically levitated at the terminator is about 10^7 times that expected from dusty meteoroid ejecta (Criswell 1973). Both electrostatically-lofted dust and secondary impact ejecta originate from the surface. On LADEE two instruments will address lofted dust, the UVS instrument and the Lunar Dust Experiment (LDEX). LDEX is an in-situ instrument which measures the charge generated by dust grain impacts within the instrument (Horanyi et al. 2014).

1.3 LADEE and UVS Objectives

The LADEE mission was intended to explore the tenuous lunar exospheric species and dust above the Moon's surface. To this end the mission had two high-level objectives:

- LADEE Objective 1: Determine the composition of the lunar atmosphere and investigate the processes that control its distribution and variability, including sources, sinks, and surface interactions
- LADEE Objective 2: Characterize the lunar exospheric dust environment and measure any spatial and temporal variability and their effects on the lunar atmosphere

The UVS instrument supported both of these mission goals, as it was capable of observing emission by exospheric gases as well as the optical scattering or extinction by exospheric dust. The UVS baseline measurement requirements were:

- Detect resonance scattering emissions of Na, K in the lunar atmosphere with signal-to-noise ratio (SNR) of 5 or better over a single orbit of the LADEE spacecraft. The temporal scales covered shall range from 12 hours to 1 month. The spatial coverage shall be sufficient to resolve variations in Na and K within $\pm 20°$ of the terminator regions of the Moon.
- Detect resonance scattering emissions, or establish new upper limits for these emissions, with SNR of 5 or better, for the following species over the course of a 100-day mission: Mg, Al, Si, Ti, Fe, and Ca.
- Search for emissions from other, as-yet undetected species not included in the above list, with a SNR of 1 or better over the course of a 100-day mission.
- Perform solar occultation measurements to detect suspended dust particles over an altitude range of 1.5 to 50 km.
- Perform limb sounding measurements to detect reverse or forward scattered sunlight by suspended dust at 50 km or less, at a minimum column density of 10^{-4}/cc.

These measurement requirements were verified prior to flight using laboratory calibrations (Sect. 3) and analysis (e.g. Stubbs et al. 2010 and Sarantos et al. 2012). Given the pre-launch understanding of the exosphere and possible dust populations, and in reaction to realities in flight, operations were developed pre- and post-launch which allowed for a variety of observation geometries to address each of these measurement requirements (Sect. 4).

2 The Ultraviolet and Visible Spectrometer

2.1 Introduction

The UVS instrument consists of several components integrated into a single instrument. These components include a spectrometer with two foreoptics, a limb telescope and solar viewing optic, optical fibers, integrated mechanical/thermal structure and telescope aperture door. The UVS instrument was mounted atop the LADEE SC bus (Fig. 1). These components and the integrated instrument are described below.

2.2 Spectrometer Design

The spectrometer is the "next-generation" design of the Lunar CRater Observation and Sensing Satellite (LCROSS) Visible SPectrometer (VSP) (Ennico et al. 2012). The mechanical components are virtually identical with the VSP, with the only exceptions being mounting features for the integrated circuit boards. The spectrometer is a symmetric f/4 crossed Czerny-Turner spectrometer with a 1 inch aperture (Fig. 2). The first spectrometer mirror is spherical in figure, while the oversized camera mirror is toric. The toric figure of the camera mirror allows for a more efficient collection of light from the astigmatic spectrometer, with the spectral image slightly underfilling the 1.4 mm active height of the CCD detector. The 230–810 nm spectrum from the slit is imaged onto a 1044×64 (1024×58 active) pixel Hamamatsu S7031-1006S CCD detector array with integrated thermoelectric cooler (TEC). Each column of pixels is binned within the CCD, delivering a 1×1044 pixel spectrum to the electronics for packaging. The spectrometer contains no moving parts.

Fig. 1 *Top Panel*: The UVS
instrument installed atop the
LADEE SC. *Bottom Panel*: View
of the UVS instrument from
above

At a top level, the LADEE UVS electronics consisted of a few functional blocks (Fig. 3)
distributed across three printed wiring assemblies. A power supply board takes spacecraft
power (28VDC nominal) and converts it to the variety of voltages needed by the remain-
der of the electronics. A radiation-hard Actel radiation-tolerant (RTAX) 2000S field pro-
grammable gate array (FPGA) provides the timing and triggering needed by the instrument,
as well as an embedded 8051 microcontroller. The microcontroller code was contained in
and executed from an external $32k \times 8$ programmable read-only memory (PROM). Internal
FPGA Random-access memory (RAM) was utilized for both microcontroller data, which
was Error Detection And Correction (EDAC)-protected, and a spectral data First-In First-
Out (FIFO). The microcontroller provides the universal asynchronous receiver/transmitter
(UART) for the instrument's RS-422 serial interface, as well as the logic for receiving com-
mands from the spacecraft and presenting science data over the serial port. The FPGA feeds
a bank of MOSFET (metal–oxide–semiconductor field-effect transistor) drivers that form

Fig. 2 Shown is the UVS spectrometer optical layout with ray trace
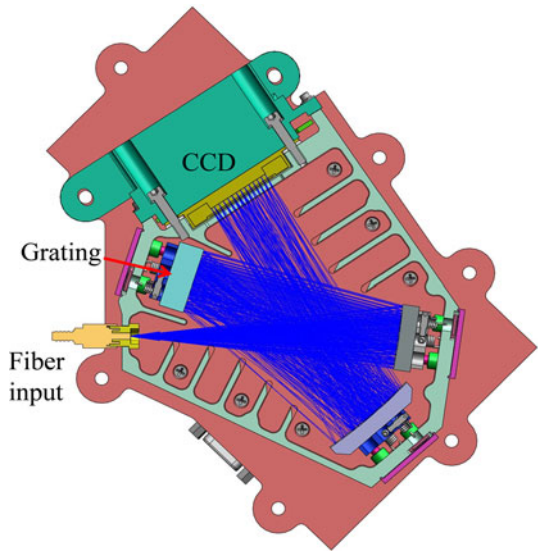
**Fig. 3** Shown is the UVS electronics block diagram with key components and interfaces
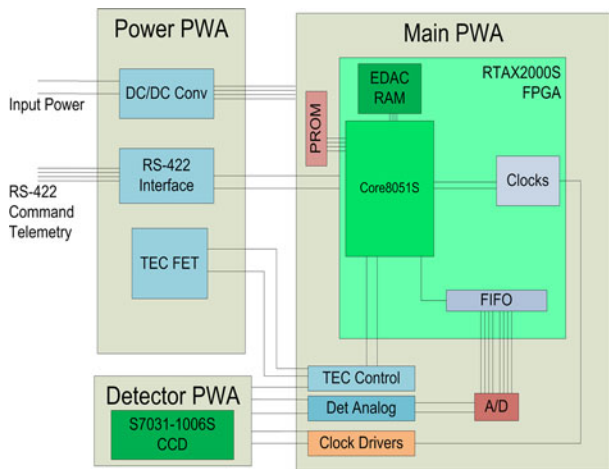
the clocks needed by the CCD detector. Analog sensor data is conditioned and digitized by a 16-bit 333 MHz A/D. The CCD detector temperature is controlled by a built-in single-stage TEC configured to provide cooling only. The detector temperature is monitored by a thermistor integrated within the CCD package. A proportional-integral-derivative controller (PID) loop implemented in the embedded 8051 microcontroller provides the necessary control of the PID loop, regulating the temperature of the detector to $+/-0.1\,°C$. The UVS electronics also provide over-current protection for the TEC, as well as monitors for TEC drive current and the temperature of the hot side of the TEC. The UVS telemetry data contains the TEC temperatures and drive currents. This design allowed for the reuse of >90 % of LCROSS's VSP FPGA and microcontroller code.

The spectrometer's power varies from 11.2 W to 17 W when the TEC is operated and can reach the peak power consumption of 23.6 W for a short period of time when the spectrometer reaches the temperature set point (typically $<-25\,°C$) of its sensor or when the TEC

Fig. 4 Shown are the optical/mechanical layouts for the (**A**) UVS Limb Telescope and (**B**) the UVS Solar Viewer
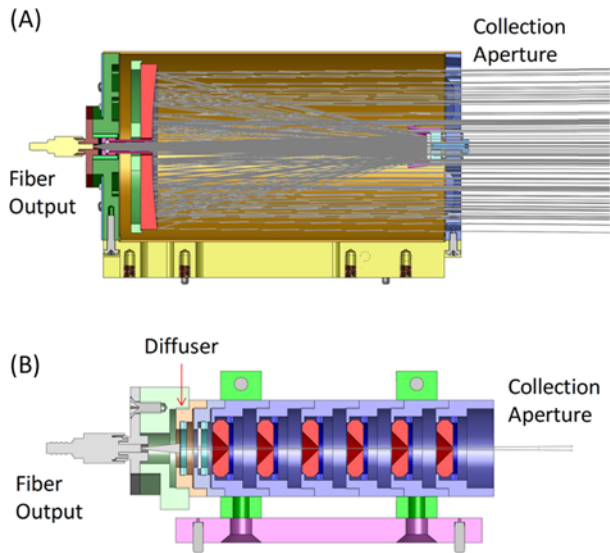

reaches its maximum cooling capacity. Spectrometer power consumption is always limited by the UVS power supply board and does not exceed 23.6 W. Thus, if the cooling capacity of TEC is exceed for any particular temperature set point, detector temperatures will drift as the spectrometer warms. If the spectrometer temperature reaches its maximum operable temperature, the spectrometer would be turned off. While in flight the detector temperatures were seen to drift toward the end of activities, the instrument never reached peak operating temperatures and thus was not turned off.

2.3 Telescope and Solar Viewer Design

An approximately 45-cm length, 300-micron core-diameter, bifurcated glass optical fiber attaches the spectrometer to both the telescope and solar viewer fore-optics. Two fibers are contained in this one fiber assembly; they vertically overlap one another at the spectrometer slit but separate to feed into the individual fore-optics. Light is collected from a specific optic by operational constraints: only one optic is illuminated during an observational period. These two fore-optics, the limb telescope and solar viewer, are separated by an angle of 12.6 degrees. This angle was chosen to minimize SC attitude maneuvers while maintaining one of the two fore-optics pointing to dark sky or dark lunar surface.

2.3.1 Telescope

The telescope, a catadioptric design with all spherical surfaces (concave primary, convex secondary, plano-convex field lens), presents a 3 inch aperture and a 1 degree field-of-view (Fig. 4). The telescope optical coatings are optimized for the 250–800 nm wavelength range. Baffles are incorporated at the secondary mirror mount and primary mirror aperture, and the interior of the telescope tube is bead-blasted to minimize stray light. Mass constraints did not allow for an extended sunshade. However, the secondary mirror spider mounts were beveled away from the entrance aperture by 10° to help minimize scatter into the telescope from surface reflected sunlight (see Sect. 3.4). All interior surfaces are black anodized. A rail is
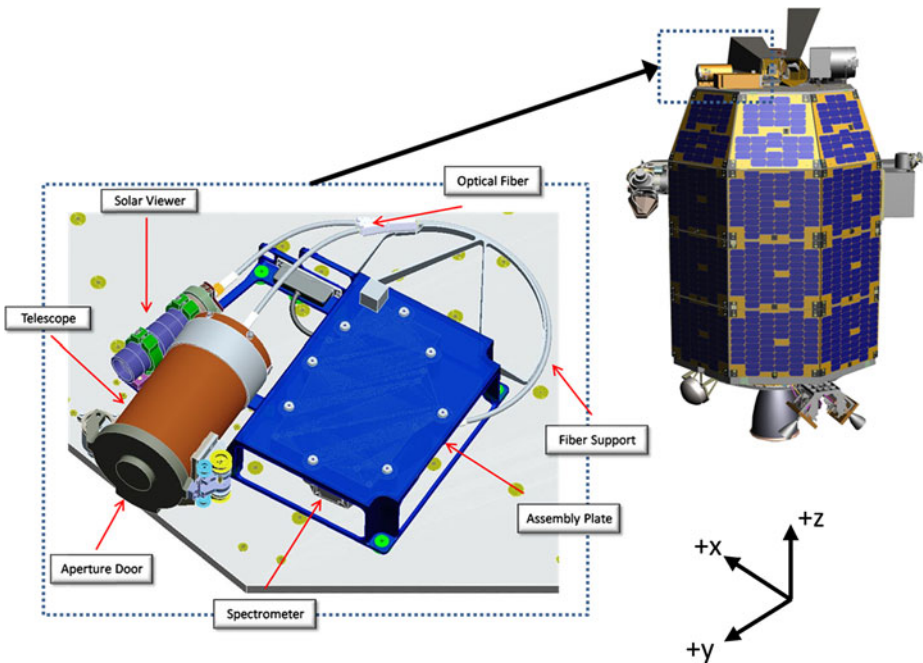
Fig. 5 The UVS instrument assembly is mounted as one component on the radiator deck at the top of the LADEE spacecraft

mounted on the underside of the telescope and attaches the telescope to the instrument assembly plate. Finally, the telescope has an aperture door assembly (ADM) composed of a delrin (polyoxymethylene) cover, a TiNi pinpuller and a locking hinge to protect the telescope optics against contamination sources during the initial mission phases. The ADM was deployed during commissioning prior to the science operations.

2.3.2 Solar Viewer

The solar viewer is a series of six interlocking aperture supports with six concentric aperture disks forming a 1 degree field-of-view (Fig. 4). A ground fused silica diffuser is held in a separate mount and attached to the back of the mount series before the solar viewer connects to the fiber. The diffuser serves two purposes: it attenuates the solar irradiance to a level that can be detected by the spectrometer without saturation and provides an extended spot of light to fill all of the optical modes of the fiber. The transmission of the diffusor varied no more than 2 % across the UVS wavelength range. The entire series of supports is mounted to a rail and held in place by two ring-shaped clamps. The rail mounts the solar viewer to the instrument assembly plate.

2.4 Integrated Instrument Design

The LADEE UVS consists of three components and their supporting electrical and mechanical harnesses as shown in Fig. 5. The UVS is integrated into the spacecraft on the top radiator deck (Fig. 1).
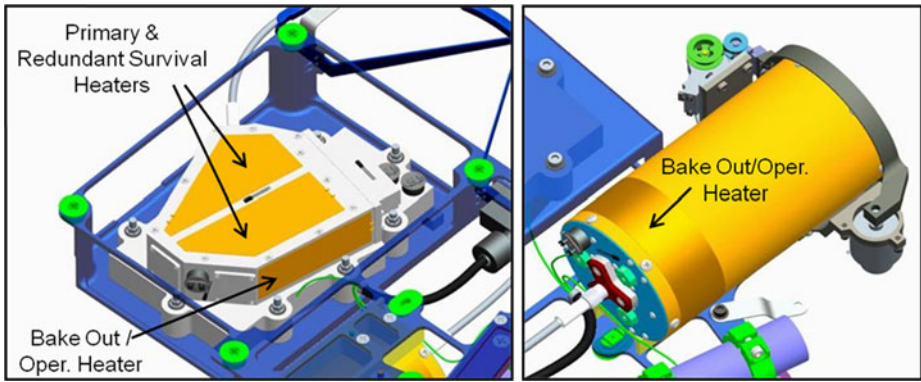
Fig. 6 The spectrometer survival and operational heaters are mounted to the spectrometer housing and positioned around the internal optics (*left*). The telescope operational heater wraps around the back end of the telescope tube surrounding the primary mirror inside the telescope (*right*)

2.4.1 Instrument Design

The UVS thermal management system was designed to keep the instrument within its operational ($-20\,°C$ to $+45\,°C$) and survival boundaries ($-30\,°C$ to $+60\,°C$) throughout all of the mission phases. The system consists of bake-out, operational, and survival heaters, thermostats, temperature sensors, Multi-Layer Insolation (MLI) and radiative surfaces (Fig. 6). To minimize dependence between the spacecraft and UVS thermal designs, UVS was design to be thermally isolated from the spacecraft. To thermally isolate the UVS from the spacecraft, each mounting fastener is surrounded by a low thermal conductivity washer (G-10 material) and the instrument wrapped in MLI.

2.4.2 Spectrometer Thermal Management

A challenge for the design was the thermal maintenance of the spectrometer's thermoelectric cooler (TEC), which cools the CCD detector. The TEC can cool the detector to between 10 and $50\,°C$ colder than the spectrometer heat sink. Additionally, during operation, heat is generated at the location of the TEC as well as on the two electronics boards. This heat flows to the bottom cover of the spectrometer, which is also the mounting surface.

To effectively cool the instrument, the spectrometer is inverted and mounted to the bottom of the UVS assembly structure. The opposite side of this assembly area, which faces out from the SC, is coated with a silverized tape and acts the instrument's thermal radiator (visible in Fig. 1, bottom panel). The spectrometer bottom cover is thermally coupled to the instrument thermal radiator with 8 bolts and a high thermal conductance gasket (made of Cho-Therm 1671). Additionally, the telescope and solar viewer are also mounted to the side of the assembly structure and thermally coupled with Cho-Therm 1671.

The primary and redundant survival heaters kept the UVS above its survival temperature limit during times of non-operation, such as transfer phase, non-UVS science orbits, or safe-mode. The survival heater is controlled by an independent thermostat and is designed to keep the instrument above $-30\,°C$. The bake-out/operational heaters on the spectrometer were used to warm UVS for bake-out (contamination control) and used to warm to operational turn-on temperatures at the beginning of an operational orbit, when necessary. Bake-out/operational heaters are controlled by flight software, based on temperatures recorded

by the UVS temperature sensors. Bake-outs were performed shortly after launch (4 days after, >12 hours with the entire instrument over 40 °C), during cruise (>20 days with the instrument over 40 °C), and shortly after lunar insertion (>24 hours with the instrument over 40 °C). These bake-outs were also used to help anneal radiation damage on the CCD (formation of hot pixels and increase in dark current) which occurred primarily as the SC passed through the Van-Allan radiation belts during the missions Earth-to-Moon cruise phase. To further mitigate contamination, beginning approximately 5 days after launch and through cruise UVS had a requirement to be kept at least 10 °C warmer than the spacecraft surfaces in the immediate vicinity of UVS. These surfaces were typically less than 20 °C. However, because there was sufficient power, it was decided to maintain the UVS in a bake-out state for the majority of the cruise duration.

3 Instrument Characterization and Calibration

A number of pre-flight and in-flight tests were conducted to characterize and calibrate the UVS instrument. Obviously, in most cases in-flight characterization or calibration should supersede pre-flight results. This section summarizes these tests and their results. Calibration work is on-going with new calibration to be delivered to PDS as part of a second data products delivery schedule for Summer 2015.

In each spectrum, there are blank pixels (pixels 0–3 and 1040–1043 using zero index notation) and bevel pixels (pixels 4–9 and 1034–1039). The blank pixels are dark pixels that are optically inactive. The bevel pixels are pixels that are optically active but not entirely back thinned. Pixels 10–1033 represent the entire optically active range. Including in each spectrum is an inherent instrument electronics voltage bias and thermal (dark) current. This voltage bias, a non-uniform offset from zero across the detector, is measured using the short (10 msec or less) integration times and coldest detector temperatures where thermal noise is negligible (Sect. 3.3). Thermal current is measured using a range of "dark calibrations" performed both pre- and post-launch.

Analyzing a spectrum is a multi-step process of removing the bias and instrument thermal noise and cosmic ray effects. On the ground individual spectra are "scrubbed" for cosmic rays using a histogram to identify the pixels with counts significantly greater (typically >5-sigma) than the running median in time. These events are flagged and not included in later analysis. Following this cosmic-ray scrub, a voltage bias spectrum is subtracted. Using this product, then the median of the last four blank pixels, which give a good measure of the instrument dark current at the time of measurement, is subtracted. The first four have a spike inherent from the spectrometer electronics and are therefore not used. Lastly, grating second-order effects are subtracted. A radiance calibration is then applied to these spectra to convert the digital number (DN) to radiance units (Sect. 3.5). Specifics of instrument characterization and calibration are discussed in the following section.

3.1 Alignment and Pointing

Nominal UVS in-flight operations required careful pointing of the limb viewing telescope and solar viewer. Both the telescope and solar viewer had to be able to point to with 0.2 deg of the intended target and have a pointing knowledge of 0.15 deg. This relatively tight control would allow for the UVS telescope to point to within approximately 3–5 km of the surface without unintentional viewing of the surface, and allow the solar viewer to track the sun (assumed to have an angular diameter of 0.52 deg) over the course of an entire solar occultation activity.

3.1.1 Telescope Boresight—In Flight Calibration

To measure the relative shift in the boresight alignment after launch, the UVS telescope's FOV was swept across the lit lunar limb several times, with a low angular velocity. The slews covered the limb crossing along two orthogonal axes in the UVS telescope's field of view with one done about the spacecraft Z-axis and the other about a vector in the spacecraft X–Y plane. Based on the spacecraft position during this activity and the spectral response of the instrument, the position of the limb crossing was determined and used to calibrate the instrument alignment to the spacecraft frame of reference. This activity was done about both the X and Y axis.

3.1.2 Solar Viewer Boresight—In Flight Calibration

For the solar viewer boresight calibration, the spacecraft performed a series of slews to enable UVS solar viewer crossings of the sun, similar to the telescope boresight calibration, except these slews cross over the entire disk of the sun (as opposed to the partial disk of the moon). Note that the slews were done back and forth along each axis as numbered in the image below. Based on the light curve produced from the instrument during this activity and the corresponding spacecraft position, the vector of the limb was determined and used to calibrate the instrument alignment to the spacecraft frame of reference.

3.2 Wavelength and Instrument Line Profile Calibrations

3.2.1 Ground Wavelength Calibration

A Mercury-Argon (HgAr) lamp spectrum was used to perform lab-based wavelength calibrations. 21-lines in the lamp spectrum were used to fit a third order polynomial, correlating wavelength to pixel number. The HgAr lamp was used frequently to trend the wavelength shifts and calibrate the instrument throughout flight I&T at ARC. The polynomial fit was updated during the payload I&T program before and after any environmental testing was performed. Errors in the fits are $+/-0.59$ nm. During environmental testing, the instrument demonstrated a shift of up to 3 pixels or 1.8 nm as a result of qualification level vibration tests.

3.2.2 In Flight Wavelength Calibration

During early-mission instrument commissioning, data from the solar viewer boresight calibration activity was used to calibrate the wavelength position for each pixel, similar to the method using the HgAr lamp on the ground. First, a Gaussian response function was fitted to the HgAr lines from the ground data. This response function was convoluted with a standard, high resolution solar spectrum standard from Harvard-Smithsonian Center for Astrophysics (CfA) (Chance and Kurucz 2010) to produce and estimate of the spectrum that UVS should record when viewing the sun. Using actual spectra from the solar viewer boresight calibration with the solar disk in the FOV, the UVS measured solar spectrum was compared to the convolved CfA standard solar spectrum to determine the wavelength value for each pixel, based on line positions (Table 2). The pre and post launch calibrated wavelengths shifted by approximately 1 nm as, shown in the Table 2.

Table 2 The in-flight wavelength calibration used standard solar lines convolved with the UVS spectral response to compare to actual spectra from the solar viewer boresight calibration

Data Recorded November 1, 2013					
Pixel	Measured λ (nm)	Δλ From Pre-Flight	Pixel	Measured λ (nm)	Δλ From Pre-Flight
77	274.276	0.896	278	393.306	0.834
85	279.638	0.832	284	396.801	0.839
94	284.994	0.823	342	430.480	0.888
130	305.770	1.392	439	486.376	0.973
135	309.323	0.798	493	517.275	1.008
218	358.228	0.801	739	656.299	0.822
261	382.806	1.407	991	794.681	1.124

Cubic Fit: $\lambda \, [\text{nm}] = a_0 + a_1 x + a_2 x^2 + a_3 x^3$; $x = $ pixel number from [0:1023]

Intercept	2.28659E+02
First Coefficient	5.99468E−01
Second Coefficient	−2.75462E−05
Third Coefficient	−1.00518E−09
Regression Fit	0.9999976

### 3.2.3 Instrument Line Profile Calibration

The instrument line profile was measured in-flight by comparing observations of the solar spectrum to modeled solar spectra (Chance and Kurucz 2010) at various degrees of spectral resolution. By fitting measured solar Fraunhofer lines (width and depth) at variable spectral resolutions the instrument line profile can be estimated. Figure 7 shows line width in terms of standard deviation (sigma) and a fit to the data.

3.3 Dark and Bias Calibrations

To calibrate for the spectrometer CCD dark current, the instrument's response was characterized for various TEC set-points and integration times. This calibration was then used to predict the dark current for each spectrum and to remove the dark current from spectra before applying any calibrations.

Dark calibrations recorded spectra at the following TEC set points: −30 °C, −25 °C, −20 °C, −15 °C and −5 °C and at each TEC set-point, spectra were recorded with the following integration times: 8 ms, 100 ms, 500 ms, 1 s, 5 s, 10 s, 30 s, and 60 s. This activity occurred both on the ground and in orbit, and these data sets are used to monitor and trend the dark response of the instrument over the duration of the mission. In-flight dark calibrations were performed periodically through the mission by pointing the telescope at the night-side of the moon during full moon (avoiding Earth-shine). These calibrations were very useful to identify and calibrate "hot pixels", i.e., pixels with higher than average dark current, typically the result of radiation damage. The 'bias' spectrum is the measure of the instrument's signal offset from zero. The bias spectrum was generated in flight using a set of 10 millisecond scans gathered during each dark calibration activity (Fig. 8).

Fig. 7 The instrument line profile width (standard deviation to a Gaussian fit) as a function of wavelength were derived from fits of flight data to modeled solar spectrum at various resolutions (see text)


$$y = 5.2343x^{-0.329}$$
$$R^2 = 0.8672$$
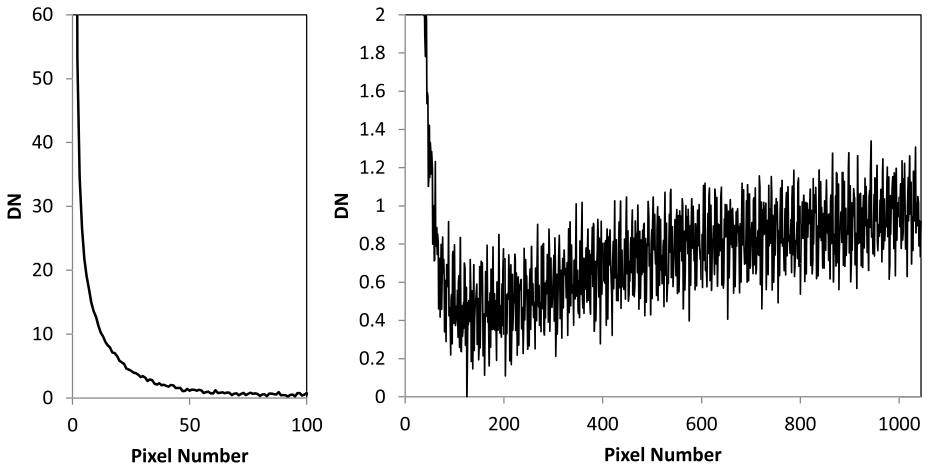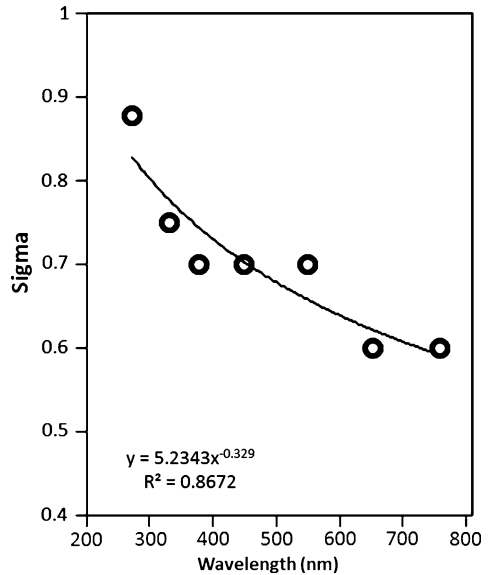
Fig. 8 Inherent in the instrument is an offset from zero called the instrument voltage bias. The instrument bias is a maximum at the smallest pixel numbers (*Left Panel*) and relatively flat at pixels beyond 75 (*Right Panel*)

3.4 Scattered Light

3.4.1 Ground Tests Performed to Characterize Instrument Response to Stray Light

Spectrometer Interior Stray Light Rejection   Stray light inside the spectrometer can result from grating shine or reflection off the CCD window. To measure this, the instrument underwent a series of tests to determine if there was any interior stray light and to characterize what stray light was found. For the test, a cover was made for the integrating sphere to interface with a series of edge filters and project light through the filter into the telescope's

Fig. 9 The measurement set-up for measuring instrument internal scattering (*top panel*) and an example the percent scatter for one of the filters (665 nm) (*bottom panel*)
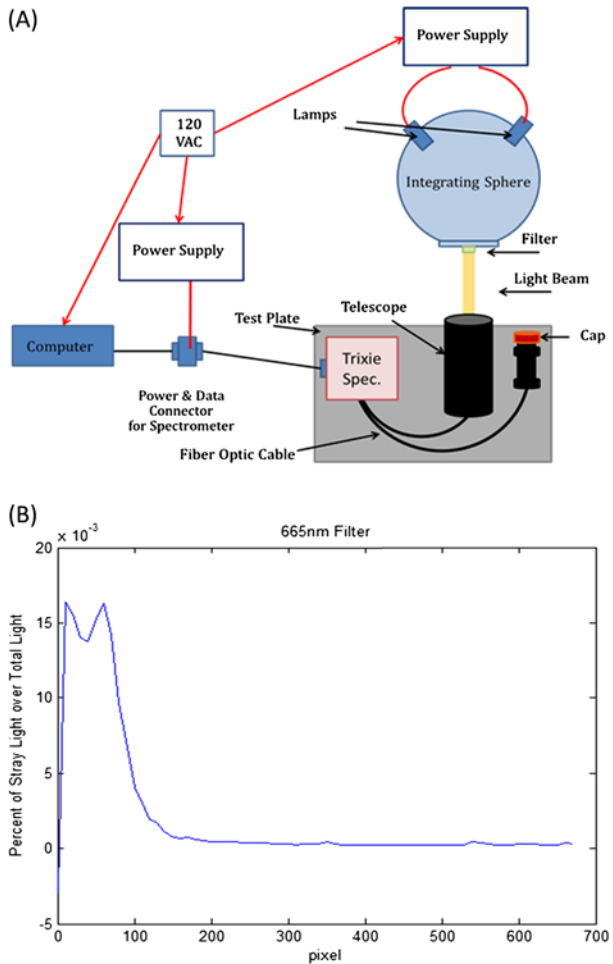

FOV (Fig. 9A). In the setup, a heat absorbing filter was used to remove any IR from the spectrum and the subsequent 610 nm, 630 nm, 665 nm and 695 nm filters were placed in front of the IR filter. For each of the four filters, spectra were recorded and subsequently dark-corrected, time-normalized and averaged over the number of samples recorded. Then, in 5-pixel increments, the integral was calculated for the reference data and the spectra using the 4 filters. No stray light was found to be higher than 0.02 % of the reference signal, with stray light being generally less than 0.0005 % across most of the detector. The maximum internal stray light occurs at the shortest wavelengths below 275 nm (pixel ~100) (Fig. 9B), however, this is partially due to the reference signal being low in that region, diminishing the dynamic range.

Off Axis Light Rejection   An off axis light rejection test was performed to gauge the telescope's acceptance of light outside of its FOV. For this test, the UVS instrument was set up on a test bench with a HeNe laser beside it. The laser was projected onto a target 263.2 cm away and the telescope was positioned so that the laser back reflection was in the FOV. From here, the laser point was stepped in 1.3 cm increments from the center of the telescope FOV

**Fig. 10** Shown are the two primary sources of stray light
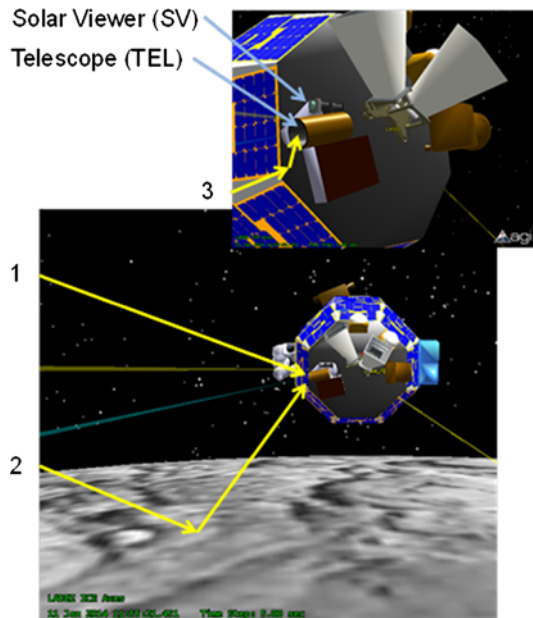
to 39.4 cm from the center, so that the angle of incident light varied from 0 to 9.4 degrees from telescope normal.

At each position, twenty spectra were recorded with an integration time that maximized SNR at that position. Following the test, the spectra from each location were averaged, time-normalized and dark-adjusted to give one representative spectrum per each location. Using pixels 710 to 712, which corresponds to 635.5 to 636.6 nm (the wavelengths that the laser covered), the integral of the laser response was calculated using the trapezoid rule on both the "in-FOV" spectra and the three "out-of-FOV" spectra. To determine the off axis rejection, each integral of the out-of-FOV data was divided by the integral of the in-FOV data. At angles greater than 1.5° from the center of the telescope FOV, the off axis light contribution was typically less than 3×10^{-4}.

3.4.2 Flight Measurements to Characterize Instrument Response to Stray Light

In flight, two sources of stray light have been identified (Fig. 10). The first is from direct sunlight impinging directly on the secondary mirror mount at the front of the UVS telescope or on the spacecraft upper deck (radiator) and then onto the mirror mount (rays 1 and 3). The second comes from sunlight reflected off the lunar surface and onto the mirror mount (ray 2). The geometry of the UVS operations were adjusted to minimize these sources of scattered light. While operating in "Limb" mode (see Sect. 5) lunar and solar scatter surface scatter into the telescope was determined by comparing total signal levels at a variety of surface and solar elongation angles. It was found that when the solar elongation angle was <90°, direct scatter into the telescope was prohibitive. For worst-case surface reflectance scatter the total rejection was between 2×10^{-4} and 3.3×10^{-4} at 634 nm, or about a factor of 1.6 times worse than measured in the lab. The discrepancy is due to the difference between the relatively small range of exposure angles in the lab versus what is seen while viewing the lunar limb over a fully illuminated surface. At ultraviolet wavelengths (<330 nm) the rejection is much better, with very little difference between spectra taken at local noon and

Fig. 11 The fraction of off-axis light scatter into the limb telescope and fit to the data
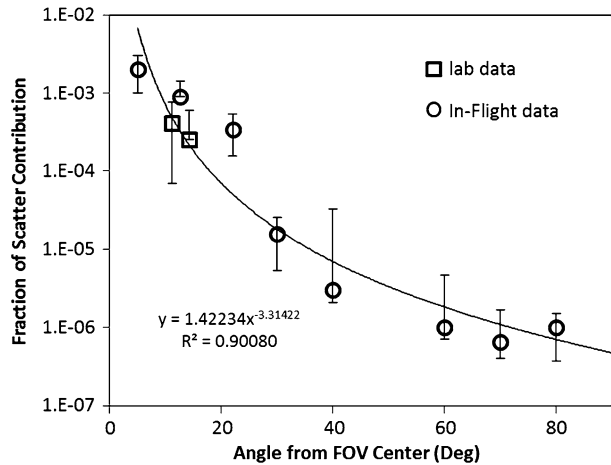
when the spacecraft is in lunar umbra with no scattering sources present. The off-axis response was determined at a range of angles by monitoring the amount of sunlight into the telescope while the telescope pointed off the sun. This data, along with lab measurements, are shown in Fig. 11. As mentioned, while in limb-view, in addition to the sun, the bright lunar surface was also a source of scattered light. As mentioned above, because the UVS activities were timed to keep the sun behind the instrument aperture (solar elongation angles >90), the lunar surface was most often the primary source of scattered light.

3.5 Radiometric Calibration

3.5.1 Radiometric Calibration on the Ground

UVS radiometric calibrations are based on data taken with an integrating sphere acquired from LabSphere. The sphere used for this calibration has both a tungsten-halogen and xenon light source that mix within the integrating sphere to provide uniform illumination at the output aperture over the UVS wavelength range (230.34–824.52 nm). The sphere has an independent NIST calibrated spectrometer to record the sphere's spectral output in units of radiance ($\mu W/sr/nm/cm^2$) which can then be compared to the UVS recorded spectra in digital number (DN; i.e. counts) to determine a DN/unit-radiance calibration. The data used to calculate the radiance calibration was taken during the instrument's last performance test prior to integration with the spacecraft on July 25, 2012.

To begin this process, both the UVS DN spectra and integrating sphere radiance spectra are dark-corrected by subtracting a recorded dark spectrum from each respective spectrometer at the time of the test. Using the dark-subtracted data, each sphere and UVS spectrum is normalized or divided by its respective integration time in seconds. The sphere-reference data is spline-fit to the UVS wavelength range, to match UVS. From here, the UVS spectrum is corrected for the spectrometer grating second order effects. Second order effects are from a small portion of the light at the fundamental frequency (250–415 nm) being projected onto the CCD at its second harmonic wavelength (500–830 nm). This correction was generated through a combination of analytical modeling of the detector quantum efficiency, the grating efficiency, the mirror reflectivity and the grating reflectivity, and from measurements of the second order peaks in MgAr line data. Finally, the UVS DN spectrum is divided by the
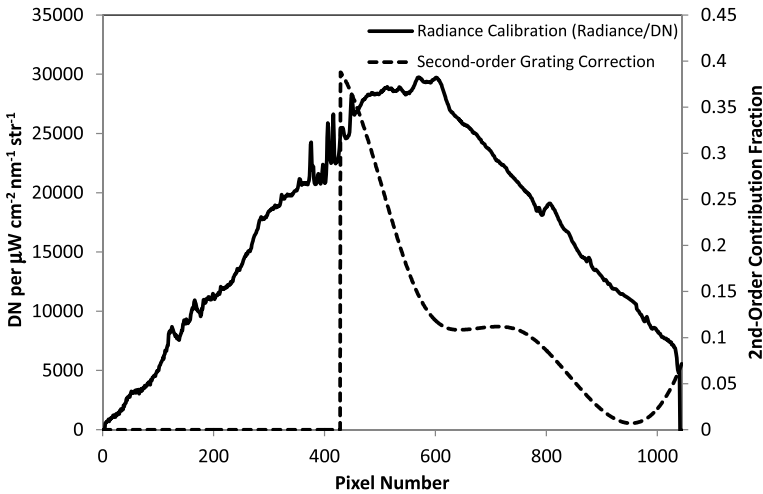
Fig. 12 The instrument radiance calibration (DN to radiance) and the fraction of grating second-order contribution

sphere radiance spectrum to determine a DN/μW/sr/cm^2/nm value for each UVS pixel. This calibration curve and the grating second order contribution is shown in Fig. 12.

In summary, the steps needed to apply the radiance calibration to any recorded UVS spectra from flight are:

1. Dark and bias correct the spectra
2. Normalize the spectra by integration time
3. Correct the spectra for second-order grating effects
4. Apply the radiance calibration

3.5.2 In Flight Radiometric Calibration

To verify radiometric response, UVS spectra of specific lunar surface locations were compared with measurements of the same locations from other missions. UVS activities were planned so that the spectra recorded would have the same incidence and emission angles as spectra from the Moon Mineralogy Mapper (M3) instrument on Chandrayaan-1, and the USGS RObotic Lunar Observatory (ROLO) measurements over the same areas on the lunar surface (work in progress).

Moon Mineralogy Mapper and Wide Angle Camera Comparison   Using STK, the geometry of the UVS activity was mapped to determine the incidence and emission angles to the lunar surface. The M3 and WAC data was then filtered for these angles over the same local lunar area and matched to the UVS data over the UVS spectral range. Figure 13 shows one area over which UVS, M3 and WAC data have been compared. Agreement is generally good, except between 500–650 nm. It is in this area that ROLO data will help improve the calibration.
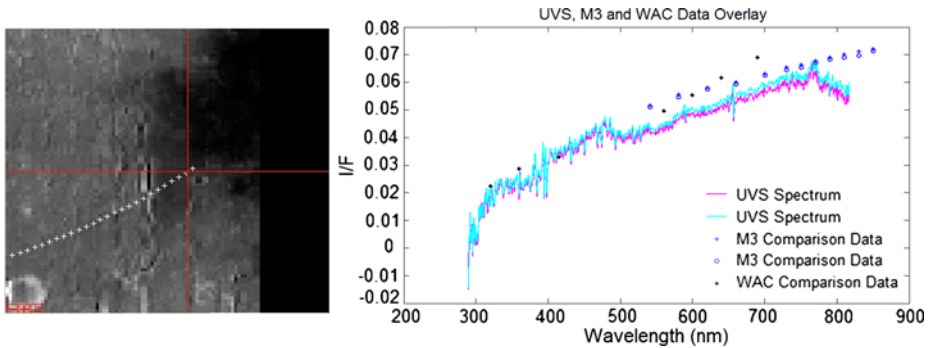
Fig. 13 The UVS spectral collections (+) were plotted over an M3 image of the same area to determine the overlap in measurements (*left panel*) and a preliminary comparison of M3 and WAC I/F for a single UVS nadir activity (*right panel*)

4 Mission Operations and Expected Results

4.1 Instrument Configuration

Although UVS provides a flexible command set and approximately 20 configuration settings, most were left in their default state during the LADEE mission. Four settings were used during flight:

1. Detector Temperature: the setpoint for the thermo-electric cooler that regulates the detector temperature. Typical values are $-30\,°C$ and $-25\,°C$.
2. Integration Time: how long to capture photons for a single spectrum. Typical values are 26 msec for solar occultation measurements and 2 sec for limb observations.
3. Streaming Mode Duration: How long to collect spectra before stopping and remaining idle. 20 minutes is a typical value.
4. Streaming Mode Period: The time interval between integration starts. This was normally set to 0 msec, causing the spectrometer to follow each integration immediately with another.

Of these, the first two are the most important and were varied frequently during the mission as the operations team improved its understanding of in-flight instrument performance.

4.2 Nominal Operations

While there are only four internal instrument settings, there are numerous combinations of observing geometries and durations called activity types. Each activity type has a primary science goal and can support other science activities, while each science goal can be supported by multiple activity types. For example, Na and K observations can be derived from spectra taken during "Limb" and "North-South" observation activities (see below). The following section summarizes the viewing geometry and sampling interval for each activity.

4.2.1 Limb Orbit

The limb activity is the principal activity for characterizing lunar exosphere gases and dust backscatter. In this activity, the UVS telescope is pointed by the spacecraft backward (anti-ram) and just off the moon's limb. These activities are timed so that the telescope points toward the lunar sunrise terminator, the sunset terminator, or toward lunar noon.
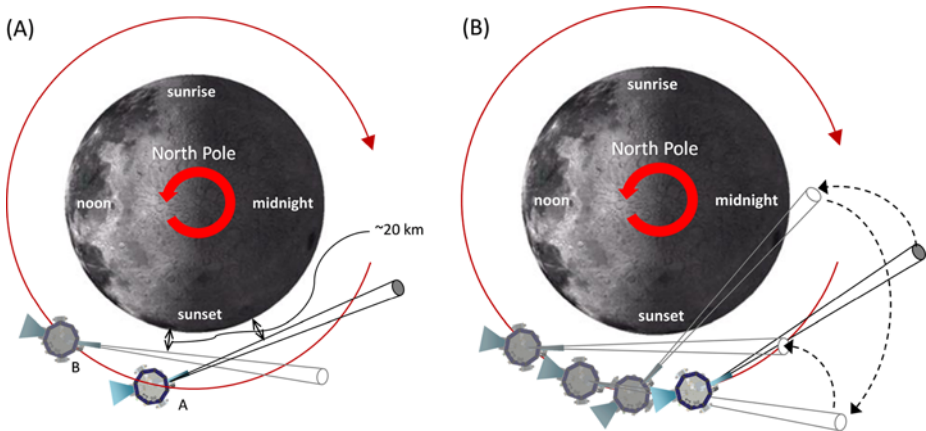
Fig. 14 Stare portion (**A**) and nod (**B**) components of a limb activity


Fig. 15 Positions of the telescope (*blue circle*) and solar viewer (*yellow circle*) fields of view during a limb stare
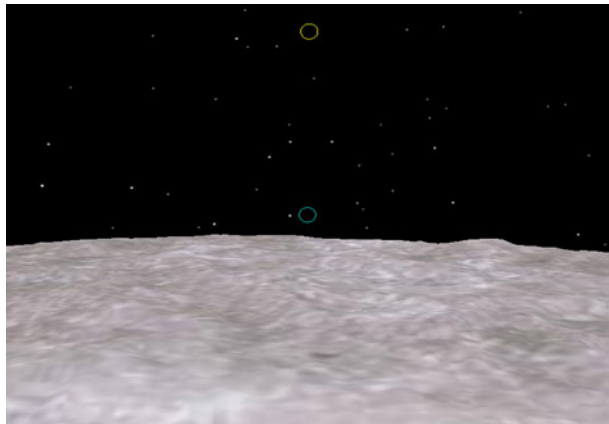
Instances of this activity used earlier in the mission consisted of "stares", where the telescope's field-of-view was held a constant attitude above the lunar reference sphere, and "nods", where the field-of-view was swept down to the surface, then up higher than a stare, then back to the stare altitude. Figure 14A shows LADEE at the beginning of a limb activity (A) and later at the end (B). At both times, the stare altitude is 20 km. Figure 14B illustrates the nod portion of a limb activity. Data collected during nods provides information about the concentration of gasses across different altitudes.

Figure 15 illustrates the sizes of the telescope field-of-view (blue) and the solar viewer field-of-view (yellow) and their positions during limb stares. Note that, although light always enters through both apertures, in this configuration, the solar viewer is far from lit surface and the solar viewer's diffusor rejects so much light that all but the brightest sources are negligible. The spectrometer is much more sensitive to light entering the telescope aperture, and metadata are provided with the spectra to indicate whether the Sun or Earth are in or near the telescope's field-of-view. While bright starts were monitored, they did not present a frequent enough problem to include in the metadata.

While all limb activities early in the mission contained nods, most nods were emitted them. This change was made initially for limb stares near noon to avoid higher levels of
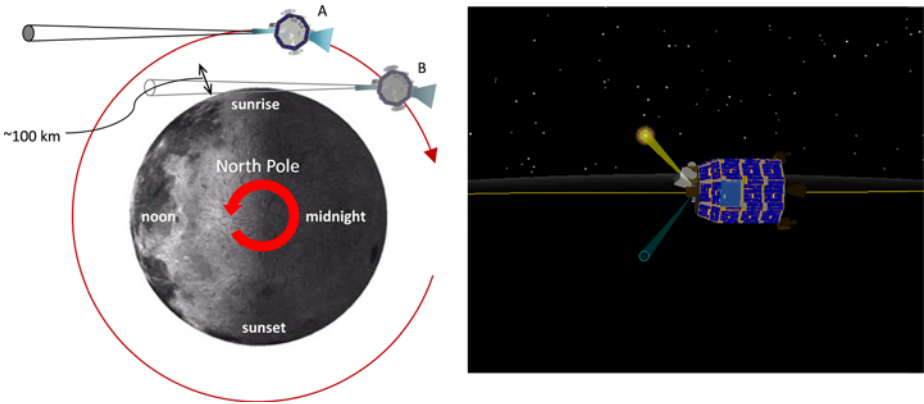
Fig. 16 Occultation activity observation geometry and SC perspective

stray light entering the telescope as the field-of-view neared the surface and subsequently for limb activities looking toward the terminators.

4.2.2 Occultation

The occultation activity allows for the characterization of the lunar dust and gases down to very low altitudes (Fig. 16, left panel). The activity is performed with the UVS viewing the sun through its solar viewer while the spacecraft crosses the lunar sunrise terminator (position A) and enters the shadow of the moon (i.e., sunset for the spacecraft at position B). The orientation of the spacecraft is held constant while it passes into the moon's shadow allowing the UVS to take measurements from a higher altitude down to the lunar surface.

Figure 16 also shows the relative positions of the solar viewer and telescope fields-of-view during an occultation (Fig. 16, right panel). Note that the telescope field-of-view is on the surface. The yellow line is the terminator with lit surface on the far side of the line and unlit terrain on the near side. Spectra collected before the telescope field-of-view is sufficiently past the terminator to avoid lit peaks may contain enough photons through the telescope to be relevant. Unfortunately, it was impractical from an operational standpoint to rotate the spacecraft about the solar viewer boresight enough to bring the telescope FOV off the surface.

4.2.3 North-South

The North-South activity is a variant of a limb activity where the UVS telescope field-of-view is pointed either north or south instead of backwards along the orbit track. Like a limb activity, the field-of-view is held a fixed altitude above the lunar reference sphere, and these activities also may contain nods. North-South activities are done to create a 3-D characterization of the lunar exosphere; in particular, to characterize the longitudinal and latitude variations in dust and gas species (Fig. 17). In this case, the spacecraft maintains a near constant attitude relative to the sun. The telescope field-of-view is steady above the limb although the solar viewer field-of-view moves around, remains off of the surface for the duration of these activities.

83

Fig. 17 SC perspective of a North-South activity
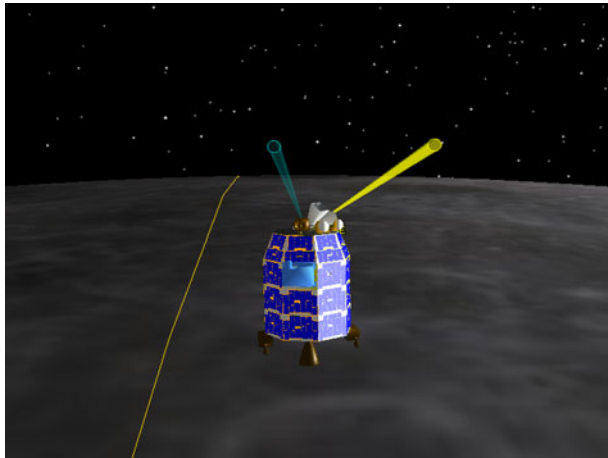
4.2.4 Sodium Tail

The sodium tail activity is a limb stare in the lunar night that makes measurements of the moon's sodium tail. The results will be compared with other similar science measurements made on other missions.

4.2.5 Forward Look

The Forward Look activity provides observations in a geometry which maximize signal from any dust that may be in the instrument FOV. Small dust grains tend to scatter most strongly in the forward direction (that is anti-sun, or near 180 degrees of phase angle relative to the light source). Forward scattering can be between 20 to $100\times$ greater than backscattering (0 degrees relative to the light source). The forward look geometry provides similar viewing conditions to what the Apollo astronauts had from orbit, as the command module came up on spacecraft sunrise (over the lunar sunset terminator). In normal spacecraft-ram limb observations, UVS takes measurements in the backscatter orientation over the sunset terminator. The Forward Look direction performs the same Limb observations, including nods, but with UVS pointed in the forward (ram) direction. These observations would provide maximum sensitivity to small, levitated dust particles at the sunset terminator. Also, measurement of both the forward and backscatter contribution from putative lofted dust will help provide constraints on particle size and shape.

4.2.6 Almost Occultation

Almost Occultation activities are a variant on occultations that hold the solar viewer's field-of-view slightly off of the sun while putting the telescope's field-of-view in the same position relative to the sun as it is during normal occultations. Figure 18 illustrates an Almost Occultation (compare this with Fig. 16B). Almost Occultations were performed to study the impact of stray light into the telescope on normal occultation measurements.
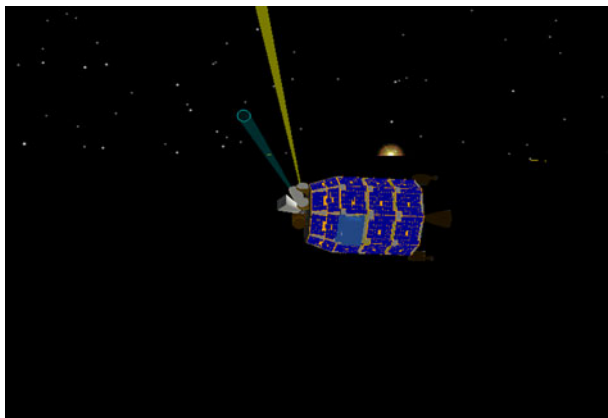
4.2.7 Almost Limb

Almost Limb activities use the telescope to search for dust close to the surface, complementing occultations which use the solar viewer for the same purpose. They are called Almost

Fig. 18 SC perspective of an Almost Occultation activity
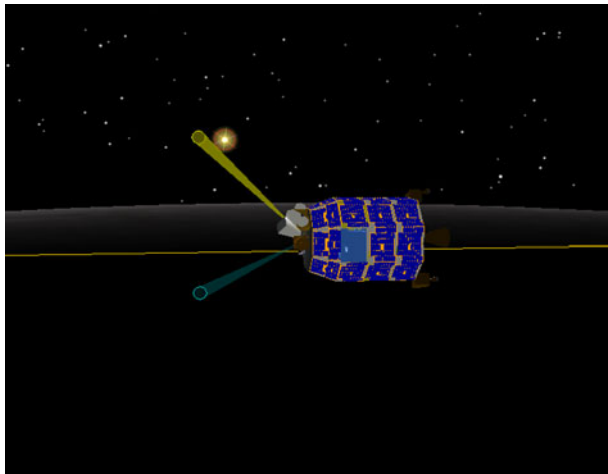
**Fig. 19** SC perspective of an Almost Limb activity

Limb activities because they place the telescope's field-of-view above the limb just after the spacecraft enters umbra like some limb activities. They are different, however, in that the spacecraft is held in a fixed (inertial) attitude and the telescope field-of-view moves with the sun, approaching and crossing the limb (effectively setting) shortly after the sun sets (Fig. 19). This is done to hold constant the contribution from Zodiacal Light, which is within the FOV as a background emission to any forward scattered light from low dust.

4.3 Instrument Planning and Real-Time Operations

Instrument operations and activity planning took place in the instrument operations center (IOC) located in building N240 at NASA Ames Research Center. In the IOC, the data from the spacecraft was displayed in telemetry pages whenever the spacecraft was in view and telemetry was streaming from the science operations center. Available telemetry included a good overview of the spacecraft as a whole—power, propulsion, communications, thermal, payloads, and software, and UVS power, temperatures and heater state.

To operate the instrument, command sets were arranged into a relative time sequence (RTS) that executed specific commands sequentially. Each RTS was tested on a hardware-
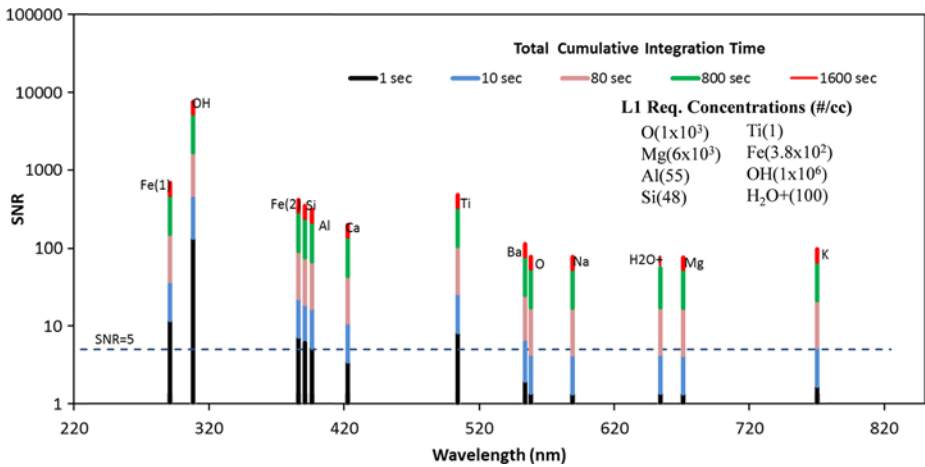
Fig. 20 The calculated SNR for several cumulative integration times for the various exospheric gas emission lines estimated for a detector temperature of −20 °C. The line strengths were calculated at the specified concentrations in the Level 1 requirement

in-the-loop simulator before first use. To incorporate an RTS into the larger spacecraft command sequence, the planning tool LASS (LADEE Activity Sequence Scheduler) was used. The spacecraft team would provide the individual instrument team an activity allocation for a 3–5 day period where the instruments would insert the desired RTSes and then in the science operations working group, these instrument plans would be combined into one larger science plan. From here, the science plan would receive updated ephemeris from the spacecraft and any updates to the spacecraft RTSes before being turned into a absolute time sequence (ATS). The ATS was uploaded to the spacecraft and provided each RTS with an absolute start time to run.

4.4 Expected Results

Prior to flight, ground calibrations and analyses were used to determine the expected performance of the UVS system for both "Limb" and "Occultation" activity types. These results can be extended in a general sense to other activity types given their viewing geometries and expected signal strengths (e.g., for a particular gas species or dust column).

For each of the gas species in the UVS Level 2 requirements (Sect. 1.3) the expected integration time to reach an SNR = 5 was calculated given the specified concentrations in the Level 2 requirement (Table 1) and laboratory radiance calibration. These calculations were made for a fixed g-factor (Table 1). While this is appropriate in many cases, in those cases where the g-factor may vary substantially (Sarantos et al. 2012) there was significant margin in total integration (e.g., Ti).

Figure 20 shows the calculated SNR for the exospheric species at the concentrations specified in the Level 1 requirements (Table 1) for several cumulative integration times. The calculations were made using a laboratory measured noise-equivalent power for a detector at −20 °C, but modified to account for in-flight measured increases in noise from radiation effects. Based on these analyses, new upper limits can be set for most species within a single UVS orbit. That said, some spectra during a particular activity may not be as applicable, due to observational constraints (e.g., pointing and off-axis scattering limits).
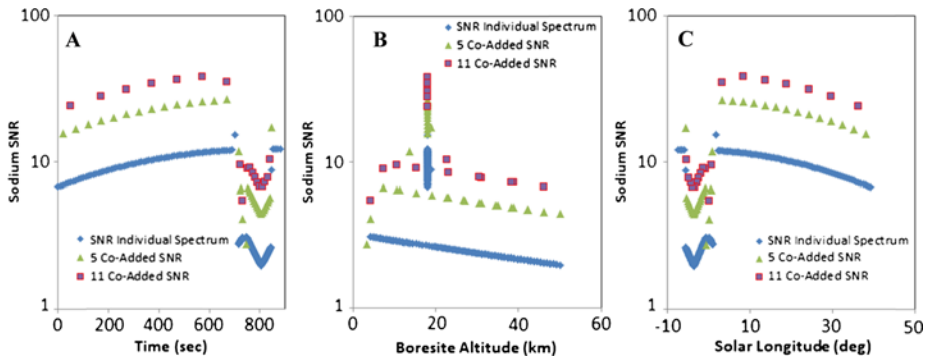
Fig. 21 Simulations of a UVS "Noon" activity showing the SNR for sodium. (**A**) The Sodium SNR vs activity time, (**B**) Sodium SNR vs. telescope boresight altitude, and (**C**) the Sodium SNR vs. telescope boresight altitude, and (**B**) the Sodium SNR vs. telescope boresight solar longitude with zeerboresight solar longitude

The expected SNR of any particular gas will depend on its spatial distribution. As listed in Sect. 1.3, a UVS goal is to measure the spatial variation of sodium and potassium. Spatial variations are determined by measuring concentrations at each of the two terminators and during the noon activity. Figure 21 highlights the UVS's capability of measuring sodium based on the UVS "Noon" limb stare with a nod maneuver. These simulations assumed sodium density varied as the square of the cosine of the solar zenith angle and as the cosine of the selenographic latitude. Panel A is the limb and nod activity as a function of time. Panel B is the same activity but as a function of the telescope bore sight altitude. The peak SNR are at the limb stare altitude of 18 km. Panel C is the same activity simulation, but this time plotted as a function of solar longitude. Since the UVS is looking in the anti-velocity direction, the graph is essentially the mirror image of the first.

Similar analyses were carried out for dust observations. Stubbs et al. (2010) provided a number of predictions for the total dust scatter, or lunar horizon glow (LHG), and possible background contributors, including zodiacal light (ZL). These studies indicated that at decreasing solar elongation angles, LHG becomes a decreasing fraction of the total signal, with the majority of signal contributed by ZL. Possibly distinct color differences between ZL and LHG may help to separate the two contributions. Additional studies were carried out by the UVS team which included forward and backward scattered radiances calculated using DISORT (Discrete Ordinates Radiative Transfer) (Stamnes and Conklin 1984). Dust clouds with various mean radii were used to calculate optical depths. For each mean radius a log-normal distribution of dust grains was assumed with a variance of 1.5. Optical coefficients were calculated using Mie theory and indices of refraction for SiO_2. Total transmission through a dust cloud was also calculated using DISORT to support UVS occultation measurements. Figure 22 shows results for these dust simulations for forward and backward scattering radiances and the UVS Noise Equivalent Power (NEP), that is the power need to equal the instrument noise level (i.e., SNR = 1). Also shown in Fig. 22 is the expected off-axis light scattering contribution from fully lit lunar surface scattering into the limb-viewing telescope as the telescope holds a fixed stare point 50 km above the surface (for example, late into a noon activity). For this estimate off-axis contribution curve shown in Fig. 11 was convolved with a lunar reflectance model (Buratti et al. 2011). To minimize the effects of lunar surface scattering, UVS activity times were adjusted in flight such that illuminated atmosphere was observed while the UVS instrument was positioned over dark (including SC in lunar umbra) or dimly-lit lunar surfaces at each of the two terminators (both in forward

Fig. 22 Examples of calculated forward and backscatter radiance for dust grains with radii = 100 nm (see text for details). Also plotted is the estimated off-axis scattering contribution for an activity over fully lit surface (Rej = 2e-3) and for Rej = 1e-4 and 1e-5 which are typical for activities with partly lit surfaces (e.g., sunrise and sunset activities). Also shown is the instrument NEP (−20 °C)
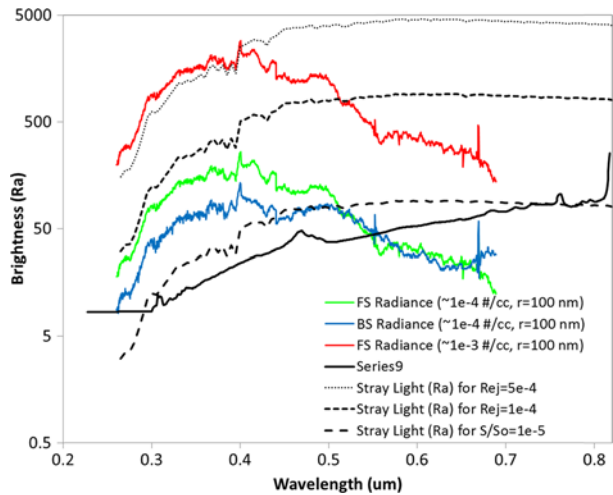
and backward views). In these instances the dust detection limit is determined by the UVS NEP.

Solar Occultation measurements have the benefit of having very high SNR, with typical SNR greater as high as 1000 at some wavelengths in a single 15–30 msec integration time. The high sample rate allows for vertical sampling, as the sun appears to set, of approximately the angular size of the solar disk up until the solar disk touches the lunar limb. For a solar disk angular size of 0.52 deg this results in an approximate 3.7 km vertical sampling for a spacecraft at an orbit altitude of 50 km. The duration of the occultation is approximately 2.2 minutes (from 35 km to the lunar limb, although it varies by approximately 0.2 minutes from activity to activity) giving a vertical rate of motion of about 0.23 km per sec. At a sample rate of 25 msec, the motion of the solar disk is greatly over resolved and thus allows for additional co-adding of spectra to build SNR further. The high SNR and rapid sampling allows for observations very near the surface, where previous models have predicted dust concentrations to be highest. For example, the dust model of McCoy and Criswell (1974) predicted dust concentrations as high as 0.1–1 grains per cc. The expected extinction (I/Io) for 100 nm dust grains was calculated using the same grain size distribution and optical constants used as before for a range of dust concentrations (Fig. 23). Dust grains with radii = 100 nm and a concentration of 10^{-4} per cc will have an optical depth of approximate 2×10^{-6}, results in a total extinction (I/Io) of approximately 2×10^{-6}. As dust concentration increases, for example per the model of McCoy and Criswell (1974), as long as the dust is optically thin, the extinction will increase linearly, thus the McCoy model would predict extinctions as high as 3×10^{-2} at altitudes below 20 km. Also shown in Fig. 23 is the estimated sensitivity (1/SNR) for a single occultation scan, 5 co-added and 20 co-added scans.

5 Summary

The LADEE UVS instrument is a simple, robust system that allows for a variety of different observation options, both for dust and gases. UVS provides unique observations of sodium and potassium, able to monitor these gases at a variety of local times over several lunations. These observations combined with observations from the other LADEE instruments and
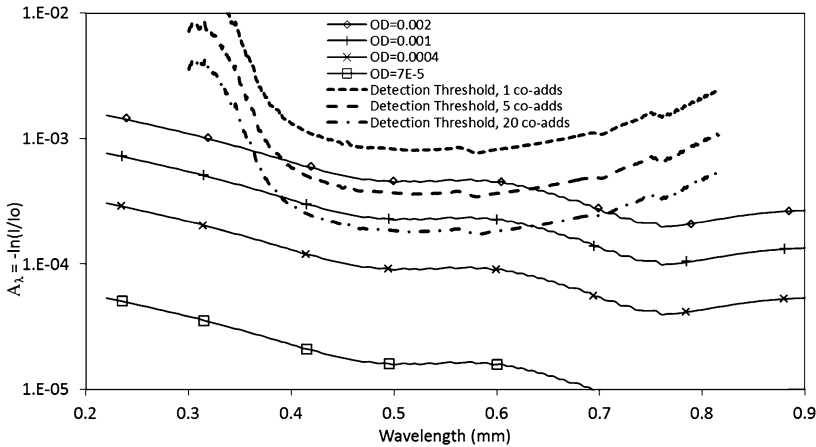
Fig. 23 Shown is the predicted absorbance, $A_\lambda = -\ln(I/I_o)$, of sunlight for several dust column optical depths (OD). The smallest OD corresponds to a dust concentration of 1e-4 #/cc of 100 nm dust grains. At altitudes of less than 20 km the McCoy and Criswell (1974) predicted dust ODs of >3e-2. Also shown is the estimated sensitivity of UVS, in terms of measurable absorbance, for a single occultation scan and co-adds of 5 and 20 scans

models of the lunar exosphere will provide constraints on the relative importance of impact vaporization, sputtering and PSD. Likewise, UVS provides either measurements or new upper limits on a variety of gas species and dust. The operation of the UVS instrument was relatively complex, having to coordinate SC attitude maneuvers to point the instrument fore-optics with instrument operation. Cooperation with the Project Science and other instrument operation planners was critical. Use of the LASS scheduling tool, with a 2–4 day tactical planning cycle, proved very successful, approximately doubling the number of observations made by UVS over what was expected prior to launch. Likewise, timing of operations was efficiently adjusted to minimize scattering and, later in the mission, further adjusted to allow for increased cooling of the CCD, minimizing thermal noise.

References

A. Bhardwaj, S. Raghuram, A coupled chemistry-emission model for atomic oxygen green and red-doublet emissions in the comet C/1996 B2 Hyakutake. Astrophys. J. **748**, 18 (2012)

B.J. Buratti, M.D. Hicks, J. Nettles, M. Staid, C.M. Pieters, J. Sunshine, J. Boardman, T.C. Stone, A wavelength-dependent visible and infrared spectrophotometric function for the Moon based on ROLO data. J. Geophys. Res. **116**, E00G03 (2011)

R.P. Cageao, Y.L. Ha, Y. Jiang, M.F. Morgan, Y.L. Yung, S.P. Sander, Calculated hydroxyl A2Σ → X2Π (0, 0) band emission rate factors applicable to atmospheric spectroscopy. J. Quant. Spectrosc. Radiat. Transf. **57**, 703–717 (1997)

K. Chance, R.L. Kurucz, An improved high-resolution solar reference spectrum for earth's atmosphere measurements in the ultraviolet, visible, and near infrared. J. Quant. Spectrosc. Radiat. Transf. **111**, 1289–1295 (2010)

D.H. Crider, R.R. Vondrak, The solar wind as a possible source of lunar polar hydrogen deposits. J. Geophys. Res. **105**(E11), 26773 (2000)

D.R. Criswell, Horizon-glow and the motion of lunar dust, in *Photon and Particle Interaction in Space*, ed. by R.J.L. Grard (Reidel, Dordrecht, 1973), p. 545

K. Ennico, M. Shirley, A. Colaprete, L. Osetinsky, The Lunar Crater Observation and Sensing Satellite (LCROSS) payload development and performance in flight. Space Sci. Rev. **167**, 23–69 (2012)

P.D. Feldman, D.A. Glenarb, T.J. Stubbs, K.D. Retherford, G.R. Gladstone, P.F. Miles, T.K. Greathouse, D.E. Kaufmann, J.W. Parker, S.A. Stern, Upper limits for a lunar dust exosphere from far-ultraviolet spectroscopy by LRO/LAMP. Icarus **233**, 106–113 (2014)

B.C. Flynn, S.A. Stern, A spectroscopic survey of metallic species abundances in the lunar atmosphere. Icarus **124**(2), 530–536 (1996)

D.A. Glenar, T.J. Stubbs, J.E. McCoy, R.R. Vondrak, A reanalysis of the Apollo light scattering observations, and implications for lunar exospheric dust. Planet. Space Sci. **59**(14), 1695–1707 (2011)

M. Horanyi, S. Gagnard, D. Gathright, E. Gruen, D. James, S. Kempf, M. Lankton, R. Srama, Z. Sternovsky, J. Szalay, The Dust Environment of the Moon as Seen by the Lunar Dust Experiment (LDEX), in *45th Lunar and Planetary Science Conference, Held 17–21 March, 2014 at The Woodlands, Texas. LPI Contribution No. 1777* (2014), p. 1303

R.R. Hodges Jr., Methods for Monte Carlo simulation of the exospheres of the Moon and Mercury. J. Geophys. Res. **85**(A1), 164–170 (1980)

M. Kagitani, M. Taguchi, A. Yamazaki, I. Yoshikawa, G. Murakami, K. Yoshioka, S. Kameda, S. Okano, Variation in lunar sodium exosphere measured from lunar orbiter SELENE (Kaguya). Planet. Space Sci. **58**(12), 1660–1664 (2010)

The Lunar Exploration Roadmap: Exploring the Moon in the 21st Century: Themes, Goals, Objectives, Investigations, and Priorities, Lunar Exploration Analysis Group (LEAG) (2011)

T.E. Madey, B.V. Yakshinskiy, V. Ageev, R.E. Johnson, Desorption of alkali atoms and ions from oxide surfaces—Relevance to origins of NA and K in atmospheres of Mercury and the moon. J. Geophys. Res. **103**, 5873 (1998)

P. Mahaffey et al., The neutral mass spectrometer on the lunar atmosphere and dust environment explorer mission. Space Sci. Rev. (2014). doi:10.1007/s11214-014-0043-9

M. Matta, S. Smith, J. Baumgardner, J. Wilson, C. Martinis, M. Mendillo, The sodium tail of the Moon. Icarus **204**, 409–417 (2009)

J.E. McCoy, D.R. Criswell, Evidence for a high latitude distribution of lunar dust, in *Proc. Lunar Sci. Conf. 5th* (1974), p. 2991

A.D. Michael, U. Fink, A.B. Schultz, Spatial distribution of H_2O^+ in Comet P/Halley. Icarus **86**, 152–171 (1990)

National Research Council—Committee on the Scientific Context for Space Exploration. The National Academies Press (2003)

National Research Council—Decadal Survey, Visions and Voyages for Planetary Science in the Decade 2013–2022. National Academies Press (2011)

A.E. Potter, R.M. Killen, T.H. Morgan, Variation of lunar sodium during passage of the Moon through the Earth's magnetotail. J. Geophys. Res. **105**(E6), 15073–15084 (2000)

J.J. Rennilson, D.R. Criswell, Surveyor observations of lunar horizon glow. The Moon **10**, 121 (1974)

M. Sarantos, R.M. Killen, A.S. Sharma, J.A. Slavin, Influence of plasma ions on source rates for the lunar exosphere during passage through the Earth's magnetosphere. Geophys. Res. Lett. **35**, L04105 (2008)

M. Sarantos, R.M. Killen, S.A. Surjalal, J.A. Slavin, Sources of sodium in the lunar exosphere: Modeling using ground-based observations of sodium emission and spacecraft data of the plasma. Icarus **205**, 364–374 (2010)

M. Sarantos, R.M. Killen, D.A. Glenar, M. Benna, T.J. Stubbs, Metallic species, oxygen and silicon in the lunar exosphere: Upper limits and prospects for LADEE measurements. J. Geophys. Res. **117**(A3), A03103 (2012)

The Scientific Context for Exploration of the Moon (SCEM), Committee on the Scientific Context for Exploration of the Moon, Space Studies Board, Division on Engineering and Physical Sciences, National Research Council of the National Academies. The National Academies Press (2007)

A.B. Severny, E.I. Terez, A.M. Zvereva, The measurements of sky brightness on Lunokhod-2. The Moon **14**, 123–128 (1975)

A.L. Sprague, R.W. Kozlowski, D.M. Hunten, W.K. Wells, F.A. Grosse, The sodium and potassium atmosphere of the moon and its interaction with the surface. Icarus **96**, 27–42 (1992)

K. Stamnes, P. Conklin, A new multi-layer discrete ordinate approach to radiative transfer in vertically inhomogeneous atmospheres. J. Quant. Spectrosc. Radiat. Transf. **31**, 273–282 (1984)

S.A. Stern, J.W. Parker, T.H. Morgan, B.C. Flynn, D.M. Hunten, A. Sprague, M. Mendillo, M.C. Festou, NOTE: an HST search for magnesium in the lunar atmosphere. Icarus **127**(2), 523–526 (1997)

A.S. Stern, The lunar atmosphere: history, status, current problems, and context. Rev. Geophys. **37**, 453 (1999)

T.J. Stubbs, R.R. Vondrak, W.M. Farrell, A dynamic fountain model for lunar dust. Adv. Space Res. **37**, 59–66 (2006)

T.J. Stubbs, D.A. Glenar, A. Colaprete, D.T. Richard, Optical scattering processes observed at the Moon: Predictions for the LADEE Ultraviolet Spectrometer. Planet. Space Sci. **58**(5), 830–837 (2010)

H.A. Zook, E. McCoy, Large scale lunar horizon glow and a high altitude lunar dust exosphere. Geophys. Res. Lett. **18**, 2117 (1991)

The Lunar Dust Experiment (LDEX) Onboard the Lunar Atmosphere and Dust Environment Explorer (LADEE) Mission

M. Horányi · Z. Sternovsky · M. Lankton · C. Dumont · S. Gagnard · D. Gathright · E. Grün · D. Hansen · D. James · S. Kempf · B. Lamprecht · R. Srama · J.R. Szalay · G. Wright

Abstract The Lunar Dust Experiment (LDEX) is an *in situ* dust detector onboard the Lunar Atmosphere and Dust Environment Explorer (LADEE) mission. It is designed to characterize the variability of the dust in the lunar exosphere by mapping the size and spatial distributions of dust grains in the lunar environment as a function of local time and the position of the Moon with respect to the magnetosphere of the Earth. LDEX gauged the relative contributions of the two competing dust sources: (a) ejecta production due to the continual bombardment of the Moon by interplanetary micrometeoroids, and (b) lofting of small grains from the lunar surface due to plasma-induced near-surface electric fields.

Keywords Lunar · Dust · Exosphere · LADEE mission · Instrumentation

1 Introduction

NASA's Lunar Atmosphere and Dust Environment Explorer LADEE mission was launched on September 6, 2013; and it reached lunar orbit a month later on October 6, 2013. LADEE's

M. Horányi (✉) · Z. Sternovsky · M. Lankton · C. Dumont · S. Gagnard · D. Gathright · E. Grün · D. Hansen · D. James · S. Kempf · B. Lamprecht · J.R. Szalay · G. Wright
Laboratory for Atmospheric and Space Physics, University of Colorado, Boulder, CO 80303, USA
e-mail: horanyi@colorado.edu

M. Horányi · Z. Sternovsky · M. Lankton · E. Grün · D. James · S. Kempf · J.R. Szalay
Solar System Exploration Research Virtual Institute (SSERVI)—Institute for Modeling Plasmas, Atmospheres, and Cosmic Dust (IMPACT), University of Colorado, Boulder, USA

E. Grün
Max Planck Institut für Kernphysik, 69117 Heidelberg, Germany

R. Srama
Institut für Raumfahrtsysteme, Universität Stuttgart, Raumfahrtzentrum Baden Württemberg, 70569 Stuttgart, Germany

R. Srama
Baylor University, Waco, TX 76706, USA

scientific objectives include the characterization of the lunar dust environment (Delory et al. 2009; Elphic et al. 2012, 2013). The lunar dust environment is expected to be dominated by submicron-sized dust particles: (i) released from the Moon due to the continual bombardment by interplanetary micrometeoroids (Grün et al. 2011); and (ii) possibly lofted due to UV radiation and plasma-induced near-surface intense electric fields (Sternovsky et al. 2008). The Lunar Dust Experiment (LDEX) instrument is designed to map the variability of the dust size and density distributions in the lunar environment (Horányi et al. 2009, 2012). LDEX is an impact ionization detector, capable of reliably detecting and measuring the mass of individual submicron and micron sized dust grains. LDEX also measures the collective signal of multiple impacts of dust particles that are below the detection threshold for single impacts; hence it can search for the putative population of grains with radii $\simeq 0.1$ μm lofted over the terminator regions by plasma effects (De and Criswell 1977; Pelizzari and Criswell 1978).

LDEX is the first high-sensitivity dust instrument dedicated to exploring the lunar dust environment, it is capable to detect particles with masses down to $m \simeq 10^{-15}$ kg, and covers an altitude range of $\simeq$ 3–250 km. We are aware of only one previous attempt to identify the lunar ejecta cloud. The Munich Dust Counter (MDC) onboard the HITEN satellite in orbit about the Moon (February 15, 1992 to April 10, 1993) covered a typical altitude range of 10^4–$5 \cdot 10^5$ km. The MDC could not identify the lunar ejecta cloud due to its large distance from the surface and high detection threshold. MDC recorded a total of about 150 detections of lunar and/or interplanetary dust particles (Iglseder et al. 1996).

Ejecta clouds were first observed *in situ* by the Galileo mission during flybys of the icy moons of Jupiter: Europa, Ganymede, and Callisto (Krüger et al. 1999, 2000). The observations by the Cosmic Dust Analyzer onboard Cassini in orbit around Saturn indicate that, in addition to the active plumes on Enceladus, ejecta particles also make a non-negligible contribution to the dust environment of Saturn (Spahn et al. 2006; Kempf et al. 2010). Ejecta clouds are expected to engulf all airless planetary objects, including the Moon, asteroids, dormant comets, Mercury, and the moons of Mars: Phobos and Deimos. LDEX is designed to identify and characterize the ejecta cloud surrounding the Moon.

LDEX will also search for the putative population of plasma-lofted particles. These particles, with characteristic radii of $\simeq 0.1$ μm (McCoy and Criswell 1974; McCoy 1976), have been suggested to lift off the surface due to the combination of charging and intense localized electric fields. The processes involved remain controversial. The combination of the remote sensing optical observation by the LADEE Ultraviolet and Visible Spectrometer (UVS) and the *in situ* LDEX measurements are expected to establish upper limits for the density of these particles.

In this paper we summarize the science background and LDEX measurement requirements in Sect. 2, the engineering details of the instrument, and the description of the data products are described in Sect. 4. The initial results, demonstrating that LDEX is operational and capable of delivering the required measurements, are summarized in Sect. 5.

2 Science Background

The LDEX instrument addresses the LADEE science objective to "Characterize the lunar exospheric dust environment, measure any spatial and temporal variability, and their impacts on the lunar atmosphere." LDEX is designed to detect micron and submicron sized particles, in order to gauge the relative importance of the two expected sources of dust: (i) ejecta production due to continual bombardment by interplanetary meteoroids, and (ii) lofting due to plasma effects.
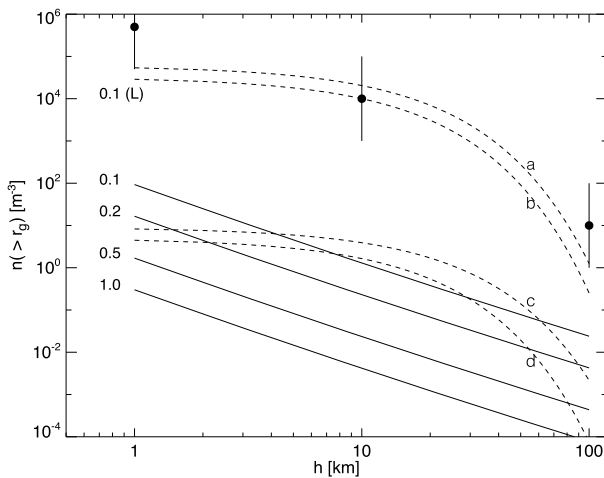
Fig. 1 The predicted cumulative number density (*solid lines*) of the ejecta cloud around the Moon as function height based on the theoretical model by Krivov et al. (2003). *The numerical labels* indicate the smallest particle sizes contributing to the density. *The data points with error bars* represent the estimate for the density of plasma lofted (L) dust particles from excess coronal brightness observations (McCoy 1976). *The dashed lines* are analytical models for the distribution of lofted particles based on the original (a) and the reanalysis (b) of the Apollo observations (Glenar et al. 2011), and the more recent Clementine (Glenar et al. 2014) (c), and LRO measurements (Feldman et al. 2014) (d), showing a systematic trend toward decreasing density estimates

Meteoroid impacts eject material, both neutral and charged, that become part of the lunar environment. The impact-generated ions and neutrals contribute to sustaining the lunar atmosphere and ionosphere (Stern 1999). Based on the meteoroid influx into the Earth's atmosphere on the order of 10^5 kg/day (Love and Brownlee 1993), the Moon is also expected to be bombarded by particles delivering $\simeq 5 \cdot 10^3$ kg/day of cosmic material mainly in the form of particles with radii of about 100 μm (Grün et al. 1985), and characteristic impact speeds $\simeq 20$ km s^{-1} (Taylor 1996). The initial speed of the vast majority of the ejected dust is below the escape speed from the Moon ($v_{escape} = 2.4$ km/s), hence they are returned to the surface by gravity. The particles follow ballistic motion, and form a continually present dust exosphere around the Moon.

Figure 1 shows the predicted—though highly uncertain—density of ejecta grains in the lunar dust exosphere, based on models developed to describe the ejecta clouds surrounding the icy moons of Jupiter (Krüger et al. 2000; Krivov et al. 2003; Sremčević et al. 2003). Figure 2 shows the expected densities and impact rates for a characteristic LADEE orbit. During meteor showers, the ejecta population is expected to increase with a spatial distribution showing strong deviations from spherical symmetry.

The lunar surface is exposed to UV radiation and the solar wind plasma flow. This leads to electrostatic charging of the surface, and possible small-scale intense electric fields across lit and dark regions. Existing *in situ* and remote sensing observations suggest that dusty plasma processes could result in the mobilization and transport of the lunar soil (Criswell 1973; Rennilson and Criswell 1974; Berg et al. 1973; Colwell et al. 2007; Grün et al. 2011). Modeling the excess brightness of the solar corona above the lunar terminator during Apollo 15 and 17 led to the suggestion of a significant dust exosphere over the terminator region, extending to altitudes > 100 km, with an integrated column density of 10^{-10} kg/m^2, and a characteristic grain radius of 0.1 μm (McCoy 1976; Zook and McCoy 1991; Murphy and Vondrak 1993).
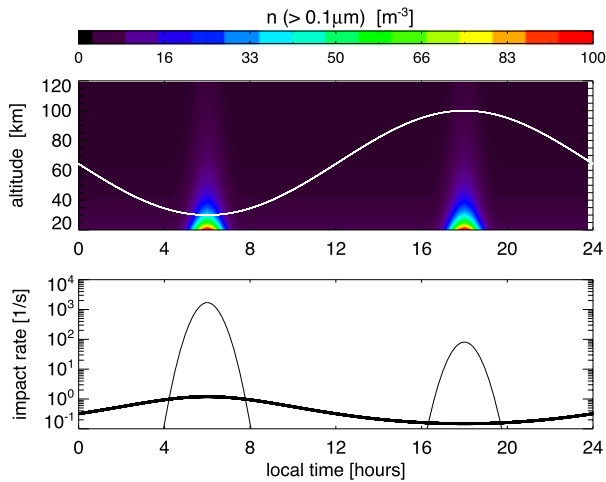
Fig. 2 *Top*: the expected density of grains with radii $r_G \geq 0.1$ μm as function of local time (LT) and altitude. The density of the ejecta cloud changes slowly with height and remains independent of LT. The high-density regions localized at the sunrise and sunset terminators show plasma lofted particles. A 30 by 100 km eccentric LADEE orbit is also shown (*white line*) with an assumed pericenter over the sunrise terminator. LADEE follows a retrograde orbit, hence at this point it will cross into the shadow. *Bottom*: the expected impact rate of ejecta particles with $r_g \geq 0.3$ μm (*thick line*) and the plasma lofted grains (*thin lines*)

However, a followup study of the same observations indicates lower column densities (Glenar et al. 2011). More recent observations by the star tracker camera onboard the Clementine (Glenar et al. 2014) and the LAMP instrument onboard the LRO missions (Feldman et al. 2014) indicate even lower upper limits for the density of the high altitude dust exosphere. The putative density of lofted grains over the terminator region is shown in Fig. 1.

LADEE follows a small eccentricity, retrograde, equatorial orbit at a characteristic altitude of $h \simeq 50$ km and excursions spanning the typical range of $\simeq 15$–100 km. During the initial commissioning period LADEE followed a near circular orbit at an altitude of 250 km, and towards the end of the mission it will intermittently skim the lunar surface at altitudes even below 3 km. The dust density LDEX observes is dominated by grains on bound orbits close to the maximum height of their ballistic motion. Hence, the impact speed between the grains and a detector will remain close to the speed of the spacecraft itself $v_{s/c} \simeq 1.6$ km s^{-1}. The LADEE orbital period is $P \simeq 1.8$ hour. It will make measurements for > 2000 orbits over a period of approximately 6 months. LDEX observes both the impact ejecta and the population of dust lofted by plasma effects. LDEX measures the temporal variability of the size and spatial distributions of submicron sized particles and identifies the possible effects of: (a) the position of the Moon with respect to the Earth's magnetosphere; (b) solar wind and UV variability; and (c) meteor shower activities.

3 Instrument Accommodation

LADEE began its $\simeq 150$ days of science observations in the typical altitude range of 20–100 km, following a near-equatorial retrograde orbit, with a characteristic orbital speed of 1.7 km/s (Elphic et al. 2014). In addition to LDEX, LADEE carried a Neutral Mass Spectrometer (Mahaffy et al. 2014), an Ultraviolet/Visible Spectrometer (Colaprete et al. 2014),

and a Laser Communication Demonstration Experiment (Elphic et al. 2014). LDEX began its measurements on October 16, 2014. During normal operations LDEX was pointed $\pm 5°$ of the ram direction, along the vector of the spacecraft speed with respect to the Moon.

4 Instrument Description

LDEX is an impact ionization dust detector, derived from the heritage of the dust instruments operating on HEOS 2 (Dietzel et al. 1973), Galileo (Grün et al. 1992a), Ulysses (Grün et al. 1992b), and Cassini (Srama et al. 2004) missions. The detection of a dust particle is based on measuring the charge generated by its hypervelocity ($> 1\,\mathrm{km\,s}^{-1}$) impact on a target. The impact charge Q (the total number of ions or electrons) is a function of both the speed v, and the mass m, of the impacting dust particle

$$Q = \alpha m v^{\beta}, \tag{1}$$

where the charge is measured in C, the mass in kg, and the speed in $\mathrm{km\,s}^{-1}$. The speed exponent is in the range $3.5 \leq \beta \leq 5.6$ (Auer 2001). For a characteristic value of $\beta = 3.5$, $\alpha \simeq 0.5$. The values for both α and β have to be determined by calibrating individual instruments as they depend on the composition of both the impactor and the target, and the geometry of the setup (e.g., Göller and Grün 1989).

Figures 3–5 show the LDEX instrument. A dust particle impacts its hemispherical target and generates a plasma cloud. A negative bias potential on the ion focusing grid creates a radial electric field separating the electrons and negative ions from positive ions. The electrons and the negative ions are collected on the target and measured by a charge sensitive amplifier (CSA). The positive ions are detected by a microchannel plate (MCP) placed behind a focusing grid. The MCP output is connected to a CSA to measure the impact charge from individual impacts. The mass and size of the dust particle is calculated from the impact charge using laboratory calibration data. To search for the putative population of small particles with masses below the single event detection threshold, the integrated MCP signal is also recorded. UV induced photoelectrons, solar wind and lunar ionospheric ions, and, if present, the continually generated impact charges of the lofted small particles might all contribute to this signal. The electric field between the target and the focusing grid in front of the MCP is periodically reversed from -200 V to $+30$ V, making LDEX 'blind' to the contributions from dust impacts and low energy ions. These periods provide a self-calibration to remove the contributions from sources other than the small dust particles. Further discussions on these electric field reversals are given in Sect. 4.5.2.
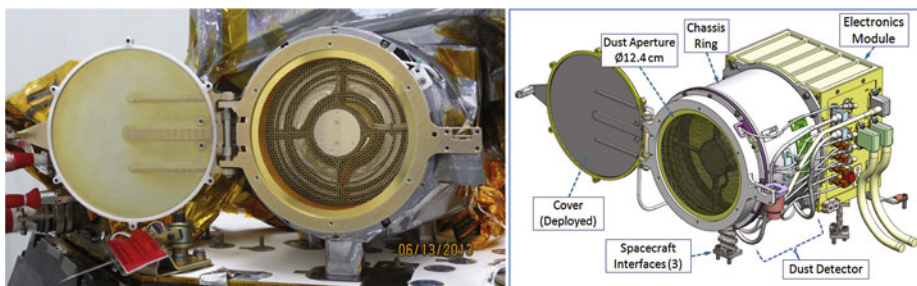
Fig. 3 The Lunar Dust Experiment (LDEX) instrument on the top deck of the LADEE spacecraft during its integration in June, 2013, and its schematic drawing
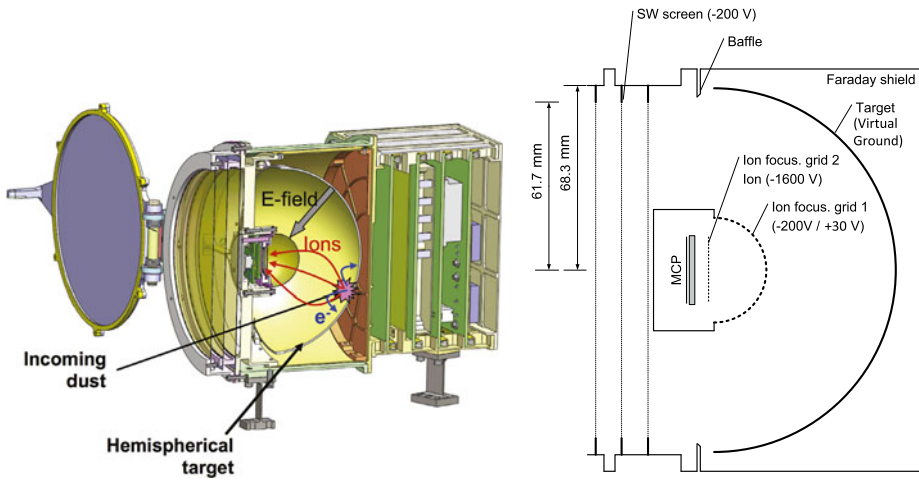
Fig. 4 *Left*: cutaway of the entire LDEX instrument. *Right*: the LDEX target section indicating the arrangement of the solar wind and ion acceleration grids with dimensions measured in millimeters

4.1 Principle of Operation

The schematic diagram of LDEX is shown in Fig. 4. There are three high open area (90 %) grids over the instrument aperture. The outermost is at chassis ground. The middle one is biased -200 V, and its function is to keep solar wind electrons from entering the instrument. The inner grid is at signal ground. The particles can enter LDEX within the dust field-of-view (FOV) of $\pm 68°$ off from the normal direction and impact on the hemispherical target. The ion focusing hemispherical grid (#1) is concentric with the target. This grid is nominally biased at -200 V and its function is to generate a radial electric field, which separates the positive and negative charges in the impact plasma. A second focusing flat grid (#2), biased at -1600 V is used to focus the ions onto the MCP detector. This grid is necessary to collect most ions from each impact, regardless of where the incoming dust particles hit the target. The ion-optical properties of LDEX have been modeled and optimized using the commercially available SIMION software package.

The positive ions are measured by the MCP, which provides an effective gain on the order of 300. The electrons and negative ions are collected on the target, which is directly connected to a charge sensitive amplifier. For best performance, the target is enclosed in a Faraday shielding cage that is connected to the signal ground of the CSA.

4.2 Mechanical Design

The LDEX instrument consists of three basic components: the deployable cover, the electronics module and the dust detector portion of the instrument. The instrument structure is primarily manufactured from machined (thin-walled) aluminum, with three compliant titanium flexures at the spacecraft interface. These flexures are designed to accommodate launch environment forces and on-orbit thermal stresses at the spacecraft interface. Figure 4 shows the overall LDEX layout, with the Ø12.4 cm aperture. Overall the LDEX instrument is 22.0 cm long, 21.5 cm tall, and 36.8 cm wide with the cover deployed. The total mass of the LDEX instrument is 3.6 kg.
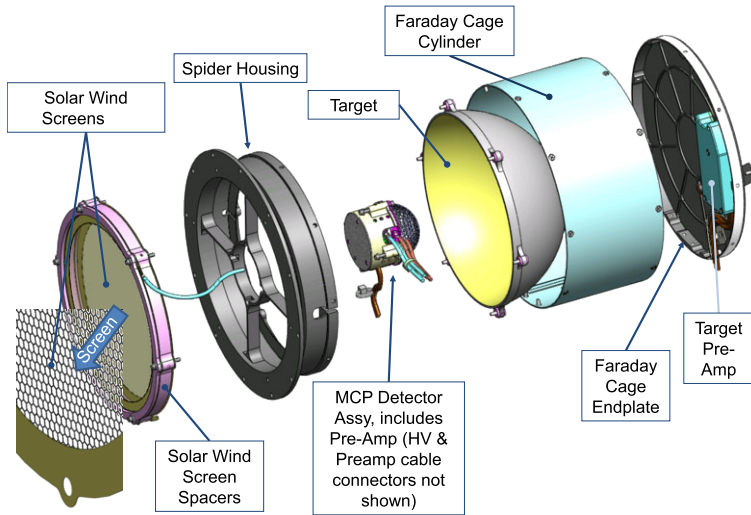
Fig. 5 An exploded view showing the Faraday cage, the Target, the Solar Wind screens and the MCP assembly

The LDEX instrument includes a one-time deployable cover. The cover protects the instrument from debris during launch and ascent, and enables the instrument to be maintained under a dry nitrogen purge throughout integration and testing. The cover is latched with a TiNi pin-puller, and the hinges are redundantly spring-loaded to keep the cover out of the field of view on-orbit.

The electronics module provides structure and EMI shielding for the front end board, the high voltage power supply board, the controller board and the low voltage power supply board. The four boards are joined via a backplane board. The electronics module structure is manufactured from aluminum, and provides 1 mm thickness of aluminum radiation shielding between the electronics and the space environment. The external surfaces of the electronics module are covered with thermal control materials including MLI and silver-teflon tape.

The dust detector components are housed within the structural chassis ring. The Target and MCP Detector Assembly are supported within the structure in an electrically isolated Faraday cage to minimize noise from the spacecraft. Figure 5 shows a sectioned view of the dust detector components. The dust target's Field Of View (FOV) is approximately 136° and the UV FOV is approximately 169°. The polished and rhodium plated target is designed to specularly reflect UV light that enters the detector harmlessly back into space. The solar wind screens are chem-etched from BeCu and are then gold plated. The screens are 90 % open area, and the orientation of the three screens is such that the total transmission is $(90 \%)^3 = 72 \%$ at 0° incidence angle. The MCP hemispherical grid is 62 % open, and the BeCu flat grid near the MCP is 82 % open area. The preamplifier for the target is attached to the inside of the back of the Faraday cage to minimize the length of the cable between the target and preamp and to minimize interference from the rest of the instrument electronics. Similarly, the preamp for the MCP is built-in to the MCP housing.

4.3 Thermal Design

The lunar equatorial orbit of the LADEE spacecraft exposes LDEX to a highly variable thermal environment. In addition to the incident solar flux, the lack of atmosphere and low

Fig. 6 The predicted temperature variations during science and communication orbits. Gray portions indicate times LDEX was off
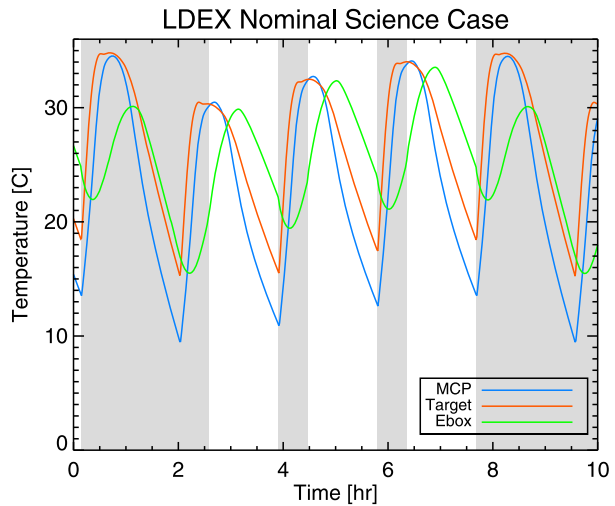
surface albedo cause the lunar IR heat load to reach values up to 1314 W m^{-2}, nearly equivalent to the sun at 1 AU. The dark side planetary IR heat load is about 5 W m^{-2}. LDEX utilizes a passive thermal control design to maintain an operational temperature range of $-25\,°C$ to $+50\,°C$ while passing through this extreme environment. This is accomplished through the use of multi-layer insulation blankets covering most of the instrument, and radiator surface locations chosen to minimize solar and lunar IR loading. During a portion of each orbit, the sun shines into the LDEX aperture. The highly polished, rhodium-coated hemispherical target reflects about 75 % of the solar energy back out of the aperture, helping maintain reasonable instrument temperatures. Though nominally planned to be off during this part of the orbit, the LDEX thermal design accommodates a 100 % duty cycle scenario. LDEX is thermally isolated from the spacecraft deck through the use of titanium flexure mounts. A survival heater maintains minimum instrument temperatures when LDEX is powered off. Even with these design considerations, LDEX temperature profiles are highly transient due to the environmental variations and the low instrument mass. A representative thermal profile of three science orbits and a communication orbit is shown in Fig. 6.

4.4 Electronics

The block diagram of the LDEX instrument is shown in Fig. 7. The high voltage power supply and the low voltage DC/DC converters are used to generate all bias voltages. A Field Programmable Gate Array (FPGA) implements all logic, processes incoming commands, and handles all science and housekeeping data. The 16-bit Analog/Digital Converters (ADCs) feed the MCP and CSA data into the FPGA for temporary storage in a circular buffer. A trigger discriminator identifies dust impacts, and initiates data readout from the buffer. Science and housekeeping data are stored in SRAM until they are transferred to the LADEE spacecraft. A data ready signal is used to allow the spacecraft to initiate telemetry data transfer. There are two connectors to interface to the spacecraft, which consists of the primary and redundant +30 V power, and the RS-422 command/telemetry. The total power consumption of LDEX is ≤ 5 W. Figure 8 shows the front-end analog electronics. These signals are processed through two channels in parallel, the integrator and impact detection channels. All data are packetized in accordance with the standard packet format recommended by the Consultative Committee for Space Data Systems (CCSDS).

Lunar Dust EXperiment
Impact Ionization Detector

HVPS

LVPS

ANALOG

FPGA

CONTROLLER

Safe/Arm Plug
9 pin D(F)
HV inhibited when
installed

SC Power
9 pin D (M)

SC Comm
15 pin HD (F)

+28V HTR
Temp (x2)

Survival Heater (28V)
2 Temp Sensors (AD590)

Inhibit

OPEN COVER
STATUS
-200V
-200V/-1600V/+30V
-200V/-1100V

Diode-
Capacitor
Multiplier

Clock_n
Clock

Reg Reg Reg Reg Reg

Adjust

En

Switch Bank

HVPS/Cover
Control

Control
Registers

Command
Processing

Sync

CCSDS

25 MHz
Clock

Telemetry
Commands
Sync (1 Hz Pulse)

RS-422

EMI Filter &
Soft-Start
Circuit

28V RTN
+28V

Interpoint
DC / DC
Converter

Interpoint
DC / DC
Converter

+3.3V   ±5V

Science ADC
Control

Sun
Detection

Impact
Trigger

Counter

Integrated
Current Collection

Waveform
Buffers

Housekeeping

Data
Egress

LDO
Regulator

+1.5V

MCP

Ion
Focusing
Grids

CSA

ADC

ADC

Integrator

ADC

CSA

Target

ADC

Housekeeping
Monitors
(on all boards)

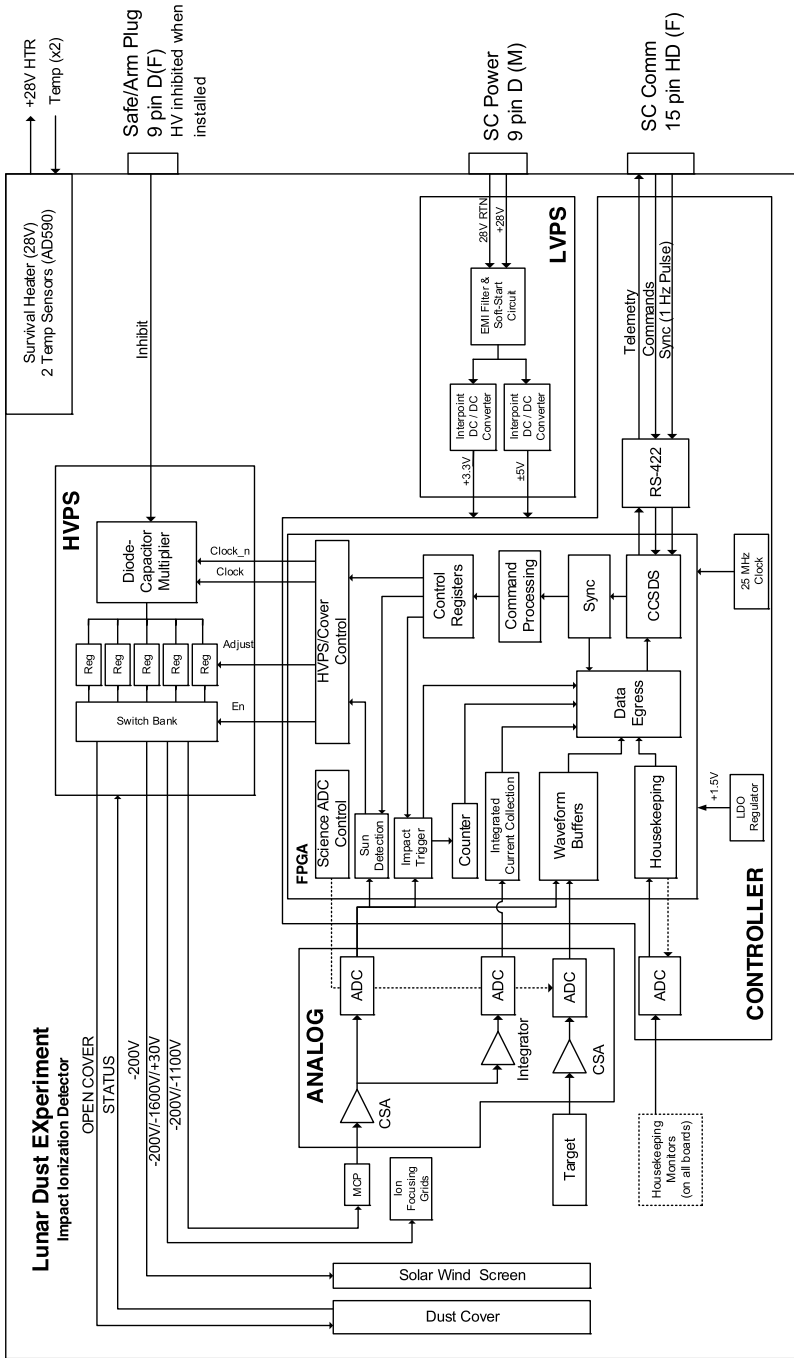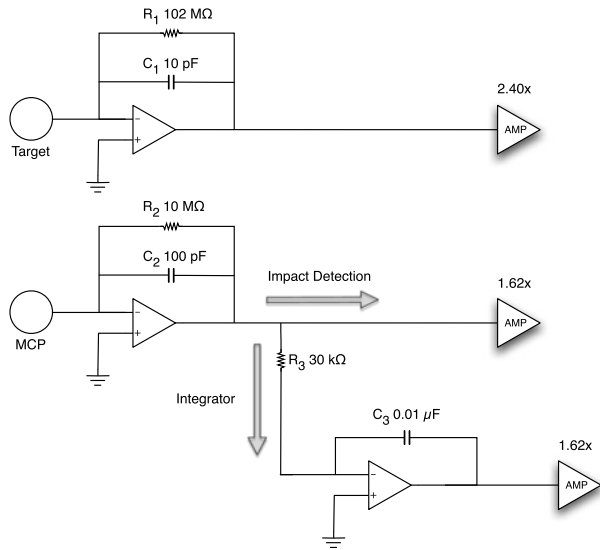Solar Wind Screen

Dust Cover

Fig. 7 LDEX electronics block diagram

Fig. 8 LDEX analog electronics


4.4.1 Event Detection

LDEX is an event-driven instrument and the data acquisition is triggered by the MCP signal increasing over a preset threshold level. The verification of an event detection is performed by comparing the microchannel plate (MCP) signal characteristics against a set of programmed parameters. A running buffer holds the last 50 samples recorded at 8 μs intervals for both the target and the MCP signals. Once the MCP signal amplitude exceeds a programmable impact threshold, the 15 samples prior to and 35 points after threshold crossing for both MCP and Target are stored to temporary storage and the impact detection logic activates. The MCP signal is then processed and compared to adjustable parameters to determine if a valid impact has occurred based on (i) pulse width; (ii) time to peak value; (iii) sum of 50 samples/peak amplitude, and (iv) the time for the signal to drop back below the threshold. These rules are summarized below.

– *Time to Peak Value*. The MCP signal must reach a maximum within a programmable time after the signal exceeds the impact threshold. The programmable range for this parameter is 8 μs to 2040 μs and its default value is 320 μs.
– *Pulse Width Max*. There is a maximum time that the MCP signal may exceed the impact threshold. The programmable range for this parameter is 1 to 255 ms and has a default value of 15 ms.
– *Pulse Width Min*. There is a minimum time that the MCP signal must exceed the impact threshold. This parameter is programmable in the range from 1 to 255 μs and has a default value of 100 μs.
– *Ratio*. The ratio of the integrated signal in the 50 sample waveform to the peak MCP value must exceed a programmable value that can range from 1 to 63, with a default value of 30.

If the MCP signal is within the values specified for all the parameters, the impact will be counted and the peak amplitude of the MCP and target signal levels will be stored. In

Fig. 9 MCP and target waveforms (*black lines*) recorded at the University of Colorado dust accelerator (Shu et al. 2012). Based on the in-beam diagnostics, the dust particle had a mass $m = 1.01 \cdot 10^{-12}$ g; speed $v = 1.83$ km s^{-1}, and carried a charge of $Q = 0.94$ fC. An analytic fit to these waveforms is also shown (*blue lines*)
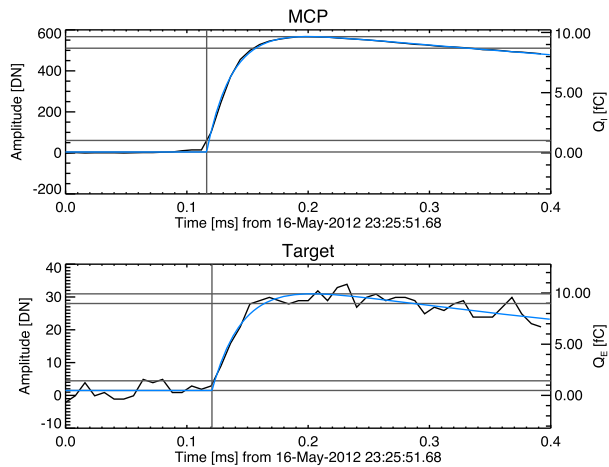

addition to storing the peak amplitudes of the MCP and target level for each valid impact, a selectable fraction of impact waveforms dictated by a programmable decimation factor are also stored, as described in Sect. 4.5.2. Finally, any waveforms that occur with very steep MCP signal slope will result in the production of a waveform regardless of the decimation factor; this helps with the positive identification of dust particles that do not originate from the surface of the Moon. This MCP slope parameter is programmable in the range from 1 to 65535 DN/sample, with a default value of 10000 DN/sample. Figure 9 shows an example of a valid MCP and target waveform pair recorded at the dust accelerator facility of the University of Colorado.
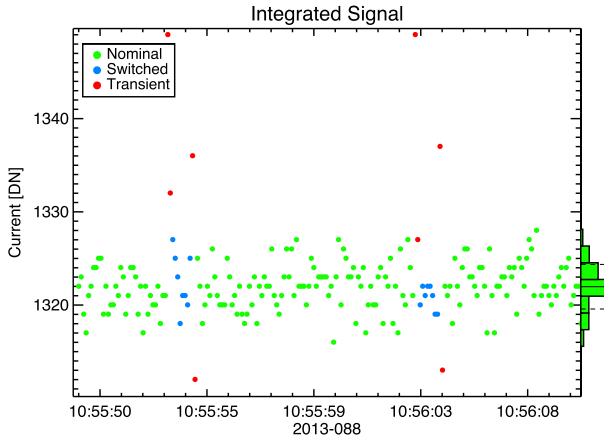
4.4.2 Integrator

In addition to passing the MCP signal through impact detection logic to determine if large impacts occur, the MCP signal is concurrently collected on the integrating capacitor, C_3 in Fig. 8. The purpose of this is to characterize the cumulative effect of small impacts that would otherwise pass undetected through the impact detection logic. This mode is used to search for the putative population of small grains suggested to be lofted over the terminator, with characteristics grain radii on the order of 0.1 μm (McCoy 1976). Such a population would yield a integrator signal which is over 2 orders of magnitude larger than the baseline measurement at 10 km over the lunar surface.

The charge on C_3 is sampled at a programmable rate from 0 (not sampled) to 255 ms with a default of 100 ms. The integrator science channel also has a reset that is pulsed for 1 ms at a programmable rate from 0 (not reset) to 255 ms with a default of 100 ms. This is to allow resetting the integrator capacitor at a faster rate without increasing the data volume for the channel. The intent is that the sample rate and reset rate will be set to values that are integer multiples of each other to keep them in sync. The FPGA takes two samples of C_3 each cycle to perform a correlated double sample. The first one is taken 1 ms after reset goes low to establish the zero level for the signal. The second one is taken after the programmed sample period has expired. The difference of the two is the measurement of the integrated current collected. Figure 10 shows the timing for the correlated double sample with both reset and sample periods set to their default values of 100 ms. Figure 11 shows an example
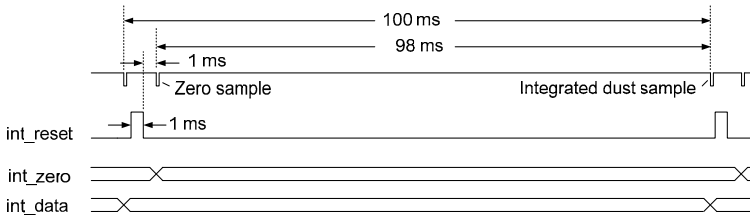
Fig. 10 The logic for sampling the integrator capacitor

Fig. 11 Integrator signal recorded at the University of Colorado dust accelerator showing no dust current (Nominal and Switched values are approximately the same). Green samples are taken during nominal grid configuration or -200 V, blue samples are taken during switched grid configuration of $+30$ V, and red samples are transients due to the switching. A large number density of grains would manifest itself in the integrator measurement by having the green, nominally biased points being significantly larger in magnitude than the blue, switched bias points

of an integrator signal recorded at the dust accelerator facility at the University of Colorado. The three types of integrator samples will be discussed in Sect. 4.5.2.

4.5 Modes of Operation

4.5.1 Standby

The LDEX instrument initially powers up into a known safe configuration with the high voltage power supply disabled. In this standby mode, the instrument produces housekeeping telemetry packets at a regular cadence, from which it is possible to monitor and assess the health and safety of the instrument. The aperture cover actuator firing, a one-time deployment of the instrument's protective cover, may only be performed in this mode. It is possible to monitor the science signals from the hemispherical target and MCP (including the integrated MCP measurement) while in this standby mode by sending the instrument the specific command to issue science packets; however, no science packets are issued by default in this mode. When the high voltage power supply is disabled the science data are of limited use, but this mode enabled the functional testing of LDEX prior to launch.

4.5.2 Science

Upon receipt of the proper command sequence, the instrument high voltages will be enabled. When this occurs, the programmable logic within the instrument brings up the high voltages in such a manner as to reduce the relative potential across the surfaces of the instrument and reduce the probability of arcing. When the high voltages are enabled, the instrument automatically begins producing integrated MCP science data packets at regular intervals. Fifty integrator measurements are contained within one integrated MCP science data packet.

Any dust impact with high enough MCP signal to cross the impact threshold with proper waveform characteristics (a valid impact) that occurs when the high voltages are enabled is counted and the amplitudes are recorded in instrument memory. The amplitude is calculated by subtracting the first sample of the 50 contained in the waveform buffer from the maximum value of the 50 samples. When 20 such impacts have been detected, the instrument produces a science data packet containing the 20 impact times and amplitudes. A 'short' packet is produced with less than 20 impacts if more than 60 seconds pass between the first impact recorded in an impact peaks packet and the 20th impact. In this case, the peak signal and impact time values in the science data packet will be padded with zeros as necessary to fill the data for any missing impacts.

The LDEX instrument will also produce impact waveform science data packets containing the signals from the hemispherical target and MCP during valid impacts. Due to limited bandwidth availability, the instrument is designed to send the waveform of only every Nth impact, a feature called decimation. The decimation factor defaults to 96, but is user programmable between 0 (no waveforms) and 255. Additionally, at a rate of no more than once per minute, the instrument will produce a waveform packet for any invalid impact, which consist of signals which exceed the impact threshold but fail the waveform shape parameter tests. The minimum time between invalid impact waveform packet production is programmable within the range of 0 (no invalid waveforms produced) to 255 min, with a default value of 1 min.

LDEX provides a range of noise characterization tools. The hemispherical grid maintains a nominal voltage of -200 V when the high voltage is enabled. For 1 second out of every 10 seconds, the FPGA switches the voltage to $+30$ V, making LDEX 'blind-to-dust' for 1 second. This allows for characterization of the background signal. Figure 11 shows this switching scheme in the integrator data with -200 V samples shown in green and $+30$ V samples shown in blue. The integrator is sensitive to this switching and records a transient signal for 0.2 seconds after each voltage switch. This results in two transient integrator points immediately following a voltage switch, shown in red in Fig. 11. Additionally, samples of the raw MCP and Target signals may be stored upon user request in 8 ms increments (1000 samples with a Δt of 8 μs).

4.6 Simulated Impact Tests

To test the LDEX instrument when high voltage is not or cannot be turned on, the instrument electronics include a signal injection feature. Upon command, the instrument will inject a charge into the MCP and target signal chain which will cause the instrument to detect an impact. There is no indication in the science data packets that test signals were used, so command logs must be used to eliminate these signals from the science data stream. A single impact test command will result in up to 31 signal injections separated by 100 ms. The actual number of test signals injected per command is programmable from 1 to 31, with a default of 20 injected signals per impact test command.

The voltage bias across the LDEX MCP can be adjusted by command. The 'high' side of the MCP is constantly maintained at −200 V, while the 'low' side can be adjusted from −600 V to −1200 V in 31 linear steps. The default MCP 'low' side bias is −1050 V, resulting in a voltage bias across the MCP of 850 V.

4.7 Safing Events

The LDEX instrument contains an autonomous safing mechanism that will disable the instrument high voltage power supply if the integrated MCP signal remains elevated above a programmable sun-safing threshold for 3 consecutive measurements (nominally, 300 ms elapsed time at the default integration time setting). This protects the instrument from damage due to the sun being in the instrument field of view while high-voltage is on. Beyond the autonomous safing feature, the command to disable the high voltage power supply may be issued at any time. When high voltages are disabled in either case, the instrument returns to its initial standby mode, from which it may be commanded back to science mode or powered off altogether. Any time the high voltage is turned off, including at instrument power off, the instrument will transmit one last impact peaks packet and one final integrated MCP packet. These packets will be short packets with zeros padding the unused fields.

4.8 Environmental Effects

The effect of background UV radiation on LDEX is photoelectron production and scattering into the MCP. Photoelectrons released from the target are returned by the radial electric field and have a negligible contribution to the CSA signal. The MCP detector is insensitive to photoelectrons because of the applied large negative bias. The LDEX geometry is designed to minimize specular reflection into the MCP. Ray-tracing simulations indicate that $< 2 \cdot 10^{-6}$ fraction of the entering UV photons will be detected by the MCP. The maximum UV field-of-view (FOV) of LDEX is 85° (half-angle). With a UV radiation background of $\simeq 1$ kR, which corresponds to $\simeq 2.5 \cdot 10^{10}$ s^{-1} Lyman alpha (Ly$_\alpha$) photons entering LDEX, less than $5 \cdot 10^4$ s^{-1} photons are detected. In order to maintain MCP performance, LDEX will be switched to standby mode for periods when the Sun is in the FOV. The effect of UV on LDEX has been tested using a calibrated Ly$_\alpha$ source. Solar wind ions do not affect LDEX as the Sun is excluded from the FOV during science mode. Solar wind electrons are prevented from entering LDEX by the −200 V bias applied on an entrance grid (Fig. 4). Acoustics and vibrations may cause temporal increase of the CSA noise; the overall performance of LDEX, however, is not affected as the MCP detector is insensitive to mechanical vibrations.

4.9 Test and Calibration

LDEX was tested and calibrated at the Dust Accelerator Facility at the University of Colorado (Shu et al. 2012). During its development phase tests were also done at the Dust Accelerator of the Max-Planck-Institute for Nuclear Physics, in Heidelberg, Germany (Mocker et al. 2011). Because the composition of the lunar ejecta is that of a mineral, we used olivine particles ($\rho = 3.32 \times 10^3$ kg m^{-3}) coated with platinum to calibrate the instrument. For reference, we also did tests with iron and nickel particles, which has been the dust analogs used to calibrate all dust detectors before LDEX (Dietzel et al. 1973; Göller and Grün 1989; Srama et al. 2004). To test and calibrate the instrument, LDEX was bombarded by submicron sized dust particles in a velocity range of 1–40 km s^{-1}. Figure 9 shows impact signals recorded at the accelerator.
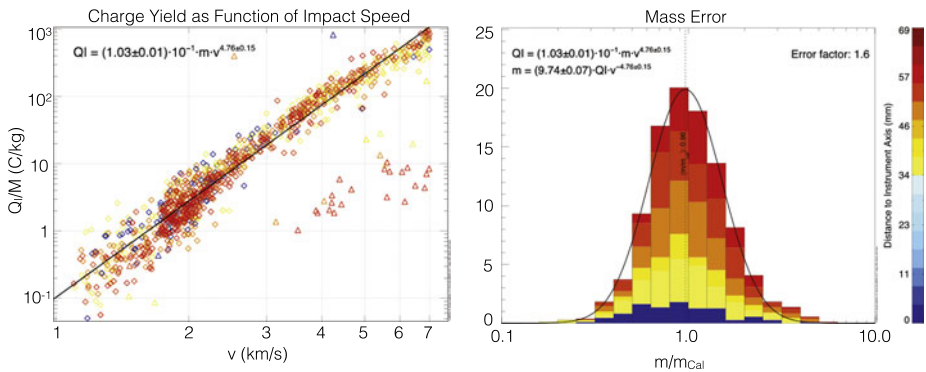
Fig. 12 LDEX impact calibration data using olivine particles (*left*), showing the specific ion yield (Q_I/m), as function of the speed of the dust particles. These tests were done at room temperature with an MCP bias of 850 V. The color code shows the distance of the impacts from the axis of symmetry of the instrument, indicating that the LDEX impact charge collection efficiency does not depend on the location of an impact. The uncertainty in mass determination is 1.6 (*right*) is also independent of the location of an impact

With the impact charge on the target (Q_e) and the MCP (Q_I) measured by LDEX, and the mass (m) and velocity (v) of the impacting dust particle reported by the accelerator, a calibration curve can be established for both the MCP and the target signals. This calibration curve was measured over a range of temperatures, MCP bias voltages, and radial positions. Figure 12 shows the calibration results for the specific impact charge measured on the MCP (Q_I/m) as function of the speed of impacting olivine particles. The resulting calibration equations for the MCP (Q_I) and the target (Q_e) recorded impact charges are

$$m = (9.74 \pm 0.07)Q_I v^{-4.76\pm0.15} \tag{2}$$

$$m = (5.31 \pm 0.06)Q_e v^{-4.34\pm0.21} \tag{3}$$

where the units are m [kg], $Q_{e,I}$ [C], and v [km s^{-1}]. The error factors are 1.6 and 4.2 for the mass determination based on Q_I and Q_e, respectively. The calibration of LDEX remains a continuing effort using its Engineering Model (EM), which is a close match of the LDEX Flight Model (FM). These calibrations are designed to improve the statistics, extend the range of impact velocities, and increase the number of impact locations on the target. In addition, the rise time of the MCP can be used to estimate the speed of the impacting dust particles. The results of the extended calibrations will be published in a followup paper, and the updates will also be available through the NASA PDS archive.

4.10 Data Products

When LADEE/LDEX data are received on the ground they are sent to the Science Operation Center (SOC) at the Laboratory for Atmospheric and Space Physics (LASP). The data are sent through a processing pipeline and archived in its original and processed formats. The data will be delivered to the NASA Planetary Data System (PDS) following PDS-4 standards containing both reduced and calibrated data. Table 1 shows the definitions of the PDS-4 standards, and Table 2 defines the LDEX data products.

Table 1 LDEX data processing levels

Product	Description
Packet	Telemetry data stream as received at the ground station, with science and engineering data embedded
Raw	Original data from an instrument. If compression, reformatting, packetization or other translation has been applied to facilitate data transmission or storage, those processes will be reversed so that the archived data are in a PDS approved archive format
Reduced	Data that have been processed beyond the raw stage but which are not yet entirely independent of the instrument
Calibrated	Data converted to physical units entirely independent of the instrument
Derived	Results that have been distilled from one or more calibrated data products (for example, maps, gravity or magnetic fields, or ring particle size distributions). Supplementary data, such as calibration tables or tables of viewing geometry, used to interpret observational data should also be classified as derived data if not easily matched to one of the other three categories

Table 2 LDEX data definitions

Product	Description	Level
Impacts	Amplitudes of individual impacts	Reduced
Integrated	Samples of integrated voltages from MCP	Reduced
Wave	Waveforms of individual impacts	Reduced
Housekeeping	Primary housekeeping telemetry	Calibrated
Mass	Calibrated mass of each impact	Calibrated
Integrated charge	Integrated charge from MCP	Calibrated

4.11 Classification of Impact Events

The MCP waveform capture can also be triggered by a number of spurious events, like cosmic ray hits or spacecraft discharging, for example. As part of the processing pipeline of downloaded data, for the identification of real dust impacts, each waveform pair is fitted by an analytical function to consistently identify their characteristics, using a non-linear list-squares fitting routine (Markwardt 2009):

$$w[t; t_0, C_0, C_1, C_2, \tau_0, \tau_1, \tau_2] = C_0 - \underbrace{\mathrm{H}(t_0 - t)\left[C_1 e^{-(\frac{t-t_0}{\tau_0})^2}\right]}_{\text{Image Charge}}$$

$$+ \underbrace{\mathrm{H}(t - t_0)\left[C_2\left(1 - e^{-\frac{t-t_0}{\tau_1}}\right)e^{-\frac{t-t_0}{\tau_2}} - C_1\right]}_{\text{Impact Charge}} \quad (4)$$

where the parameters represent the initial baseline C_0, the characteristic width of the image charge signal τ_0, the time of the impact t_0, the characteristic rise and decay times of the impact plasma generated signal τ_1 and τ_2, respectively. For consistency, these analytic fits are used to identify the amplitude of the signals Q_e, and Q_I, the rise time τ_{rise}, which is customarily defined as the time the signal rises from 10 % to 90 % of its peak value, and the signal-to-noise ratios of (a) the image-charge signal (if present) S/N_{im}, (b) the target sig-

Table 3 Requirements on waveforms

#	Requirement	MCP	Target
1	Signal-to-noise	$S/N_I > 5$	$S/N_e > 3.5$
2	Rise time [μs]	$20 < \tau_{rise}^I < 400$	$20 < \tau_{rise}^e < 400$
3	Decay time [ms]	$0.25 < \tau_2^I < 2$	$0.25 < \tau_2^e < 2$
4	Coincidence [μs]	$|t_0^e - t_0^I| < 50$	
5	$-\log_{10}(\frac{\sum(f-fit)^2}{amplitude^2})$	> 1	> 0
6	Image charge		$S/N_{im} > 2$

Table 4 Event classification. The list of requirements (1–6) are identified in Table 3. A ✓ indicates compliance with the MCP criteria while a ✓✓ indicates compliance with both the MCP and Target criteria. Criteria 5 is a quality of fit parameter, designed to removed waveforms that do not have a similar shape to the analytic fit. f is the 50 data points given by the LDEX collected waveform, *fit* is the fitted function, and *amplitude* is the amplitude of the signal

| Event	1	2	3	4	5	6
Dust impact with image charge	✓✓	✓✓	✓✓	✓✓	✓✓	✓
Dust impact	✓✓	✓✓	✓✓	✓✓	✓✓	
Candidate dust impact	✓	✓	✓		✓	
Candidate noise			✓			
Noise						

nal S/N_e, and (c) the MCP signal S/N_I. The noise levels are calculated from the first eight points that establish the baseline for each waveform. Identical fits are used for both the target and the MCP waveforms, with the only exception of setting $C_1 = 0$ for the MCP as it does not record the image charge induced by the charge a dust particle might carry before impacting the target. The characteristics of the waveforms based on these parameters are used to classify our recorded events. They are listed in Table 3. The classification of the recorded events is based on the combination of satisfied conditions. These are defined in Table 4. The classification scheme will be updated as needed, based on improved understanding of the behavior of LDEX throughout the mission.

5 Initial Results

The LDEX cover was deployed on Oct. 16, 2013 after a thorough testing of all functionalities of the instrument. Since the cover deployment, LDEX continues to make dust observations. Due to various mission and instrument constraints, LDEX is operating approximately 50 % of the time. LDEX had to accommodate the operational needs of the other instruments and avoid the Sun entering its field-of-view with the MCP high-voltages on. Through the end of 2013, LDEX recorded about 65000 MCP and target waveform pairs, including about 15000 unambiguous dust impact events. Figure 13 shows the waveforms for an early dust impact.

Based on our data to date, LDEX has identified the dust ejecta cloud that is maintained by micrometeoroid bombardment. As predicted, the density of the dust ejecta cloud rapidly

Fig. 13 MCP and target
waveforms (*black lines*) recorded
by LDEX in orbit around the
Moon on Nov. 12, 2013. Based
on our laboratory calibrations,
this dust particle had a mass
$m = 4.5 \cdot 10^{-15}$ kg. The analytic
fits (Eq. (4)) to these waveforms
are also shown (*blue lines*)
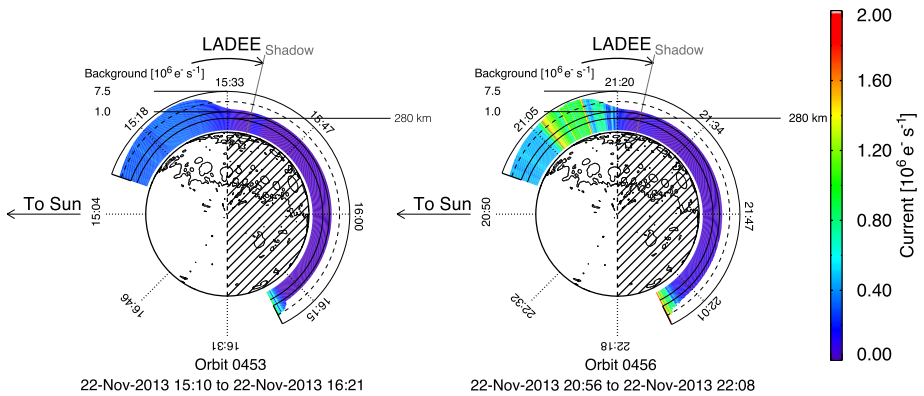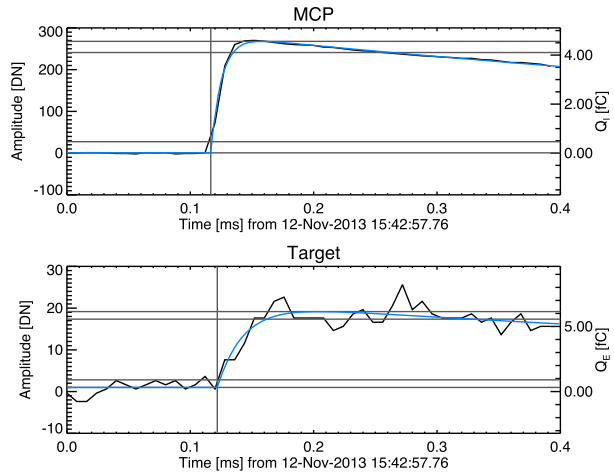
Fig. 14 The integrated MCP signal for two LADEE orbits. The radial extent of the color strips are proportional to the background measurements, and *the color-code* shows the value of the measured current

increases toward the surface and shows strong temporal variability, most likely related to the stochastic nature of the meteoroid impacts (Horányi et al. 2014; Kempf et al. 2014).

Figure 14 shows examples of the LDEX collective current measurements. As discussed in Sect. 4.5.2, LDEX measures the MCP total integrated signal (un-switched mode: E-field points to MCP), and the background (switched mode: E-field points to target) to derive the current = total integrated signal – background. This current is expected to be generated by the small particles lofted by plasma effects and low-energy ions from the lunar atmosphere. The background is dominated by UV light backscattered from the lunar surface, generating photoelectrons on the MCP detector itself (Sternovsky et al. 2014). The measured current exhibits a strong temporal variability, most likely due to the highly fluctuating nature of the direction of the polarization electric field of the solar wind. Large contributions from the lunar ionosphere are expected when $\hat{n} \cdot (\hat{v} \times \hat{B}) = -1$, where $\hat{n}$ is a unit vector pointing normal to aperture surface of LDEX, $\hat{v}$ and $\hat{B}$ are unit vectors along the solar wind flow, and the interplanetary magnetic field, respectively (Szalay et al. 2014; Poppe et al. 2014; Halekas et al. 2014). The expected difference in the density of low energy ions and lofted small

dust grains as function of altitude and longitude enables LDEX to search for the putative population of small dust grains.

References

S. Auer, in *Instrumentation*, ed. by E. Grün, B.A.S. Gustafson, S. Dermott, H. Fechtig (Springer, Berlin, 2001), pp. 387–438

O.E. Berg, F.F. Richardson, H. Burton, Lunar ejecta and meteorites experiment, in *Apollo 17: Preliminary Science Report*. NASA Special Publication, vol. 330 (1973), p. 16

A. Colaprete et al., The ladee ultraviolet/visible spectrometer. Space Sci. Rev. (2014, this issue)

J.E. Colwell, S. Batiste, M. Horányi, S. Robertson, S. Sture, Lunar surface: Dust dynamics and regolith mechanics. Rev. Geophys. **45**, 1–26 (2007)

D.R. Criswell, Horizon-glow and the motion of lunar dust, in *Photon and Particle Interactions with Surfaces in Space*, ed. by R.J.L. Grard Astrophysics and Space Science Library, vol. 37 (1973), p. 545

B.R. De, D.R. Criswell, Intense localized photoelectric charging in the lunar sunset terminator region, 1. Development of potentials and fields. J. Geophys. Res. **82**, 999 (1977)

G.T. Delory, R. Elphic, T. Morgan, T. Colaprete, M. Horányi, P. Mahaffy, B. Hine, D. Boroson, The Lunar Atmosphere and Dust Environment Explorer (ladee), in *Lunar and Planetary Institute Science Conference Abstracts*. Lunar and Planetary Institute Science Conference Abstracts, vol. 40 (2009), p. 2025

H. Dietzel, G. Eichhorn, H. Fechtig, E. Grun, H.-J. Hoffmann, J. Kissel, The HEOS 2 and HELIOS micrometeoroid experiments. J. Phys. E, Sci. Instrum. **6**, 209–217 (1973)

R.C. Elphic, G.T. Delory, E.J. Grayzeck, A. Colaprete, M. Horányi, P. Mahaffy, B. Hine, J. Salute, D. Boroson, The Lunar Atmosphere and Dust Environment Explorer (LADEE): T-minus one year and counting. LPI Contrib. **1685**, 3033 (2012)

R.C. Elphic, B. Hine, G.T. Delory, J.S. Salut, S. Noble, A. Colaprete, M. Horányi, P.R. Mahaffy, D. Boroson, The Lunar Atmosphere and Dust Environment Explorer (LADEE): T-minus 6 months and counting, in *Lunar and Planetary Institute Science Conference Abstracts*. Lunar and Planetary Institute Science Conference Abstracts, vol. 44 (2013), p. 3112

R.C. Elphic, G.T. Delory, B.P. Hine, P. Mahaffy, M. Horanyi, A. Colaprete, M. Benna, S. Noble, The lunar atmosphere and dust environment explorer mission. Space Sci. Rev. (2014)

P.D. Feldman, D.A. Glenar, T.J. Stubbs, K.D. Retherford, G. Randall Gladstone, P.F. Miles, T.K. Greathouse, D.E. Kaufmann, J.W. Parker, S. Alan Stern, Upper limits for a lunar dust exosphere from far-ultraviolet spectroscopy by LRO/LAMP. Icarus **233**, 106–113 (2014)

D.A. Glenar, T.J. Stubbs, J.E. McCoy, R.R. Vondrak, A reanalysis of the Apollo light scattering observations, and implications for lunar exospheric dust. Planet. Space Sci. **59**, 1695–1707 (2011)

D.A. Glenar, T.J. Stubbs, M. Hahn, Y. Wang, Search for a high altitude lunar dust exosphere using clementine navigational star tracker measurements. J. Geophys. Res., Planets (2014)

J.R. Göller, E. Grün, Calibration of the Galileo/Ulysses dust detectors with different projectile materials and at varying impact angles. Planet. Space Sci. **37**, 1197–1206 (1989)

E. Grün, H.A. Zook, H. Fechtig, R.H. Giese, Collisional balance of the meteoritic complex. Icarus **62**, 244–272 (1985). doi:10.1016/0019-1035(85)90121-6

E. Grün, H. Fechtig, M.S. Hanner, J. Kissel, B.-A. Lindblad, D. Linkert, D. Maas, G.E. Morfill, H.A. Zook, The Galileo dust detector. Space Sci. Rev. **60**, 317–340 (1992a)

E. Grün, H. Fechtig, J. Kissel, D. Linkert, D. Maas, J.A.M. McDonnell, G.E. Morfill, G. Schwehm, H.A. Zook, R.H. Giese, The Ulyssses dust experiment. Astron. Astrophys. Suppl. Ser. **92**, 411–423 (1992b)

E. Grün, M. Horányi, Z. Sternovsky, The lunar dust environment. Planet. Space Sci. **59**, 1672–1680 (2011). doi:10.1016/j.pss.2011.04.005

J.S. Halekas, A.R. Poppe, G.T. Delory, R.C. Elphic, V. Angelopoulos, M. Horányi, J. Szalay, Artemis observations and data-based modeling in support of ladee, in *45th Lunar and Planetary Science Conference* (2014)

M. Horányi, Z. Sternovsky, E. Gruen, R. Srama, M. Lankton, D. Gathright, The Lunar Dust Experiment (LDEX) on the Lunar Atmosphere and Dust Environment Explorer (LADEE) mission, in *Lunar and Planetary Institute Science Conference Abstracts*. Lunar and Planetary Institute Science Conference Abstracts, vol. 40 (2009), p. 1741

M. Horányi, Z. Sternovsky, M. Lankton, D. James, J. Szalay, K. Drake, A. Shu, A. Colette, E. Gruen, S. Kempf, R. Srama, A. Mocker, The dust environment of the Moon: Expectations for the lunar dust experiment (LDEX), in *Lunar and Planetary Institute Science Conference Abstracts*. Lunar and Planetary Institute Science Conference Abstracts, vol. 43 (2012), p. 2635

M. Horányi, S. Gagnard, D. Gathright, E. Grün, D. James, S. Kempf, M. Lankton, R. Srama, Z. Sternovsky, J. Szalay, The dust environment of the Moon as seen by the lunar dust experiment (LDEX), in *45th Lunar and Planetary Science Conference* (2014)

H. Iglseder, K. Uesugi, H. Svedhem, Cosmic dust measurements in lunar orbit. Adv. Space Res. **17**, 177–182 (1996). doi:10.1016/0273-1177(95)00777-C

S. Kempf, U. Beckmann, J. Schmidt, How the Enceladus dust plume feeds Saturn's E ring. Icarus **206**, 446–457 (2010). doi:10.1016/j.icarus.2009.09.016

S. Kempf, E. Grün, M. Horányi, D. James, M. Lankton, R. Srama, J. Szalay, Z. Sternovsky, Observations of the lunar dust exosphere with LDEX, in *45th Lunar and Planetary Science Conference* (2014)

A.V. Krivov, M. Sremčević, F. Spahn, V.V. Dikarev, K.V. Kholshevnikov, Impact-generated dust clouds around planetary satellites: Spherically symmetric case. Planet. Space Sci. **51**, 251–269 (2003)

H. Krüger, A.A. Krivov, D.P. Hamilton, E. Grün, Detection of an impact-generated dust cloud around Ganymede. Nature **399**, 558–560 (1999)

H. Krüger, A.V. Krivov, E. Grün, A dust cloud of Ganymede maintained by hypervelocity impacts of interplanetary micrometeoroids. Planet. Space Sci. **48**, 1457–1471 (2000)

S.G. Love, D.E. Brownlee, A direct measurement of the terrestrial mass accretion rate of cosmic dust. Science **262**, 550 (1993)

P.R. Mahaffy, R. Richard Hodges, M. Benna, T. King, R. Arvey, M. Barciniak, M. Bendt, D. Carigan, T. Errigo, D.N. Harpold, V. Holmes, C.S. Johnson, J. Kellogg, P. Kimvilakani, M. Lefavor, J. Hengemihle, F. Jaeger, E. Lyness, J. Maurer, D. Nguyen, T.J. Nolan, F. Noreiga, M. Noriega, K. Patel, B. Prats, O. Quinones, E. Raaen, F. Tan, E. Weidner, M. Woronowicz, C. Gundersen, S. Battel, B.P. Block, K. Arnett, R. Miller, C. Cooper, C. Edmonson, The neutral mass spectrometer on the lunar atmosphere and dust environment explorer mission. Space Sci. Rev. (2014). doi:10.1007/s11214-014-0043-9

C.B. Markwardt, Non-linear least-squares fitting in Idl with Mpfit, in *Astronomical Data Analysis Software and Systems XVIII*, ed. by D.A. Bohlender, D. Durand, P. Dowler. Astronomical Society of the Pacific Conference Series, vol. 411 (2009), p. 251

J.E. McCoy, Photometric studies of light scattering above the lunar terminator from Apollo solar corona photography, in *Lunar and Planetary Science Conference Proceedings*, ed. by R.B. Merrill. Lunar and Planetary Science Conference Proceedings, vol. 7 (1976), pp. 1087–1112

J.E. McCoy, D.R. Criswell, Evidence for a high altitude distribution of lunar dust, in *Lunar and Planetary Science Conference Proceedings*. Lunar and Planetary Science Conference Proceedings, vol. 5 (1974), pp. 2991–3005

A. Mocker, S. Bugiel, S. Auer, G. Baust, A. Colette, K. Drake, K. Fiege, E. Grün, F. Heckmann, S. Helfert, J. Hillier, S. Kempf, G. Matt, T. Mellert, T. Munsat, K. Otto, F. Postberg, H.-P. Röser, A. Shu, Z. Sternovsky, R. Srama, A 2 MV Van de Graaff accelerator as a tool for planetary and impact physics research. Rev. Sci. Instrum. **82**(9), 095111 (2011)

D.L. Murphy, R.R. Vondrak, Effects of levitated dust on astronomical observations from the lunar surface, in *Lunar and Planetary Institute Science Conference Abstracts*. Lunar and Planetary Institute Science Conference Abstracts, vol. 24 (1993), pp. 1033–1034

M.A. Pelizzari, D.R. Criswell, Differential photoelectric charging of nonconducting surfaces in space. J. Geophys. Res. **83**, 5233–5244 (1978). doi:10.1029/JA083iA11p05233

A.R. Poppe, J.S. Halekas, J.R. Szalay, M. Horányi, G.T. Delory, Model-data comparisons of ladee/ldex observations of low-energy lunar dayside ions, in *45th Lunar and Planetary Science Conference*, vol. 1393 (2014)

J.J. Rennilson, D.R. Criswell, Surveyor observations of lunar horizon-glow. Moon Planets **10**, 121–142 (1974). doi:10.1007/BF00655715

A. Shu, A. Collette, K. Drake, E. Grün, M. Horányi, S. Kempf, A. Mocker, T. Munsat, P. Northway, R. Srama, Z. Sternovsky, E. Thomas, 3 MV hypervelocity dust accelerator at the Colorado center for lunar dust and atmospheric studies. Rev. Sci. Instrum. **83**(7), 075108 (2012). doi:10.1063/1.4732820

F. Spahn, J. Schmidt, N. Albers, M. Hörning, M. Makuch, M. Seiß, S. Kempf, R. Srama, V. Dikarev, S. Helfert, G. Moragas-Klostermeyer, A.V. Krivov, M. Sremčević, A.J. Tuzzolino, T. Economou, E. Grün, Cassini dust measurements at Enceladus and implications for the origin of the E ring. Science **311**, 1416–1418 (2006). doi:10.1126/science.1121375

R. Srama, T.J. Ahrens, N. Altobelli, S. Auer, J.G. Bradley, M. Burton, V.V. Dikarev, T. Economou, H. Fechtig, M. Görlich, M. Grande, A. Graps, E. Grün, O. Havnes, S. Helfert, M. Horányi, E. Igenbergs, E.K. Jessberger, T.V. Johnson, S. Kempf, A.V. Krivov, H. Krüger, A. Mocker-Ahlreep, G. Moragas-Klostermeyer, P. Lamy, M. Landgraf, D. Linkert, G. Linkert, F. Lura, J.A.M. McDonnell, D. Möhlmann, G.E. Morfill, M. Müller, M. Roy, G. Schäfer, G. Schlotzhauer, G.H. Schwehm, F. Spahn, M. Stübig, J. Svestka, V. Tschernjawski, A.J. Tuzzolino, R. Wäsch, H.A. Zook, The Cassini cosmic dust analyzer. Space Sci. Rev. **114**, 465–518 (2004). doi:10.1007/s11214-004-1435-z

M. Sremčević, A.V. Krivov, F. Spahn, Impact-generated dust clouds around planetary satellites: Asymmetry effects. Planet. Space Sci. **51**, 455–471 (2003)

S.A. Stern, The lunar atmosphere: History, status, current problems, and context. Rev. Geophys. **37**, 453–492 (1999). doi:10.1029/1999RG900005

Z. Sternovsky, P. Chamberlin, M. Horanyi, S. Robertson, X. Wang, Variability of the lunar photoelectron sheath and dust mobility due to solar activity. J. Geophys. Res. **113**(12), 10104 (2008). doi:10.1029/2008JA013487

Z. Sternovsky, S. Gagnard, D. Gathright, E. Grün, D. James, S. Kempf, M. Lankton, M. Horányi, R. Srama, J. Szalay, Modeling the uv signal scattered into the lunar dust experiment (ldex) from the surface, in *45th Lunar and Planetary Science Conference* (2014)

J.R. Szalay, M. Horányi, A.R. Poppe, J.S. Halekas, Ldex observations and correlations with artemis measurements, in *45th Lunar and Planetary Science Conference* (2014)

A.D. Taylor, Earth encounter velocities for interplanetary meteoroids. Adv. Space Res. **17**, 205–209 (1996). doi:10.1016/0273-1177(95)00782-A

H.A. Zook, J.E. McCoy, Large scale lunar horizon glow and a high altitude lunar dust exosphere. Geophys. Res. Lett. **18**, 2117–2120 (1991). doi:10.1029/91GL02235

The Lunar Laser Communication Demonstration: NASA's First Step Toward Very High Data Rate Support of Science and Exploration Missions

Don M. Boroson · Bryan S. Robinson

Abstract Future NASA missions for both Science and Exploration will have needs for much higher data rates than are presently available, even with NASA's highly-capable Space- and Deep-Space Networks. As a first step towards this end, for one month in late 2013, NASA's Lunar Laser Communication Demonstration (LLCD) successfully demonstrated for the first time high-rate duplex laser communications between a satellite in lunar orbit, the Lunar Atmosphere and Dust Environment Explorer (LADEE), and multiple ground stations on the Earth. It constituted the longest-range laser communication link ever built and demonstrated the highest communication data rates ever achieved to or from the Moon.

This report will summarize the main achievements of LLCD and put them in context of the near-term and long-term communications goals of NASA space missions.

Keywords Free-space optical communications · Laser communications · Lasercom · Photon counting receiver · Lunar laser communications demonstration · Moon · Lunar

1 Introduction

The highest resolution maps to date of Mars are based on thousands of photographs taken by orbiting American and European spacecraft. These have resolutions of 20–100 meters per pixel. There are also a number of photographs of surface features taken by, for example, the HiRISE camera on the Mars Reconnaissance Orbiter, which can resolve details down to 0.3 meters. A quick calculation, though, indicates that, even with the recently demonstrated

D.M. Boroson (✉) · B.S. Robinson
MIT Lincoln Laboratory, Lexington, MA, USA
e-mail: boroson@ll.mit.edu

B.S. Robinson
e-mail: brobinson@ll.mit.edu

6 Mbps data delivery from Mars (Shambayati et al. 2006) (which was not at the max range), an 8 bit map of the entire Martian surface at that 0.3 meter resolution would take over 60 years to transmit back.

There is a similar story for manned space exploration. The in-development Orion Multi-Purpose Crew Vehicle will carry humans to the Moon, asteroids, and perhaps even Mars. Although it could conceivably also carry communications equipment similar to the large science relay satellites, mass and size constraints keep its links to a very few megabits per second up and down, from the Moon, Bergin (2009) with R^2 losses keeping data rates much lower as the distances grow. There is no question that high definition and perhaps even 3-D video will be desired for these missions' downlinks, with good video uplinks, as well as near-continuous web-like connectivity for the astronauts and the mission.

For over thirty years, NASA has been developing free-space optical communications technologies to try to achieve the kinds of high duplex data rates that will be needed, as well as keeping space hardware with low SWaP (Size, Weight, and Power).

As a first major step, NASA designed, built, and demonstrated the Lunar Laser Communication Demonstration (LLCD). This system consisted of a space terminal, the Lunar Lasercom Space Terminal (LLST, Robinson et al. 2011), and a primary ground terminal, the Lunar Lasercom Ground Terminal (LLGT, Fitzgerald 2011), a transportable system which was stationed at White Sands, NM for the mission. In order to increase the amount of time of operations in the face of the short LLCD mission (one month) and the possibility of clouds, the program also included two alternate terminals, the Lunar Lasercom OCTL Terminal (LLOT, Wilson et al. 2012), residing at the NASA Jet Propulsion Laboratory's Optical Communications Telescope Laboratory at Table Mountain Facility in California, and the Lunar Lasercom Optical Ground System (LLOGS, Sans et al. 2012), residing at European Space Agency's OGS on Tenerife, the Canary Islands. The space terminal was a payload on the Lunar Atmospheric Dust and Environment Explorer (LADEE) spacecraft (Elphic et al. 2014). The operation of the space and ground terminals were all coordinated from the Lunar Lasercom Operations Center (LLOC) which resided at the MIT Lincoln Laboratory in Lexington, MA. The LLST, LLGT, LLOC, and overall LLCD system were all designed, built, and operated by teams from the MIT Lincoln Laboratory. The LLOT was designed and operated by the Jet Propulsion Laboratory and the LLOGS was designed and operated by the European Space Agency. The entire LLCD program was overseen by NASA Goddard Space Flight Center, and the LADEE spacecraft was designed, built, and operated by the NASA Ames Research Center.

The LLCD system was highly successful in meeting its goals of performing reliable high-rate links both up and down, plus demonstrating that system needs for operations of such a system were essentially the same as those of radio links, and that the large delivered data volumes were useful.

2 Brief Introduction to Lasercom

Optical communications (also known as free-space optical communications, laser communications, or just lasercom) is the use of the optical frequencies of the electromagnetic spectrum instead of the radio frequencies. These can be with wavelengths as short as ultraviolet or visible, as long as 2–10 microns, or, more typically, in the near- and short-wave infrared bands between 1 and 1.5 microns, where the fiber telecom industry has developed much relevant technology. Such terrestrial technology includes the very high-speed modulation that is possible in these optical bands.

There are direct optical analogs for every part of a communication system: a telescope instead of an antenna (possibly duplex), waveguides for carrying the signal (optical fibers), optical amplifiers and pre-amplifiers, sources, modulators, low-noise receivers, and so on. The big difference is the width of the beam, which, for a fixed aperture size, is known to have a diffraction-induced width proportional to the wavelength. Thus, lasercom beams can be as much as 10,000 times narrower than radio beams. This is good from the point of view of efficiently delivering power, but creates an engineering task of pointing and stabilizing the beams. After many years of working on these problems, however, the industry has devised a number of successful approaches.

Unlike the radio bands, the optical bands are unregulated, although care must be taken if the lasers are bright and they aim near airplanes or satellites with optical sensors. Thus, if adequate power can be transmitted and if modem hardware is adequately capable, extremely high data rates can be achieved. The other possible tradeoff would be to achieve the same data rates as radio systems, but design the terminal to be much smaller. Typically, lasercom systems try to achieve a little of each.

LLCD was designed to achieve higher data rates from lunar orbit than ever achieved before, while keeping both the space and ground terminals somewhat smaller than even much less capable radio systems.

3 LLCD System Overview

3.1 The System (see Fig. 1 and Table 1)

The LLCD lasercom links operated in the 1.5 micron band, and supported 4PPM (pulse position modulation) uplinks at 10 and 20 Mbps; 16PPM downlinks at selectable rates from
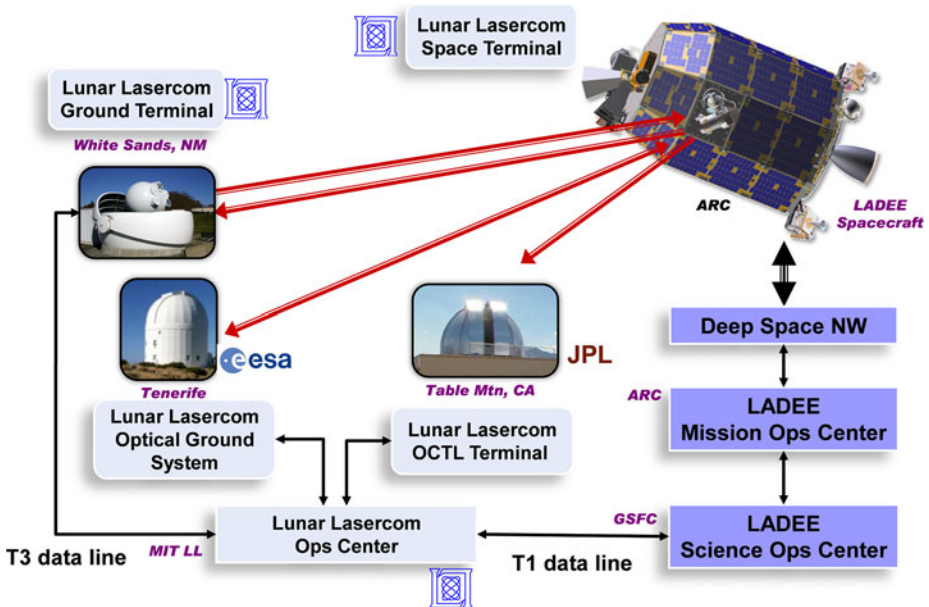

Fig. 1 LLCD system block diagram

Table 1 LLCD system block diagram

System	
Uplink data rate	10 or 20 Mbps
Uplink format	4-ary PPM
Downlink data rate	622, 311, 155, 78, 39 Mbps
Downlink format	16-ary PPM
Space terminal	
Total mass	~ 30 kg
Total power	~ 90 W
Telescope	10 cm, duplex
Uplink receiver	Pre-amplified direct detection
Downlink transmitter	0.5 W EDFA amplifier
Gimbal	2-axis
Tracking sensors	Inertial sensors plus nutating fiber comm receiver
Ground terminal	
Uplink	4 @ 15 cm
Downlink	4 @ 40 cm
Uplink transmitter	4 @ 10 W
Downlink receiver	Superconducting nanowire single photon detecting arrays

39 Mbps up to 622 Mbps; an uplink acquisition signal square-wave modulated at 1 Khz; and the capability to measure the round-trip Time of Flight (TOF) continuously with instantaneous errors somewhat less than 200 psec. As in most free-space lasercom systems, each of the two terminals of LLCD used the position of the received beam from the other terminal as its pointing reference.

3.2 Lunar Lasercom Space Terminal

The LLST has been described in detail in Robinson et al. (2011), Elgin et al. (2011), Boroson (2012), and Boroson et al. (2014). It consisted of an optical module mounted on an external panel of LADEE (See Figs. 1 and 2) and two electronics modules, the modem and the Controller Electronics (CE). The optical module was based on a duplex 10 centimeter reflective telescope that produced a ~ 15 µrad beam. Optical fibers coupled the optical module to the modem where nominally 0.5 W downlink transmitted optical waveforms were generated and uplink received optical waveforms were processed (Robinson et al. 2011). Control for the optical module and modem as well as command and telemetry interfaces to the spacecraft were provided by the CE. There was also a 40 Mbps interface between the LADEE data buffer and the downlink side of the modem, as well as data connections from the modem to the CE.

3.3 Ground Terminals

The primary ground terminal, the LLGT, has been described in detail in Fitzgerald (2011) and Boroson (2012). Its main features were its array of four 15 cm uplink telescopes, each transmitting a 10 W replica of the uplink which was delivered via single-mode fiber (Caplan et al. 2012) and tracking the downlink; its array of four 40 cm downlink telescope (Boroson et al. 2004), each coupled via multi-mode, polarization-maintaining fiber (Grein 2011) to an

array of superconducting nanowire single photon detectors (Dauler et al. 2007; Willis et al. 2012); a single gimbal carrying all 8 telescopes in an environmentally-controlled enclosure; and a nearby control room containing the cryogenic nanowire systems, the rest of the modem electronics and opto-electronics, the various control computers, and the local operations center.

The LLGT was capable of performing all the uplink, downlink, and TOF functions in the LLCD system in real time. Its design and performance were described in more detail in Murphy et al. (2014). Its form factor allowed it to be transportable, and it was ultimately brought to White Sands. (See Fig. 3.)

The LLOT was based on the OCTL system with its 1 meter-diameter telescope (Wilson et al. 2012). It included uplink acquisition signals from 6 subapertures, with a total of 60 watts average power, and coupled its downlink via multi-mode fibers to a superconducting nanowire photon-counting array. The terminal was capable of supporting uplink acquisition and tracking, and could receive downlink rates up to 78 Mbps with software post-processing. Its design and performance were described in more detail in Biswas et al. (2014). (See Fig 4.)

The LLOGS was based on the OGS system with its 1 meter-diameter telescope (Sans et al. 2012). It included uplink acquisition and communications signals from 3 outrigger telescopes with a total of 60 watts average power, and coupled its downlink via multi-mode

Fig. 2 The Lunar Lasercom Space Terminal, optical module. For scale, the aperture diameter is 10 centimeters
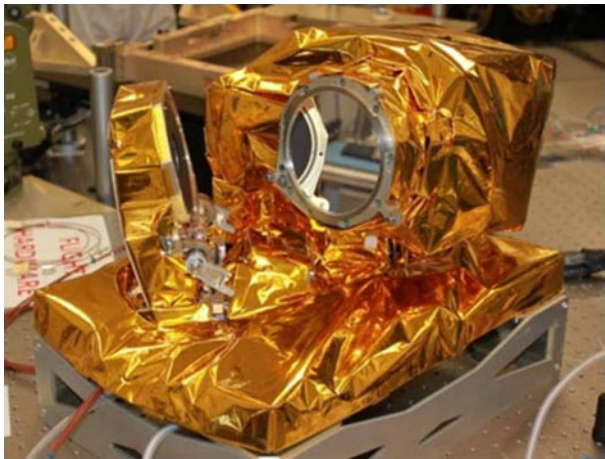
Fig. 3 The Lunar Lasercom Ground Terminal at site (White Sands, NM). The four smaller uplink telescopes can be seen grouped above the four 40 cm downlink telescopes

Fig. 4 The Lunar Lasercom OCTL Terminal (OCTL, at Table Mtn, CA)

Fig. 5 The Lunar Lasercom OGS Terminal (OGS, at Tenerife, Spain)

fibers to a photo-multiplier tube array. The terminal was capable of supporting uplink acquisition and tracking plus communications, and could receive downlink data at 39 Mbps with a hardware post-processor. Its design and performance were described in more detail in Sodnik et al. (2014) and Arnold et al. (2014). (See Fig. 5.)

3.4 Operations Center

The LLOC resided at MIT Lincoln Laboratory, and consisted of over one dozen desktop computers performing functions of command and control for the LLST, of monitoring telemetry from the LLST either over the RF path or the high-rate optical downlink path, of monitoring selected health and performance signals from each of the ground terminals, of monitoring weather conditions and predictions for the 3 sites, and monitoring telemetry and orbital information from LADEE. The computers and voice services were connected via ground lines to each of the ground terminals, to the LADEE Science Operations Center at Goddard Space Flight Center and to the LADEE Mission Operations Center at Ames Research Center.

4 Preparations, Launch, and Cruise

The LLST was designed, fabricated, integrated, tested, and space qualified at MIT Lincoln Laboratory. Integration onto LADEE, the launch, the phasing loops, and insertion into lunar orbit have been described elsewhere in this special issue (Elphic et al. 2014).

Near the apogees of loops 2 and 3, LLCD was provided a short window for checkout. Power up and internal checkouts plus the ground control infrastructure all operated correctly. The LLCD team was even able to attempt an initial pointing and acquisition session during one of the opportunities. Since the LLGT was partly cloudy during that period, the LLOT was used, and its uplink was successfully acquired and tracked. A downlink beam was similarly acquired and tracked. No lasercom data transfer was attempted. The primary spacecraft-to-LLST post-launch pointing biases, although reasonably small, were learned and subsequently compensated for on all the in-orbit passes.

5 Orbit, Conditions, and Operations Planning

The first month of the on-orbit LADEE mission took place in a near-circular low-inclination retrograde orbit approximately 250 km above the surface and lasting about 2 hours. This first month was divided into an alternating set of 4 and 3 day blocks. Each "4 Lunar Day Block (4LDB—a Lunar Day defined to be the time duration between moon rises)" was dedicated to LLCD operations during the approximately 19 hours that LADEE was visible by at least one of the 3 ground terminals. The 19 hour day started approximately one hour later each subsequent day as the Moon traveled in its monthly orbit around the Earth. In between the 4LDB's were 3-day periods dedicated to the checkout and commissioning of the LADEE science payloads. At the end of this month, LADEE was lowered to approximately 50 km and was dedicated solely to its main science mission. The LLCD mission's total duration ended up being 15 Lunar Days (Robinson et al. 2014).

The geometry of the orbit was such that LADEE was in front of the Moon for a little over an hour each orbit. The LADEE navigation team kept an up to date orbit model upon which LADEE in-view periods from Earth were predicted. Outputs from this orbital model were also sent regularly to the three ground terminals for their open-loop pointing needs. LADEE had allocated a (conservative) 39 watt-hours per orbit of energy usage for the LLST, since its battery was only being recharged about half of each orbit. Pre-launch calculations predicted that amount of energy would be able to power nominal LLST operations for 20–25 minutes. Thus, the joint LLCD/LADEE team had a certain freedom in the placement of the 25 minute pass time somewhere in the approximately one hour in-view time.

6 Pointing, Acquisition, and Tracking

The detailed design and operations of the LLCD pointing, acquisition, and tracking (PAT) systems and protocols have been described elsewhere (Burnside et al. 2011).

Using the most recent LADEE orbit knowledge, the ground terminal would transmit its beam to follow the moving spacecraft starting a few minutes before the LLST was to be powered up. The LLST used its knowledge of the location of the selected ground site plus one-second updates of attitude information sent to it by LADEE in order to initially point its telescope. Its acquisition detector was thus ready to detect an uplink if it were there.

As suggested above, after the very first (phasing loop) pass where the initial pointing bias was learned and corrected, the LLST was able to detect and pull in the uplink beam as soon as its gimbal had slewed to the proper position. Although conservative protocols had been devised and tested before launch in case either the ground terminal or the LLST were not able to point as well as hoped, it was found that both the ground terminals' uplinks (with appropriate pre-pass star calibrations and appropriate beam-width selections) and the

space terminal's pointing (even though it was mounted some distance from the LADEE star trackers) were good enough to produce instantaneous uplink detection and acquisition once the LLST gimbal completed slewing, and then, after a 1.3 seconds moon-Earth propagation time, instantaneous downlink detection and lockup. Once the ground terminal locked onto and tracked the downlink, it further refined its uplink pointing.

7 Communications and Ranging Functions

The LLCD data signals, both uplink and downlink, were constructed by multiplexing so-called transfer frames from multiple subchannels into a single time-division multiplexed (TDM) frame. These were block-encoded with data interleaved over approximately one second. The pairing of channel data interleaving with powerful coding (rate ½) has been found to be a highly robust means with which to combat even deep fading due to atmospheric turbulence (Boroson 2008; Barron and Boroson 2006).

Uplink streams were completely demodulated and decoded in the LLST modem (Stevens et al. 1999, 2014). The uplinks came from a combination of LLST terminal commands which were created at the LLOC (and were then passed by the LLST modem to the CE,) an arbitrary data stream from an Ethernet user port which was connected to the LLOC, and pseudonoise patterns to fill up the link.

Both the LLGT and LLOGS could transmit uplink data at either 10 or 20 Mbps. LLGT could send arbitrary data and the LLOGS could send a repeated fixed frame which was adequate for demonstrating the quality of the link by monitoring the LLST-measured and telemetered uplink Codeword Error Rates. The LLOT transmitted the uplink acquisition wavelength only. (The LLOGS and LLOT joined the LLCD program too late to be able to include all the functions.)

The downlink data sources included: the 2.7 Mbps LLST telemetry stream multiplexed with the data received on the uplink user channel and which provided a loop-back configuration for various demonstrations; a 38.55 Mbps stream from the LADEE buffer, which could be configured by LADEE to download arbitrary data partitions; and the rest of the downlink which was filled with encoded and framed pseudonoise patterns for assessing the performance of the entire link. The downlink could thus be selected to include 1, 2, 4, 8, or 16 parallel subchannels (corresponding to 39, 78, 155, 311, and 622 Mbps), with the lower data rates able to operate in even the poorest link conditions.

The LLGT had the capability to receive the entire downlink at any rate and decode any four selectable subchannels in real time using an FPGA implementation. The LLOT could receive either of the two lowest rates and could decode them off-line in a software-based system. The LLOGS could receive the lowest rate and could decode it off-line in a hardware-based system.

Thanks to the uplink and downlink rate designs being multiples of each other, the LLST modem used the derived uplink slot and frame clock as the reference for the downlink timing. Thanks to this feature, a ground terminal with both an uplink and downlink communications capability could measure the time delay between each uplink frame and the paired downlink frame that returned approximately 2.6 seconds later. This continuous (at 20 Khz) measurement of two-way Time of Flight (TOF) was a novel use of such a high-rate duplex link for Deep Space (or any) satellites. With the proper processing (removing the various known system biases) this measurement can produce knowledge of the position and orbit details of the spacecraft to a centimeter or better. Although LADEE did not make real-time use of this capability, the measurements were taken whenever there was a duplex link running.

8 Demonstrations and Performance

Of course, a major goal of LLCD was "just" to demonstrate that lasercom could be done from a lunar spacecraft to the ground. This was accomplished the first time it was attempted and on nearly all the passes through the month.

However, the real goal of LLCD was to show that lasercom had the following useful properties:

1. An optical space terminal can be integrated on and then flown on an operational spacecraft, and then provide useful services.
2. Lasercom can deliver high data rates from the Moon and beyond.
3. Optical beams can be acquired and tracked regularly, quickly and in many orbital and atmospheric conditions.
4. Optical links can be run error-free, on both the uplinks and downlinks through the turbulent atmosphere.
5. Optical links can be run error-free, on both the uplinks and downlinks, in daytime and nighttime, near the sun, as well as high and low in the sky.
6. Optical link operations can be run with a very small team.
7. Clouds can be dealt with operationally by preparing and coordinating a ground terminal network.
8. Intermittent clouds can be defeated by using a fast-re-acquiring system that uses a repeat-request protocol such as Disruption Tolerant Networking.
9. A capable optical ground terminal can be built from an array of small telescopes that can be transportable.
10. Highly-efficient high data rate optical reception can be achieved, even through turbulence, using high-speed photon-counters with error-correction codes and channel data interleavers.
11. Multiple error-free HD video streams can be carried over such links, in addition to data files.
12. Optical links can be used to carry command, control, and telemetry signals for the lasercom system itself.
13. Optical links can be brought up, operated, and reconfigured without the need for radio connectivity.
14. High-speed lasercom signals can be used to make continuous, real-time ranging estimates with centimeter-class accuracy.

All of these goals were achieved with LLCD.

1—Although LADEE was a completely new, very small satellite with only moderate capabilities for power and thermal control, the LLCD Space Terminal was successfully designed to fly on it. Its modularity allowed it to be placed throughout LADEE, aiding in balancing. It survived the launch and multiple rocket firings on the way to lunar orbit. It was successfully operated in the tough thermal environment of low lunar orbit, and was able to sustain links for 20–30 minutes per orbit on battery power.

2—The LLCD system regularly achieved error-free uplinks at either 20 Mbps or 10 Mbps, and also regularly was able to achieve downlinks at 622 Mbps, although many "passes" were operated at 311 Mbps so as to preserve energy by running the laser transmitter at half power. Lower data rates were sometimes used in particularly turbulent conditions. Such performance had been predicted in pre-launch modeling. The alternate terminals were successful in demonstrating their lower data rates.

3—After the first very few passes where pointing biases were learned and where a few space-ground (LLGT) configuration details were refined, then after acquisition, the system

locked up every time with error-free performance both up and down. In most cases, with the uplink already illuminating the spacecraft, the Space Terminal was powered up and then slewed to its calculated position. Immediately upon reaching that position, the uplink was detected and locked up, and the duplex link was operational within seconds after that. (The one-way time of flight of the beam was about 1.3 seconds.)

4—With the primary ground terminal, uplinks and downlinks ran error free in nearly all atmospheric conditions. That is, the links were established and, 20 minutes later or so, when the links were powered down, the error totals on both the uplink and downlink showed zero counts. These counts were available because the decoders knew whether they had succeeded or not with extremely high probability.

5—With the primary ground terminal, links were error free at all times of the day and night. In fact, during the one pass with the sun near the Moon in the sky, links were preserved with Sun-Earth-Probe angles as low as 3 degrees. (There was essentially only one chance during the month when geometries were such that such a test could be run.) Also, the link continued to work as the Moon got lower and lower in the sky, with one pass down to 3.8 degrees elevation.

6—During the first several passes, many people from the Ground and Space Terminal teams—mechanical and thermal engineering, electrical engineering, and communications—stayed in the Operations Center to assist with any necessary initial debugging efforts. However, after only a few days, the operations had become so routine that only two operators at the LLGT and three operators (Director plus liaisons with the spacecraft team and the LLGT) in the LLOC were required. There is no doubt that operations could have been done with even fewer.

7—With the potential for cloud cover during the short one-month mission, the LLCD program added two alternate ground terminals, as described above. The times when both the LLGT and the LLOGS could see LADEE were limited, but of those, the availability of two terminals definitely increased the number of possible passes. The LLGT and LLOT had near complete time overlap, and so several times every day, there was the opportunity to choose, at the last minute, the terminal with better cloud conditions.

On several occasions during the month, it was found that cloud conditions changed during the pass. Thus, with only a modicum of warning to the terminal on standby, the Space Terminal was commanded to drop the link being clouded out, slew to the new terminal, and successfully lock up and operate, all in seconds. This demonstrated break-before-make handover will be important in future space-to-ground systems with capable ground networks.

8—Near the end of the month, a team from Goddard SFC plus the MIT Lincoln Laboratory programmers created the capability to send files from Goddard to the LLOC to the LLGT, up over the Moon, and back to Goddard, using end-to-end Delay/Disruption Tolerant Networking. The details of this demo were given in Israel and Cornwell (2014), but we can say here that the demonstration was quite successful in pushing files over the link. In fact, one of the passes selected for this demo experienced scattered clouds over White Sands. Although the link came and went, the DTN protocol successfully pushed the data through whenever the links were up. There is no doubt that such a capability will make some kinds of future laser communication functions be successful even in the face of partial clouds.

9—The LLGT was designed with an array of transmit telescopes and an array of receive telescopes, all configured on a single gimbal. The non-coherent uplink transmissions and multi-mode fiber-coupled photon-counted downlinks worked very well (and as predicted by theory and modeling) in achieving these high data rates, especially with the very small space transmitter. This was all designed so that it could be taken apart and reassembled quickly, making it fully transportable. Future ground infrastructures will likely be a combination of fixed-location terminals and transportable ones.

10—LLCD demonstrated what had been known through theory and simulation—that a powerful, medium-rate code paired with a long channel-data interleaver would allow error-free performance even through appreciable fading due to turbulence. In addition, the ground terminals used photon-counting detectors behind multi-spatial-mode collectors, allowing operation through turbulence without adaptive optics. Error-free performance was demonstrated in nearly all conditions.

11—Using the error-free, high-rate up and downlinks, LLCD was able to transmit arbitrary signals (via an Ethernet port) up to the Space Terminal, and then to loop the demodulated bits back to the ground. The 20 Mbps uplink was thus able to carry up to four HD video signals and loop them back. Although future systems will likely not use the loop-back configuration of this demonstration, the achievement showed the ability to send error-free HD videos either up or down. Both pre-recorded and live videos were sent in this fashion, to the great amusement of visitors to the LLOC.

The fast links were also used to demonstrate error-free transmission of large data files both on the uplink (to the Controller) and on the downlink. In fact, the downlink was used to transmit the entire 1 GB LADEE buffer on a number of occasions during the month, taking only minutes instead of the 2–3 days it would have taken had LADEE tried to accomplish this using its radio link. This data was found to be very useful, especially after anomalies occured.

12—Operating the Space Terminal was possible by sending it commands and by monitoring its telemetry. The system was able, of course, to do both of these using the radio links (through the LADEE systems). However, the Space Terminal was configured to send downlink telemetry (a much more complete set) at a rate about 50 times that of the radio link, as well as accept optical uplink commands sent in real time directly from the LLOC to the LLGT. After the first several sessions where all configurations were performed using the radio links, the LLCD team used instead the optical links to do all terminal commanding and configurations throughout the month of passes. That included being able to change the rate and format details of the uplink, with much care, during the sessions. It also made feasible (and demonstrated) the uploading of files including patches to the on-board software.

13—Usually, LLCD requested LADEE to send the power-up commands to the Space Terminal in real time when the ground terminal and planning were announced to be ready. However, on several passes, previously-configured command scripts had been uploaded to LADEE. Then, at a pre-defined time, LADEE autonomously powered up the Space Terminal which then acquired and locked up with the Ground Terminal. This allowed the entire session to be started, run, reconfigured, and shut down with no radio links required. Only pre-loaded "Absolute Time Sequences" and optical links were used. Such capability will greatly simplify future mission operations.

14—As described above, the primary terminal was able to make continuous two-way Time of Flight measurements with high accuracy whenever both the up and down lasercom links were running. This data was processed off-line for LLCD and LADEE and shows the predicted performance—at least as good as the sporadic ranging done by the radio system. It is very likely that future real-time details will be able to be tweaked to give even an order of magnitude (if not more) better than radio performance in future systems.

9 The Meaning of LLCD for Future Science and Exploration Mission

LADEE was a relatively short mission, and had an even shorter period allocated for LLCD operations. However, the approximately 100 total passes, spread out over a wide variety of

day/night, orbital, and atmospheric conditions, plus three different ground terminals, were more than adequate to demonstrate the capability, robustness and reliability of the high-rate LLCD lasercom system.

In the past, science or exploration mission managers have been wary about employing this new technology for a number of reasons. It is hoped that the specific achievements listed in the last section will go a long way to giving confidence to future system designers for including lasercom in order to increase their data return, as well as meet new uplink needs.

Certainly, this exact system could be useful for lunar trunk lines, carrying large amounts of science or mission ops data in both directions. We should point out that the exact same space terminal hardware, if it were to be reprogrammed, could quadruple the downlink capability (if paired with a larger ground telescope). Similarly, the uplink could quadruple its capability with more on-board decoders. (It used a ¼ duty cycle uplink that could be filled in the future, and was already designed with plenty of signal margin.)

A manned exploration mission might not need all this demonstrated data rate capability, and so it is easily envisioned to create an even smaller space terminal that could still greatly outperform a radio system of the same SWaP.

Either of these systems would require the development of a set of ground terminals around the world, for increased availability due to both the rotation of the Earth and clouds.

The same space design, with an enhanced space transmitter amplifier and larger ground telescopes (2–3 meters, say), is predicted to be able to even deliver high capability on missions out to the Lagrangian points or possibly even some asteroids.

Of course, lasercom is highly relevant to planetary missions as well. Their huge distances, though, (hundreds to tens of thousands of times farther than the lunar link) would require a somewhat larger space telescope, an appreciably (though available) higher power space transmitter, and a very much larger ground collector (Boroson et al. 2004; Hemmati et al. 2012).

10 Summary

The LLCD mission was a great success. All the functions operated as predicted or better. PAT was robust and nearly instantaneous. Useful data services were demonstrated and found to be dependable. A rudimentary multi-site ground terminal network was developed and demonstrated. Operations with the NASA spacecraft were made routine. It was demonstrated that optical links could be set up without special hands-on interactions, and ground station handovers were demonstrated. Many lasercom system design approaches were validated, including specifying and validating the spacecraft-terminal interface, building the lasercom links to work through turbulence, operating lasercom as part of an ongoing science mission, employing multi-mode photon-counting receivers, using ground telescope arrays on both the uplink and downlink, employing an inertially-stabilized space telescope, including high-accuracy ranging as a by-product of the lasercom links, and so on.

LLCD has been the world's first successful two-way lasercom link from lunar orbit to the ground, has set the record for highest data rates ever accomplished to or from the Moon using any means, and has been NASA's first lasercom system. It is expected that next-generation science and exploration missions will begin to tap the great potential of optical communications.

References

F. Arnold, M. Mosberger, J. Widmer, F. Gambarara, Ground receiver unit for optical communication between LADEE spacecraft and ESA ground station. Proc. SPIE **8971** (2014)

R.J. Barron, D.M. Boroson, Analysis of capacity and probability of outage for free-space optical channels with fading due to pointing and tracking error. Proc. SPIE **6105** (2006)

C. Bergin, Orion opts for Hybrid Lite comms system due to mass/power issues. http://www.nasaspaceflight.com/2009/03/orion-opts-for-hybrid-lite-comms-system/

A. Biswas, J.M. Kovalik, M.W. Wright, W.T. Roberts, K. Birnbaum, M.D. Shaw, M.K. Cheng, M. Srinivasan, K.J. Quirk, LLCD operations using the Lunar Lasercom OCTL Terminal. Proc. SPIE **8971** (2014)

D.M. Boroson, Channel capacity limits for free-space optical links. Proc. SPIE **6951** (2008)

D.M. Boroson, *Overview and status of the Lunar laser communication demonstration. ICSOS* (2012)

D.M. Boroson, A. Biswas, B.L. Edwards, MLCD: Overview of NASA's Mars Laser communications demonstration system. Proc. SPIE **5338** (2004)

D.M. Boroson, R.S. Bondurant, D.V. Murphy, LDORA: a novel laser communications receiver array architecture. Proc. SPIE **5338**, 56–64 (2004)

D.M. Boroson, B.S. Robinson, D.A. Burianek, D.V. Murphy, F.I. Khatri, J.M. Kovalik, Z. Sodnik, Overview and results of the Lunar laser communication demonstration. Proc. SPIE **8971** (2014)

J.M. Burnside, S.D. Conrad, C.E. DeVoe, A.D. Pillsbury, Design of an inertially-stabilized telescope for the LLCD. Proc. SPIE **7923** (2011)

D.O. Caplan, J.J. Carney, R.E. Lafon, M.L. Stevens, Design of a 40 watt 1.55 µm uplink transmitter for Lunar laser communications. Proc. SPIE **8246** (2012)

E.A. Dauler, B.S. Robinson, A.J. Kerman, J.K.W. Yang, E.K.M. Rosfjord, V. Anant, B. Voronov, G. Gol'tsman, K.K. Berggren, Multi-element superconducting nanowire single-photon detector. IEEE Trans. Appl. Supercond. **17**, 279–284 (2007)

L.E. Elgin, S. Constantine, M.L. Stevens, J.A. Greco, K. Aquino, D.A. Alves, B.S. Robinson, Design of a high-speed space modem for the Lunar laser communications Demonstration. Proc. SPIE **7923** (2011)

R.C. Elphic, G.T. Delory, B.P. Hine, P. Mahaffy, M. Horanyi, A. Colaprete, M. Benna, S. Noble (the LADEE Science Team), The Lunar Atmosphere and Dust Environment Explorer Mission, this issue

D. Fitzgerald, Design of a transportable ground telescope array for the LLCD. Proc. SPIE **7923** (2011)

M.E. Grein, Design of a fiber-coupled superconducting nanowire detector array system for the LLCD. Proc. SPIE **7923** (2011)

H. Hemmati, W.H. Farr, A. Biswas, S. Townes, Sub-Gb/s-Laser-Communications Downlink From Mars. Lunar and Planetary Institute Workshop (2012)

D. Israel, D. Cornwell, Disruption tolerant networking demonstrations over LLCD's optical links, in *IPNSIG Space Technology Innovations Conference* (2014)

D.V. Murphy, R.E. Lafon, J.E. Kansky, M.E. Grein, R.T. Schulein, M.M. Willis, LLCD operations using the Lunar lasercom ground terminal. Proc. SPIE **8971** (2014)

B.S. Robinson, D.M. Boroson, D.A. Burianek, D.V. Murphy, Overview of the Lunar laser communications demonstration. Proc. SPIE **7923** (2011)

B.S. Robinson, D.M. Boroson, D. Burianek, D. Murphy, F. Khatri, A. Biswas, Z. Sodnik, J. Burnside, J. Kansky, D. Cornwell, *"The NASA Lunar Laser Communication Demonstration—Successful High-Rate Laser Communications to and from the Moon"; Space Ops* (2014)

M. Sans, Z. Sodnik, I. Zayer, R. Daddato, *Design of the ESA optical ground station for participation in LLCD. ICSOS* (2012)

S. Shambayati, D. Morabito D, J.S. Border, F. Davarian, D.K. Lee, R. Mendoza, M. Britcliffe, S. Weinreb, Mars Reconnaissance Orbiter Ka-band (32 GHz) Demonstration: Cruise Phase Operations, AIAA SpaceOps Conference, Rome, Italy, June 19–23, 2006

Z. Sodnik, H. Smit, M. Sans, I. Zayer, M. Lanucara, I. Montilla, A. Alonso, LLCD operations using the Lunar Lasercom OGS Terminal. Proc. SPIE **8971** (2014)

M.L. Stevens, D.M. Boroson, D.O. Caplan, A novel variable-rate pulse-position modulation system with near quantum limited performance. in *IEEE Lasers and Electro-Optics Society Annual Meeting* (1999), pp. 301–302

M.L. Stevens, D.O. Caplan, R.T. Schulein, B.S. Robinson, D.M. Boroson, L.E. Elgin, S. Constantine, J.A. Greco, *The Lunar Laser Communication Demonstration Uplink Design and Performance. CLEO* (2014)

M.M. Willis, A.J. Kerman, M.E. Grein, J. Kansky, B.R. Romkey, E.A. Dauler, D. Rosenberg, B.S. Robinson, D.V. Murphy, D.M. Boroson, *Performance of a Multimode Photon-Counting Optical Receiver for the NASA Lunar Laser Communications Demonstration, ICSOS* (2012)

K.E. Wilson, D. Antsos, L.C. Roberts Jr., S. Piazzolla, L.P. Clare, A.P. Croonquist, *Croonquist "Development of the Optical Communications Telescope Laboratory: a Laser Communications Relay Demonstration Ground Station", ICSOS* (2012)